K-band Phased Array Feed (KPAF) Receiver Imaging System

by

Lisa Shannon Locke
B.Sc., University of Alberta, Canada, 1997
M.Sc., University of Cape Town, South Africa, 2001

A Dissertation Submitted in Partial Fulfillment of the
Requirements for the Degree of

DOCTOR OF PHILOSOPHY

in the Department of Electrical and Computer Engineering

University of Victoria

K-band Phased Array Feed (KPAF) Receiver Imaging System

by

Lisa Shannon Locke
B.Sc., University of Alberta, Canada, 1997
M.Sc., University of Cape Town, South Africa, 2001

Supervisory Committee

Dr. Jens Bornemann, Co-Supervisor
(Department of Electrical and Computer Engineering)

Dr. Stéphane Claude, Co-Supervisor
(Department of Electrical and Computer Engineering)

Dr. Colin Bradley, Outside Member
(Department of Mechanical Engineering)

Supervisory Committee

Dr. Jens Bornemann, Co-Supervisor
(Department of Electrical and Computer Engineering)

Dr. Stéphane Claude, Co-Supervisor
(Department of Electrical and Computer Engineering)

Dr. Colin Bradley, Outside Member
(Department of Mechanical Engineering)

ABSTRACT

Astronomy large-scale surveys require instrumentation to minimize the time required to complete observations of large sections of the sky. Optimizing receiver systems has been achieved through reducing the system temperature primarily by advances in low-noise amplifier technology to a point that the internally generated noise is now fast approaching the quantum limit. Instead, reflector-coupled focal plane arrays are now used to increase the field of view (FoV) by employing either multi-element horn feeds or phased array feeds. Widely spaced (2 λ-3 λ diameter) horn feeds inefficiently sample the available focal plane radiation, thus requiring multiple imaging passes. Alternatively, a more efficient method is to use a narrow element (0.5 λ diameter) phased array feed with a beamformer to produce overlapping beams on the sky, fully Nyquist sampling the focal plane with a single pass. The FoV can be further increased with additional phased array feed (PAF) antenna-receiver modules adding to the contiguous fully sampled region.

A 5 x 5 K-band (18 - 26 GHz) single polarization modular PAF incorporating an antenna array of planar axially symmetric elements is designed, simulated, manufactured and tested. Each narrow width tapered slot antenna element has an independent receiver chain consisting of a cryogenic packaged monolithic microwave integrated circuit (MMIC) GaAs amplifier and a packaged MMIC down converting mixer. Synthesized beams and beamformer characteristics are presented. The PAF imaging system performance is evaluated by survey speed and compared to the industry standard, the single pixel feed (SPF). Scientifically, K-band is attractive because it contains numerous molecular transitions, in particular the rotation-inversion lines of ammonia (NH_3). These transitions are excited in dense gas, and can be used to directly measure kinetic temperatures and velocities of protostars throughout the Galaxy. Depending on the line detected, gas of different temperatures can be probed. It is concluded that even with a higher system temperature, a PAF with sufficient number of synthesized beams can outperform a SPF in imaging speed by more than an order of magnitude.

Contents

List of Tables

List of Figures

Symbols and Abbreviations

ALMA	Atacama Large Millimetre Array
ASKAP	Australian Square Kilometer Array Pathfinder
AUT	antenna under test
BAVA	balanced antipodal Vivaldi antenna
CSIRO	Commonwealth Scientific and Industrial Research Organization
CST	Computer Simulation Technology
CWSA	continuous width slot antenna
DRAO	Dominion Radio Astrophysical Observatory
DUT	device under test
ENR	excess noise ratio
FEM	finite element method
FIT	finite integration technique
FoV	field of view
FPA	focal plane array
FPGA	field programmable gate array
FWHM	full width half maximum
GaAs	gallium arsenide
GO	geometrical optics
GTD	geometrical theory of diffraction
HEB	hot electron bolometer
HEMT	high electron mobility transistor
HFSS	High Frequency Structural Simulator
HPBW	half-power beam width
IF	intermediate frequency
InP	indium phosphide

KPAF	K-band phased array feed
LNA	low noise amplifier
LPF	low pass filter
LSB	lower side band
MMIC	monolithic microwave integrated circuit
MoM	method of moments
NH_3	ammonia
NFA	noise figure analyzer
NRAO	National Radio Astronomy Observatory
NRC	National Research Council
NSI	Nearfield Systems Inc.
OMT	ortho-mode transducer
PAF	phased array feed
PO	physical optics
PTD	physical theory of diffraction
PTFE	polytetrafluroethylene
RF	radio frequency
SGH	standard gain horn
SIS	superconductor-insulator-superconductor
SKA	Square Kilometre Array
SOLT	Short Open Load Thru
SPF	single pixel feed
SSST	triple short calibration
SVS	survey speed
T_{sys}	system temperature
USB	upper side band
VNA	vector network analyzer

Acknowledgements

Galactic thank you to James, Mitchell and Sydney for helping me achieve my dreams, to Stéphane Claude for giving me the tools and freedom to learn, I will miss you, and to Jens Bornemann for leading by example.

And to my wonderful parents, who have always told me there's nothing I can't do.

Chapter 1

Introduction

So, five-card stud, nothing wild. And the sky's the limit.
- Captain Jean-Luc Picard

1.1 Phased Array Feeds

Next generation astronomical telescopes require unprecedented levels of sensitivity and efficiency to answer fundamental astrophysical questions about dark matter, the nature of gravity, the generation of magnetic fields in space and the origins of the first stars. From the beginnings of radio astronomy, detecting farther and fainter sources has pushed antenna and receiver technology to extreme limits.

Ever-larger reflectors and the steady progress in low-noise cryogenic amplifier research has improved system sensitivity. However, the internally generated noise is now fast approaching the quantum limit, thus reducing receiver noise temperatures will do little to increase performance.

Therefore, the only way to significantly increase the single dish telescope performance is to use the telescopes' imaging capability. Increasing the number of focal plane elements produces more synthesized beams on the sky and thus faster mapping speeds. Less time is required to image extended sources or complete large surveys of the sky. Phased array feeds (PAF) elements are packed tightly as electromagnetically, physically and economically as possible allowing for full Nyquist sampling of the imaged area in one observation, instantaneously, maximizing the survey speed. Unlike multi-beam feed horns, which can increase the field of view by a factor of the number of horns, their large apertures create an non-uniform image necessitating costly interleaved pointings. The primary contribution of PAFs is the fully Nyquist sampled field of view requiring only one imaging pass, reducing the imaging time by an order of magnitude.

Employing phased array feeds increases the value of current astronomy telescopes and is a worthy avenue of research. The National Radio Astronomy Observatory (NRAO) has identified PAFs to be one of their top technology goals for the next decade [1]. The following is a list of some other groups researching PAFs.

- National Radio Astronomy Observatory (NRAO) and Brigham Young University (BYU)'s 19-element ambient temperature L-band dipole array [2].
- ASTRON's dual-polarized all-metal 8 x 7 Vivaldi array with contributions from Chalmers University and BYU [3].
- NRC Penticton, DRAO - a dual-polarized, all-metal Vivaldi array with embedded low noise amplifier (LNA) elements [4, 5].
- CSIRO's Australian SKA Pathfinder (ASKAP), 36 12-m reflectors outfitted with checker-board style dual-polarized PAFs [6].
- Arecibo's cryogenic 19-element L-band PAF using dual-polarized dipoles [7].

Many other phased arrays are developed for military, commerical and space communication applications with a focus on small form factor and on-chip integration. A few recent examples are listed here.

- 76 - 84 GHz integrated on-chip phased array receiver for automotive radar using alternating amplifiers and phase shifters to minimize power consumption [8].
- All-RF small form factor phased array 8-element antenna array and receiver for the X- and Ku-bands (8 - 18 GHz) for radar, smart antennas and wireless communications [9].

1.2 Thesis Outline

The outline of this thesis is as follows:

Chapter 1 provides an overview of the entire thesis, and distinguishes contributions of the author and others.

Chapter 2 focuses on the imaging system, first explaining the type of astronomical signal to be detected, definitions system temperature and the minimum detectable signal. The paraboloidal reflector geometry, aperture field and focal field are defined. The K-band (18 - 26 GHz) frequency range is chosen for firstly for its significant frequency increase from existing PAF systems, and secondly the astronomy applications including general continuum imaging and ammonia molecular transitions in the 23 - 25 GHz region, which provide information about newly forming stars. Various imaging system architectures are described, the present state of the art and the two possible methods of accomplishing larger fields of view along with early historical examples. Current PAFs including a cryogenic PAF being researched are outlined. The KPAF block diagram system is presented and the survey speed figure of merit for evaluating different PAF receiver systems is explained and calculated at various ambient and cryogenic temperatures.

Chapter 3 introduces the antenna element and provides a detailed description of the tapered slot antenna and the design featured in an earlier parametric study. Description of the substrate, corrugation features for reducing cross-polarization, the antipodal configuration, taper details and the simulated results follow. Requirements for the KPAF antenna are stated and a design summary, custom calibration standards and details of the simulated antenna element are presented. Fabrication details of the planar antenna include photo lithography and laser cutting for sub-millimetre precision cuts of the antenna tapered section. S-parameters and far-field radiation pattern measurements using both planar near-field scanning and far-field techniques in an anechoic chamber are performed along with comparison to full-wave electromagnetic simulations.

Chapter 4 describes the antenna array, starting with the geometrical parameters of element spacing and the maximum array extent. An ideal element, the Gaussian feed is used to validate the calculated geometrical parameters for a 5 x 5 base array and an extended 15 x 15 array. The 5 x 5 KPAF array including tapered slot elements and incorporating mutual coupling is modeled, presenting S-parameters, far-field radiation patterns and noise temperature. The mechanical design is presented for the 5 x 5 array mount.

Chapter 5 completes the KPAF imaging receiver including the low noise amplifier

(LNA), downconverting mixer and beamformer. LNA mechanical and electrical design, the vector network analyzer (VNA), noise figure analyzer (NFA) and cryogenic test setups are described. Ambient temperature and cryogenic LNA measurements include S-parameters and noise temperature. The K to L (0.8 - 1.5 GHz) downconverting mixer interfaces with a functioning PAF beamformer and is designed along with a low-pass filter on the IF output. Two types of beamforming architectures are explained. Parabolic reflectors and the related efficiencies; aperture, spillover and taper, are summarized in relation to optimizing synthesized PAF beams. Three different amplitude weighting schemes are compared in accordance to the maximum gain value and the degree of beam symmetry.

Chapter 6 presents conclusions and ideas for future work for the KPAF imaging system.

1.3 Distinct Contributions of this Thesis

- 5 x 5 compact phased array feed concept, optics and design for prime focus microwave astronomy telescope.
- Imaging receiver system design including antenna element, array configuration and parameters, system gains and noise figure design.
- Tapered slot narrow-width (0.5 λ) broadband (18 - 26 GHz) antenna element design with axially symmetric beam and low cross-polarization.
- Cryogenic noise and S-parameter characterization of low-noise amplifier with commercial GaAs monolithic microwave integrated circuit (MMIC) chip at various bias levels.

1.4 Contributions of Others

- 18 - 24 GHz antipodal tapered slot antenna modified for narrower element spacing [10].
- 3mm linear tapered slot antenna with high gain adapted for 18 - 26 GHz and larger beam requirements [11].

- Substrate integrated waveguide to microstrip taper transition [12].
- Beamforming and aperture efficiency calculations for 40 beam 7 x 7 PAF array [13].
- MMIC low noise amplifier module electrical and mechanical design [14].
- Downconverting mixer MMIC design [14].

1.5 Publications Related to this Thesis

During the candidature for this degree, the author produced or contributed to a number of peer-reviewed related publications.

1.5.1 Journal Papers

L. Locke, J. Bornemann and S. Claude, "Substrate integrated waveguide-fed tapered slot antenna with smooth performance characteristics over an ultra-wide bandwidth", ACES Journal, Vol. 28, pp. 454-462, May 2013.

1.5.2 Conference Papers

L. Locke, S. Claude, J. Bornemann, D. Henke, J. Di Francesco, F. Jiang, D. Garcia, I. Wevers and P. Niranjanan, "KPAF (K-band phased array feed) instrument concept", Proc. SPIE Astronomical Telescopes and Instrumentation, p.1-11, Montreal, Canada, June 2014.

L. Locke, J. Bornemann and S. Claude, "Novel K-band prime focus reflector-coupled focal plane array", Proc. 43rd European Microwave Conf., pp. 211-214, Nuremberg, Germany, Oct. 2013.

L. Locke, Z. Kordiboroujeni, J. Bornemann and S. Claude, "Substrate integrated waveguide couplers for tapered slot antennas in adaptive receiver applications", Proc. 7th European Conf. Antennas Propagat., pp. 2778-2782, Gothenburg, Sweden, Apr. 2013.

Chapter 2

Imaging System

> *I'd like a petite fillet mignon, very lean. Not so lean that it lacks flavour,*
> *but not so fat that it leaves drippings on the plate;*
> *and I don't want it cooked, just lightly seared on either side,*
> *pink in the middle – not true pink, but not a mauve, either –*
> *something in between, bearing in mind the slightest error either way,*
> *and it's ruined.*
> - Dr. Niles Crane

2.1 Introduction

Imaging can be defined as the process of spatially quantifying electromagnetic radiation into a visual representation. To accomplish this, many types of antenna-receiver architectures exist for such diverse subject areas as biomedical imaging, radar, navigation, remote sensing and astronomy. Astronomy large-scale surveys require instrumentation that minimize the time required to complete observations of large sections of the sky.

Optimizing receiver systems has historically been accomplished by reducing the system temperature T_{sys}, the amount of internally generated noise. As one of the first components in the antenna-receiver system, amplifier noise is a major contributor to T_{sys} and has been reduced to almost theoretical minimums through recent semiconductor research. When the noise of the astronomical source plus the antenna is comparable to the amplifier noise, further reductions to amplifier noise will not significantly improve the overall performance. Rather, the receiver can be optimized through improving the survey speed by increasing the number of beams N_b, enlarging the field of view by adding more elements in the focal plane. In essence this creates a "radio camera" and is equivalent to a CCD being a collection of optical receiving elements. The array in the focal plane is capable of providing astronomical telescopes with a far greater imaging capability than with a single element or pixel alone.

The system performance can be quantified by survey speed, SVS, the time required to image a certain field of view. This metric is commonly used for different receiver architectures with variables including T_{sys}, N_b and others as in Section 2.10. For now, it is sufficient to note that survey speed is proportional to the number of beams and inversely proportional to the system noise temperature.

A description of the astronomy signal to be detected, the system temperature T_{sys} and the minimum detectable signal ΔT is outlined. The parabolic reflector-coupled system, commonly used to increase feed gains, improve angular resolution and reduce beamwidth, will be described followed by an explanation for the frequency chosen and the ammonia molecule that can be observed at KPAF frequencies. The imaging system architectures are explored; SPF, multibeam and PAF. Current PAF research at other institutions is detailed, followed by the KPAF system block diagram and the survey speed figure of merit.

2.2 Astronomy Signal Description

Microwave astronomy telescope receivers filter and detect radio emission from astronomical sources.

- These signals are extremely weak, and need to use sensitive amplifier and cryogenic systems to keep the internal receiver temperatures low.
- The signals are Gaussian noise-like and the measured statistical properties do not differ from the noise generated internally in the receiver or from the observed background radiation coupled into the receiver by the antenna.
- The signals are correlated in time, which allows integrating the signal over time to reduce the noise levels while maintaining signal integrity.

2.3 Astronomy System Performance - T_{sys} and ΔT

The noise performance of astronomy receivers is characterized by an equivalent system temperature, T_{sys} (in Kelvins), referred to the feed or even to outside Earth's atmosphere. The temperature units are used for the system to allow direct comparison with source temperatures. System temperatures vary widely depending on the quality of the antenna element and LNA, the use of cryogenic cooling for the antenna and LNA, and the atmospheric water content at the location of the receiver. For this reason, the best astronomical receivers are at sites with high altitude and very dry surroundings, i.e. mountain tops, deserts, and the South Pole. System temperatures can vary 10 - 100 K for receivers from 1 - 100 GHz, and a few hundred K for receivers above 100 GHz.

The observed signal is correlated from one sample to the next, and the noise, being random, will not. Therefore, adding successive measurements reduces the total noise. According to the Nyquist theorem, a time series of measurements of signal of bandwidth B of duration τ will contain $2B\tau$ independent samples, and the Gaussian noise will go down by the square-root of the number of samples. The uncertainty ΔT in the measurement of T is [15]

$$\Delta T = \frac{\alpha T}{\sqrt{2B\tau}} \tag{2.1}$$

where T is the system plus signal temperature in Kelvins, α is a system-related constant that depends on the ratio of time on and off source.

2.4 Paraboloidal Reflector Geometry

The imaging systems to be described usually employ a primary reflector, normally a paraboloid, to increase gain of the observed signal in order to help detect the faint astronomical signals. Throughout this thesis, a prime focus paraboloid reflector with diameter $D = 10$ m and focal length to diameter ratio $F/D = 0.45$ has been used as these are the characteristics of a reflector that is available for prototyping the KPAF system. In Figure 2.1 are definitions of focal plane, focus, focal length and aperture plane that are relevant to imaging system descriptions throughout this thesis.

Focal plane: for an antenna system with a primary reflector, the focal plane is the 2D plane that includes the focus of the reflector and is parallel to the aperture

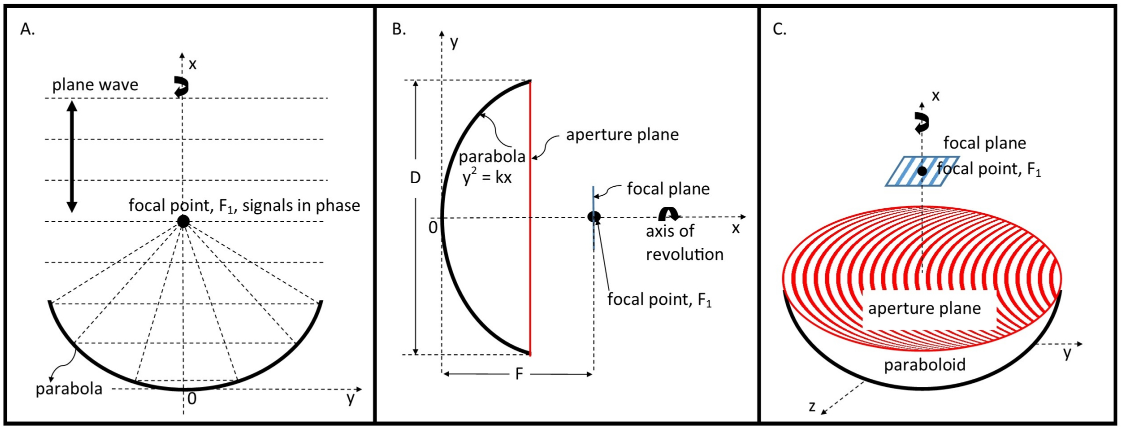

Figure 2.1: Paraboloidal geometry relevant for astronomy imaging. (a) Plane waves illuminating parabola arrive in-phase at focus point, F_1. (b) Description of focal length, F and diameter, D for a parabola. Also location of aperture plane and focal plane. (c) Perspective view of paraboloid, aperture plane and focal plane.

plane of the reflector as seen in Figure 2.1B.

Far field: region in which the electromagnetic wave is essentially planar. The maximum dimension d of the antenna or reflector if used, determines this boundary, $d_{far} \geq \frac{2d^2}{\lambda}$, and λ is the wavelength.

FoV: angular size of far field beam that can be imaged in a single observation, units of steradian (sr) or degree-squared (deg^2).

2.5 Microwave Spectroscopy

Max Planck stated:

$$E = nh\nu \tag{2.2}$$

which says that energy E is directly proportional to frequency ν, h is the Planck constant, and n and is the quantizing integer. When electrons in atoms are excited, the electrons move to higher energy orbitals, and as they fall back to ground level, a photon at a particular frequency is emitted. Molecules, being a collection of more than one atom, can possess a variety of possible energy changes in one or more of: electron spin state, molecular rotations, molecular vibration, and electronic states. The energy change represents a distinct and predictable spectral line at a certain transition frequency. Astrophysicists use molecular spectroscopy to determine chemical composition, physical temperature and relative velocity of molecular species using only passive highly sensitive astronomy receivers.

In 1968, ammonia (NH_3) was the first polyatomic molecule detected in interstellar space [16] and is still of great importance in astrophysics because of the large number of transitions in a great variety of spatial regions. Many ammonia transitions are within the K-band (18 - 26 GHz) spectrum and can be used to derive the mass and temperature of gas in newly forming protostars. The transitions between 23.6 GHz and 25.8 GHz are shown in Table A.1 and the spectrum is seen in Figure 2.2.

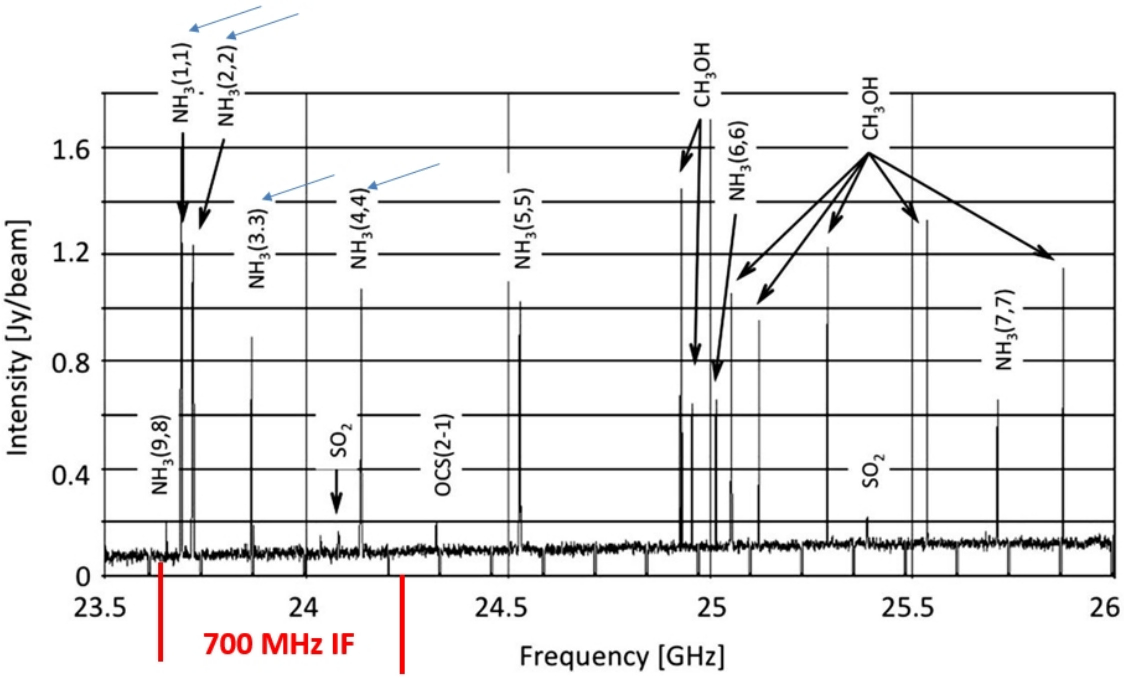

Figure 2.2: Spectrum showing ammonia (NH_3) and methanol (CH_3OH) spectral lines. Blue arrows mark first four ammonia lines of interest imaged by 700 MHz IF band centered at 23.9 GHz. Image from Expanded Very Large Array, NRAO, New Mexico [17].

Line (1,1) at 23.694 GHz and (2,2) at 23.723 GHz can be used to probe cold gas below 40 K, lines (3,3) at 23.87 GHz and (4,4) at 24.139 GHz can be used to probe hotter gas in the 100 K range [16].

Most ammonia clouds of interest are located in the Galactic plane whose relative velocity of up to 1,000 km/s is present. The frequency shift Δf of a line at 23.919

GHz[1] is:

$$\Delta f = f\left(\frac{\Delta v}{\mathrm{c}}\right) = 23.919\ \mathrm{GHz}\left(\frac{1{,}000\ \mathrm{km/s}}{3\mathrm{x}10^8\ \mathrm{m/s}}\right) = 80\ \mathrm{MHz} \tag{2.3}$$

$$1\ \mathrm{km/s} \Rightarrow 80\ \mathrm{kHz} \tag{2.4}$$

In order to resolve the ammonia line in cold clouds, the high spectral resolution of 1 km/s is desired corresponding to 80 kHz frequency resolution [18] which would be achieved in the backend electronics following the beamfomer. This expands the frequency range to F_{min} to F_{max}.

$$F_{min} = F_{(1,1)} = 23.694\ \mathrm{GHz} - 80\ \mathrm{MHz} = 23.618\ \mathrm{GHz} \tag{2.5}$$

$$F_{max} = F_{(4,4)} = 24.139\ \mathrm{GHz} + 80\ \mathrm{MHz} = 24.219\ \mathrm{GHz} \tag{2.6}$$

Thus the minimum required RF bandwidth to cover the ammonia spectral lines (1,1) through (4,4) is

$$F_{max} - F_{min} = 601\ \mathrm{MHz}. \tag{2.7}$$

How many lines can be observed simultaneously? A receiver's bandwidth is limited by the intermediate frequency (IF) bandwidth. For the KPAF system, the beamformer input sets the maximum bandwidth to 700 MHz which will cover the 601 MHz required by the first four ammonia lines, centered at 23.919 GHz. The (5,5) transition cannot be detected as it is 840 MHz away from (1,1). However, if it is decided that (5,5) is more desirable than (1,1), the 700 MHz bandwidth can be shifted to cover only (2,2), (3,3), (4,4) and (5,5). This involves a slight modification of the local oscillator frequency at the time of observation.

2.6 Frequency Selection

K-band was chosen to observe the ammonia molecular transitions at 23.6 - 24.2 GHz, and it is more than a factor of 10 higher in frequency than existing L-band (0.8 - 1.5 GHz) PAFs and presents significant engineering challenges for antenna and low noise cryogenic receiver design. In addition, test instrumentation covering the K-band is available at the University of Victoria and the NRC Herzberg.

---

[1] 23.919 GHz is midway between the (1,1) and (4,4) ammonia line.

2.7 Imaging System Architectures

The single pixel feed, the multi-beam feed and the phased array feed are introduced and relative strengths and weaknesses are outlined.

2.7.1 The Single Pixel Feed

Single pixel feeds are optically coupled to large reflectors to increase gain and improve angular resolution. The feed is composed of a single antenna element followed by a low-noise receiver and square-law detector. The antenna is usually a feedhorn, which functions as an electromagnetic wave transducer from free space into a guided wave medium such as waveguide or coaxial cable. Major components of a heterodyne receiver are:

- a polarizing separation device; an ortho-mode transducer (OMT) or polarizer,
- a directional coupler for noise calibration,
- a low-noise amplifier or other active component,[2]
- at least one mixing stage with local oscillator input, and
- a square-law detector with voltage input: $V(t)$, power output: $V^2(t) \propto P(t)$, where $P(t)$ is the output power in the backend section.

Other signal conditioning components including filters, attenuators, amplifiers and phase shifters are employed as needed. More detail on the receiver can be found in Chapter 5.

Since the signals of interest are incredibly weak, the receiver noise performance is critical, so the OMT, noise couplers and low noise amplifier are cooled to 16 Kelvin (-257°C) or 4 Kelvin (-269°C) for SIS and HEB type detectors. The typical structure of a heterodyne SPF is shown in Figure 2.3.

The first telescope used in radio astronomy was Karl Jansky's 20.5 MHz array of dipoles in Figure 2.4a to investigate noise on trans-Altantic telephone cables. He found the source to be originating from the centre of the Galaxy. The discovery made the front page of the New York Times on May 5, 1933 and he published his results in the Proceedings of the IRE [19, 20].

---

[2] Choice of active components is usually dictated by frequency. They include direct amplification techniques (HEMT, InP, GaAs amplifiers) for the low $<\sim$150 GHz region, superconducting tunnel junctions (SIS mixers) for $\sim$70-$\sim$700 GHz, and Hot electron bolometers (HEB) for $\sim$600+ GHz.

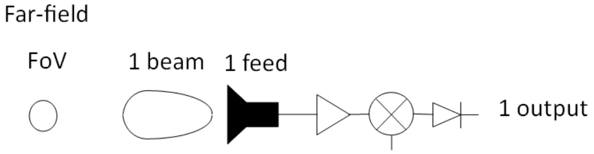

Figure 2.3: Single pixel antenna-receiver architecture including farfield beam.

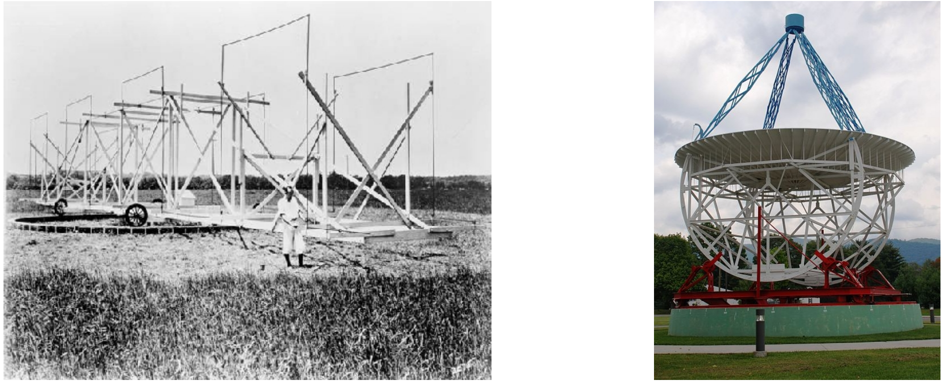

(a) 1933: Jansky, first radio astronomy telescope

(b) 1937: Reber, second radio astronomy telescope

Figure 2.4: Early radio astronomy telescopes. (a) Karl Jansky's 1933 Bell Labs, NJ array used to discover the radio noise from the centre of the Milky Way. (b) Grote Reber's 1937 9-m paraboloid and SPF reconstructed at NRAO, Green Bank, WV.

An amateur astronomer and HAM radio operator, Grote Reber continued Jansky's work and built a radio astronomy telescope with SPF in Figure 2.4b in his backyard inadvertently scaring his neighbours. He built receivers at 3.3 GHz, 900 MHz and finally 160 MHz for this reflector to image the Galaxy and confirm Jansky's discovery.

Single pixel feeds posses the following characteristics when compared with multi-beam feeds and phased array feeds:

Best sensitivity: Post-WWII radar technology fueled radio astronomy; decades of research into both low-noise corrugated feedhorns and heterodyne active component technologies resulted in systems with the absolute lowest system noise performance and to this day provide a low-noise (sensitivity) benchmark for all future system architectures. Use of a cryogenic dewar to cool the feed horn and the first active component to 16 K for two-stage cryogenic systems, and 4 K for three-stage cryogenic systems, are primarily responsible for the low noise performance. Sensitivity, the ability of a system to detect weak signals, is defined as the effective antenna area A_{eff} divided by the system temperature T_{sys} with units m^2/K.

Good resolution for fine structure: The distance at which two point sources will be just resolved is known as the Rayleigh resolution [21], ϕ_c, or smallest observable object, and is defined as one-half of the beam width between first nulls (BWFN/2). For a reflector-feed system, the resolution improves as the reflector diameter, D, is increased:

$$\phi_c = \frac{\text{FWHM}}{2} = \frac{c_1 \lambda}{D} = \text{ HPBW} \tag{2.8}$$

where λ is the wavelength of operation and the constant c_1 depends on the aperture illumination of the reflector but can be approximated to 1. Using a large reflector drastically improves the observable resolution, which is desired for detecting fine details. To this day, state of the art astronomy telescopes employ single pixel feeds, offering unprecedented sensitivity at the expense of small sky coverage.

Small field of view (FoV): Only one small beam is formed for imaging, which when used to map large-scale structures, can take many days of expensive telescope time and computing effort for reducing data. FoV is defined as the region of the sky that can be imaged in a single observation.

For example, a 10 GHz ($\lambda = 3$ cm wavelength) single pixel receiver at the focus of a 10 m paraboloidal reflector will have:

$$\text{SPF: } \phi_c = \frac{\lambda}{D} = \frac{0.03 \text{ m}}{10 \text{ m}} \frac{180^\circ}{\pi} \frac{60'}{1^\circ} = 10.3' \text{ resolution.} \tag{2.9}$$

2.7.2 Multi-beam Feed

The ever-growing need for imaging large fields of view cannot be realistically accomplished by scanning a single pixel feed as it requires a lot of expensive telescope time. One solution is to fill the focal plane of the reflector with more than one feed, i.e. focal plane arrays.

There are two primary types of focal plane arrays: multi-beam and phased array feeds, they differ mainly by their distance between antenna elements. Most research centres and observatories are currently implementing multi-beam systems due to the ability to use excellent low-noise feedhorns and mature receiver technology.

Feedhorns are electrically large (2-3 λ) in diameter. Judicious placement in the focal plane is needed to minimize defocussing effects (gain drop, coma effects, astigmatism) of the outermost elements. This arrangement of feeds produces farfield beams that barely overlap, i.e. at the -20 dB range, thus they do not adequately Nyquist-sample the field and leave significant "holes" between beams. Nyquist-sampling of the focal plane is covered in Chapter 4. Therefore, interleaved pointings are required to fill in the spaces between beams which add to the total observation time. Each feedhorn is connected to a separate receiver chain as seen in Figure 2.5.

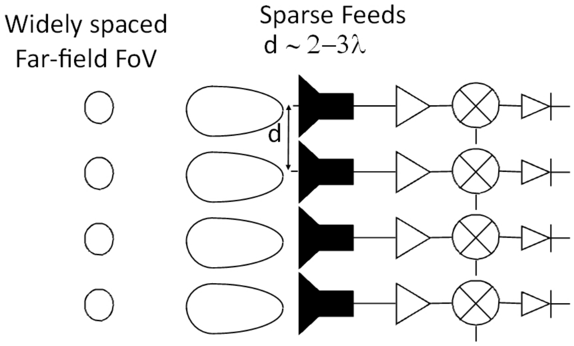

Figure 2.5: Multi-beam antenna-receiver architecture including sparse farfield beams.

Now a mature technology, multi-beam systems have drawbacks. The waveguide feedhorns and polarization elements are bulky and expensive. The polarization elements and low noise amplifiers (LNAs) require a large cryogenic dewar. Multi-beam antennas on altitude - azimuth telescopes need to be rotated to keep the relative beam locations on the sky constant as the observation is tracked in time. Perhaps most detrimental to the multi-beam is the need to re-image the portion of sky many times due to inefficient focal plane sampling, needing to fill in the space between the beams, for a fully sampled FoV. However, the multi-beam feed has the same high angular resolution as the SPF.

Multi-beam arrays in the literature are also known as "Discretely Processed Focal Plane Arrays" [22] and "Focal Plane Arrays." [23, 24]

2.7.3 Phased Array Feeds

An emerging technology, phased array feeds are also collections of densely-packed feeds, with centre-to-centre distance $\leq \lambda/2$ located in the focal plane of a reflector. Signals from the feeds are weighted and phased in a beamformer as depicted in Figure 2.6. Unlike multi-beam feeds, PAFs fully sample the focal plane due to the small, usually planar feeds that can be placed as close as 0.1 λ apart [25]. The wide beamwidth and close spacing result in an adequately sampled far field, as they overlap at the 3 dB level, requiring only one pass through the region, reducing the required observing time.

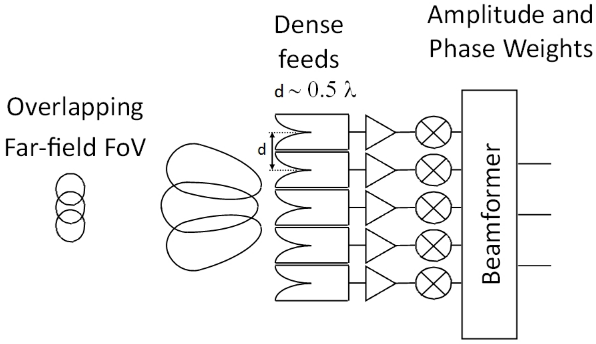

Figure 2.6: Phased array feed antenna-receiver architecture including farfield overlapping beams.

There are other advanced capabilities due to the beamforming; in [26] reduced off-axis aberrations for tolerating slightly defocused elements, optimal beamforming, and compensation of reflector-surface distortion are discussed, and in [27, 28] coma correction, beam switching and adaptive nulling are explained. Beamformer use in multi-beam communication satellites system for shaped beams is described in [29].

PAFs are now possible due to development in a number of areas. Advances in analog electronics allow low-noise amplifiers with noise figures below 0.35 dB [30] and highly integrated receiver modules incorporating hundreds of receivers per antenna. Advances in electromagnetic analysis capabilities [31] enable simulation and optimization of electrically large structures (5 λ - 10 λ) including multiple antenna elements, feeds, and receiver elements along with fine structures at a few hundredths of wavelength. Improvements in digital electronics [32] allow digital beam forming to be accomplished with ever-increasing bandwidths, currently around 300 - 500 MHz.

However, the ultra-low T_{sys} values for cryogenic single pixel feeds cannot currently be attained with planar PAFs as the antenna element has higher losses than corrugated feedhorns and the mutual coupling between densely packed receivers is not optimum for low noise performance. Also, it is a mechanical and thermal challenge to engineer the amplifier circuits, miniature connectors and densely packed cable assemblies that small arrays require.

Phased Array Feeds is the term used by [2, 33] whereas [34] uses “dense focal plane arrays”.

2.8 Existing PAF Systems

PAF technology has been implemented in astronomy mostly at L-band (1 - 2 GHz) frequencies primarily for the Square Kilometer Array, an international telescope consortium [35]. These are some groups involved in phased array feed systems in the research or production stage:

- National Radio Astronomy Observatory (NRAO) and Brigham Young University (BYU)’s 19-element ambient temperature L-band dipole array [2].
- ASTRON’s dual-polarized all-metal 8 x 7 Vivaldi array with contributions from Chalmers University and BYU [3].
- NRC Penticton, DRAO - a dual-polarized, all-metal Vivaldi array with embedded low noise amplifier (LNA) elements [4, 5].
- CSIRO’s Australian SKA Pathfinder (ASKAP), 36 12-m reflectors outfitted with checker-board style PAFs [6].
- Arecibo’s cryogenic 19-element L-band PAF using dual polarized dipoles [7].
- Oxford’s compact planar microstrip Yagi antenna for use at 1.05 THz coupled to a SIS mixer intended for ALMA band 11 [36].

To my knowledge, KPAF is the only heterodyne PAF system between 2 GHz and 1 THz. PAFs at K-band are a factor of ≈ 10 greater in frequency than L-band, translating directly to 10 times smaller structures. Small planar transmission lines, more delicate and complex mechanical integration issues, smaller coaxial connectors and thermal issues are abundant at K-band, yet low losses and good system performance must be maintained.

2.9 KPAF System Description

A block diagram of the KPAF system including a 5 x 5 planar antenna array, 5 x 5 block of 25 dB gain cryogenic MMIC low noise amplifiers (LNAs), and 25 mixers down converting from 18 - 26 GHz to 0.8 - 1.5 GHz allowing the use of an existing L-band receiver and beamformer [37] are shown in Figure 2.7.

In order to consider the impact of overall system temperature, T_{sys}, three different configurations have been considered, each with varying physical temperatures, and the first two configurations are built and tested in this work. The first is an ambient temperature (300 K) antenna and LNA, the second is an ambient temperature antenna and a cryogenic (13 K) LNA, and the third is a cryogenic antenna and a cryogenic LNA. The loss of the antenna is determined from radiation efficiency calculations to be 0.55 dB and the coaxial line loss is 0.2 dB. The LNA module's ambient temperature performance is 26.5 dB gain and 180 K noise temperature, but it was packaged for cryogenic operation and the performance at 13 K physical temperature is 30 dB gain and 25 K noise temperature. The calculated T_{sys} for a single antenna element and LNA is shown, and the array Tsys is estimated to be 15% higher to account for mutual coupling of the elements [38]. The single antenna element efficiency is assumed to be the same as the array element efficiency.

2.10 PAF Figure of Merit

Imaging systems with different number of beams, sensitivities and polarizations can be compared by using survey speed, SVS, the imaging speed per unit time assuming uniform gain across the sampled FoV [39]. The Square Kilometer Array (SKA) memo series has a wealth of information on this subject [39, 40, 41], presenting survey speed equations for both single dish and interferometer systems.

$$SVS = \frac{FoV}{t} = \frac{N_{pol} N_b \Omega_b}{t} = N_{pol} N_b \Omega_b B \Big(\frac{A_{eff}}{T_{sys}}\Big)^2 \tag{2.10}$$

$$\Omega_b = \text{HPBW}^2 = \left(\frac{c_1 \lambda}{D}\right)^2 \tag{2.11}$$

where

- instantaneous field of view, FoV
- time required to sample the image, t
- number of independent polarizations, N_{pol}
- total number of independent synthesized beams, N_b

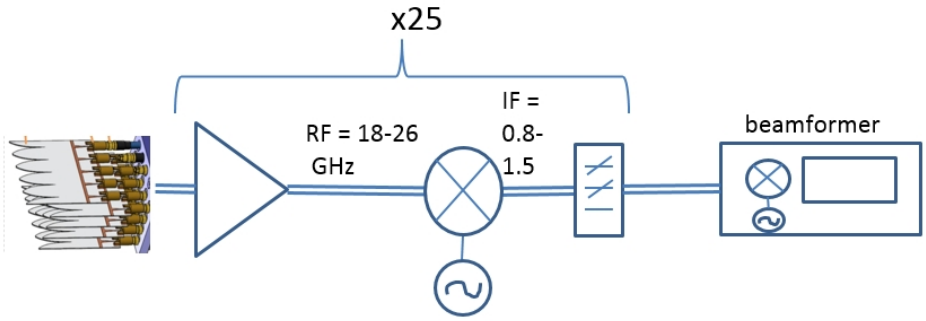

Physical Temperatures		antenna + cable	LNA	Tsys Single	Tsys Array
$T_{ANT} = T_{LNA}$ = 300K	Gain/Loss (dB)	-0.75	26.5	270	311
	Noise Temp (K)	57	180		
T_{ANT} = 300K, T_{LNA} = 13K	Gain/Loss (dB)	-0.75	30	86	99
	Noise Temp (K)	57	25		
$T_{ANT} = T_{LNA}$ = 13K	Gain/Loss (dB)	-0.75	30	32	37
	Noise Temp (K)	2.5	25		

Figure 2.7: KPAF block diagram showing the antenna array, one of 25 total receiver chains, and the beamformer backend. Three different physical temperature scenarios are outlined. Component gains and losses are used to compute system temperatures. Single T_{sys}: single antenna element plus receiver system, Array T_{sys}: array plus receiver system, this value is expected to be 15% higher than Single T_{sys} [38]. The backend from PHAD [37] will be used for testing.

- solid angle of each beam, Ω_b
- signal processing bandwidth, B
- antenna sensitivity, $\frac{A_{eff}}{T_{sys}}$, where A_{eff} is the effective antenna collecting area taking into account efficiencies, and T_{sys} is the system temperature.
- proportionality constant, c_1, is dependent on the aperture illumination.
- reflector diameter, D.

Table 2.1 compares the merits of a cryogenic single pixel feed, cryogenic 7-beam multi-beam, and various 40 beam PAF systems architectures with system temperatures ranging from 35 K to 311 K. A 5 x 5 PAF system has only enough elements to adequately produce one beam. However, by using the 5 x 5 PAF in a modular form to create a 10 x 10 PAF, at least 40 beams can be produced. Given that the antenna

	N_b	T_{sys} [K]	$(A_{eff}/T_{sys})^2$ [$\mathrm{m}^4/\mathrm{K}^2$]	$\frac{SVS(PAF)}{SVS(SPF)}$
SPF: Cryogenic	1	35	2.47	1
multi-beam: Cryogenic	7	35	2.47	7
PAF: 311 K Ambient Temperature	40	311	0.03	0.3
PAF: 175 K	40	175	0.10	0.8
PAF: 150 K	40	150	0.13	1.1
PAF: 99 K: 13 K ant + 300 K LNA	40	99	0.30	2.5
PAF: 50 K	40	50	1.2	14
PAF: 42 K	40	42	1.7	17
PAF: 37 K: 13 K ant + 13 K LNA	40	37	2.2	18

Table 2.1: Comparison of SPF, multi-beam and PAFs with different system temperatures to demonstrate the increased imaging factor of a single polarization PAF compared with a cryogenic dual-polarizations single pixel feed.

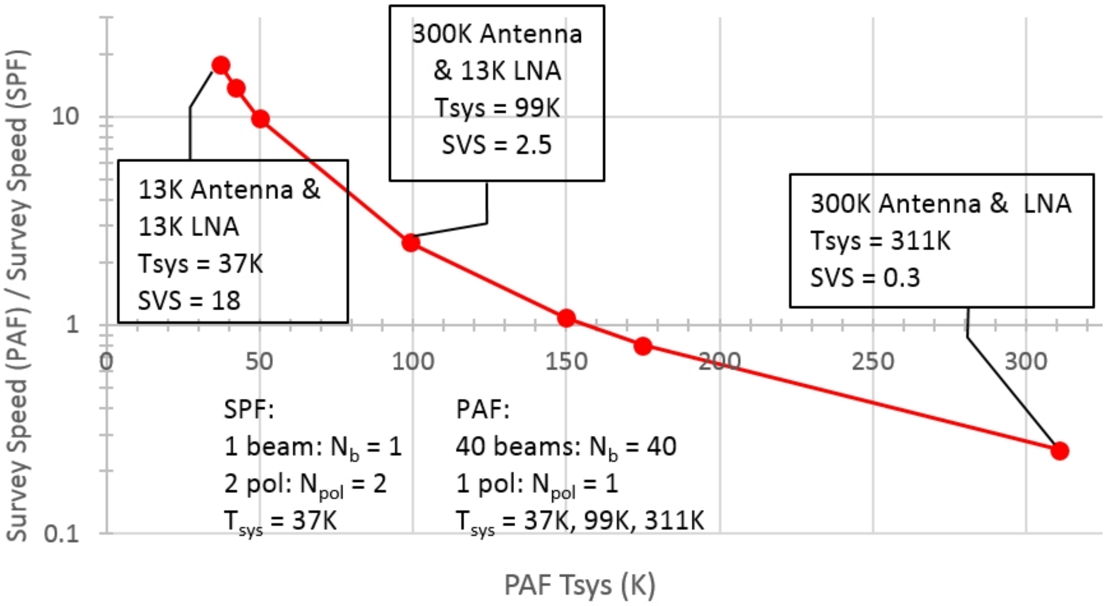

Figure 2.8: A PAF system normalized to an SPF as given by Equation 2.10. The SPF is assumed to have dual-linear polarization with a system noise temperature of 37 K. The PAF is assumed to have a single linear polarization and is shown plotted with various physical temperatures of the antenna and LNA. The cryogenic 40 beam PAF is competitive with the cryogenic dual-polarization SPF by a factor of 18.

spacing is 6.2 mm, we expect that an array of 7 x 7 can synthesize approximately 40 beams, Nyquist spaced and using a hexagonal layout at 24 GHz at the focal plane of a telescope with an F/D = 0.45. We compare this 40 beam PAF system to a benchmark, a cryogenic dual-polarization SPF, by taking the ratio of the PAF and SPF survey speeds in Figure 2.8.

The survey speeds are normalized to that of the cryogenic single pixel feed. In Table 2.1, for all instances, reflector diameter D = 10 m, efficiency $\varepsilon = 0.7$, and effective area, $A_{eff} = \varepsilon\pi(D/2)^2 = 55.0 \text{ m}^2$ and the frequency of operation is 26 GHz. Figure 2.8 shows the a PAF system normalized to a single pixel feed as given by Equation 2.10. The SPF is assumed to have dual-linear polarization with system noise temperature of 37 K. The PAF is assumed to have a single linear polarization and is shown plotted with various physical temperatures of the antenna and LNA. The tabulated results show that if we compare all other configurations to the cryogenic SPF, then a higher ratio of survey speed of PAF compared with the survey speed of the SPF equate to a faster imaging process by that factor.

The physical temperature scenarios noted in Figure 2.7 are included in Table 2.1 and explained as follows:

300 K antenna and 300 K LNA An ambient temperature antenna and LNA has an array T_{sys} = 311 K, see Figure 2.7. This system is actually slower than a SPF by a factor of 1/0.3 or approximately 3.3.

300 K antenna and 13 K LNA Cooling the amplifier while keeping the antenna at ambient temperature results in a performance factor of 2.5 times better than SPF.

13 K antenna and 13 K LNA The best case is a cryogenic system, T_{phys} = 13 K, the T_{sys} = 37 K which is 18 times better than a dual polarization cryogenic SPF.

A 40 beam single polarization PAF system with a cryogenic antenna and cryogenic LNA will outperform a single beam, dual polarization, single pixel feed by a factor of 18. A single beam PAF which is generated with only a 5 x 5 PAF is not enough, it is necessary to employ the modularity of the KPAF system in order to create a larger 10 x 10 or 15 x 15 array.

Chapter 3

Antenna Element

I'm going to need a bigger antenna.
- Ellie Arroway

The propagation of an electromagnetic wave is an iterative induction process of time varying electric and magnetic fields, governed by Maxwell's first two equations 3.1, 3.2, assuming a source-free region. A time varying field $\mathbf{E}(t)$ at t = 0 induces a magnetic field at $t = \Delta t$ which in turn induces a changing electric field at $2\Delta t$ and so on as demonstrated in Figure 3.1, the progression forms an electromagnetic wave.

$$\nabla \times \mathbf{E} = -\frac{\partial(\mu \mathbf{H})}{\partial t} \tag{3.1}$$

$$\nabla \times \mathbf{H} = -\frac{\partial(\varepsilon \mathbf{E})}{\partial t} \tag{3.2}$$

The heart of the KPAF system, the tapered slot antenna (TSA) offers moderate gain, narrow width, therefore high spatial density, and the ability to integrate active components due to its planar substrate. In this chapter, the tapered slot antenna and its family are introduced, a parametric study of the TSA is described, followed by the KPAF antenna element design, simulation results, fabrication details and measurements. Throughout this thesis, both CST Microwave Studio and Ansoft HFSS simulation tools were used and their results compare favourably.

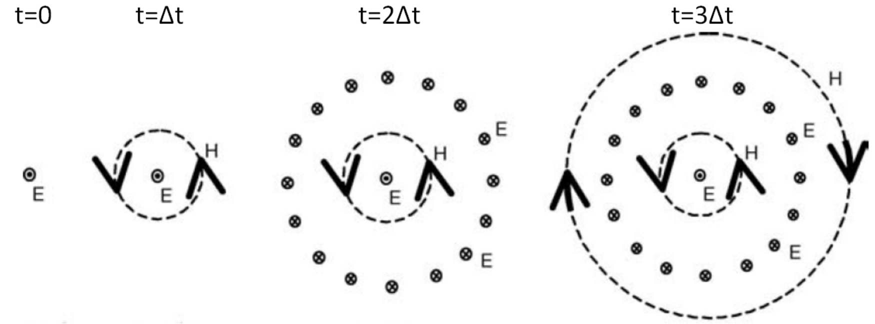

Figure 3.1: Maxwell's first two equations demonstrate the alternate induction of E- and H-fields by time-varying H- and E-fields respectively. Each successive timestep represents one quarter wavelength (90°) steps creating a propagating electromagnetic wave.

3.1 S-parameter Primer

Scattering parameters or S-parameters are a means for characterizing linear electrical n-port networks. S-parameters differ from other network parameters such as H-, Y- and Z-parameters:

1. S-parameters measurements relate travelling waves and thus are quantities of power instead of voltages and currents, and
2. they use matched loads instead of short or open circuit conditions as broadband loads are easier and more accurately produced at microwave frequencies than broadband short and open circuits.

The term scattering refers to the method that the currents and voltages in a transmission line are affected when meeting a discontinuity, in essence an impedance that differs from the line's characteristic impedance. A two-port network is defined in Figure 3.2.

The complex reflection coefficient Γ, with magnitude ρ and angle Θ, represents the quality of the impedance match between the load, Z_L and the characteristic impedance of the line, Z_0.

$$\Gamma = \rho\angle\Theta = \frac{Z_L - Z_0}{Z_L + Z_0} \tag{3.3}$$

For an N-port network a_n is the amplitude of the incident voltage wave on port n and b_n is the amplitude of the reflected voltage wave from port n. The scattering

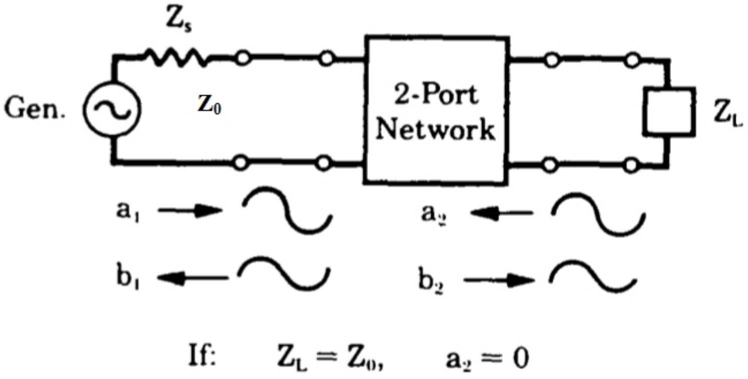

Figure 3.2: A two-port S-parameter network. [42]

matrix is defined in relation to the incident and reflected voltages as

$$[b_n] = [S][a_n]. \tag{3.4}$$

Thus we can define the four S parameters associated with a 2-port network:

Input reflection coefficient, S_{11}: When port 2 is terminated with Z$_0$,

$$S_{11} = \left.\frac{b_1}{a_1}\right|_{a_2=0} = \Gamma^{(1)}\big|_{a_2=0} = \left.\frac{Z_{in}^{(1)} - Z_0}{Z_{in}^{(1)} + Z_0}\right|_{Z_0 \text{ on port 2}} \tag{3.5}$$

Input Return Loss = -20 $\log_{10}(S_{11})$ dB

Output reflection coefficient, S_{22}: When port 1 is terminated with Z$_0$,

$$S_{22} = \left.\frac{b_2}{a_2}\right|_{a_1=0} = \Gamma^{(2)}\big|_{a_1=0} = \left.\frac{Z_{in}^{(2)} - Z_0}{Z_{in}^{(2)} + Z_0}\right|_{Z_0 \text{ on port 1}} \tag{3.6}$$

Output Return Loss = -20 $\log_{10}(S_{22})$ dB

Forward transmission coefficient, S_{21}: Measuring port 2 with respect to port 1,

$$S_{21} = \left.\frac{b_2}{a_1}\right|_{a_2=0} \tag{3.7}$$

Forward gain = 20 $\log_{10}(S_{21})$ dB

Reverse transmission coefficient, S_{12}: Measuring port 1 with respect to port 2,

$$S_{12} = \left.\frac{b_1}{a_2}\right|_{a_1=0} \tag{3.8}$$

Reverse gain = 20 $\log_{10}(S_{12})$ dB

3.2 The Tapered Slot Antenna

Two types of travelling wave antennas are the surface wave (also called slow wave) antenna, for which $v_{ph} < c$ and the leaky wave (or fast wave) antenna, for which $v_{ph} > c$. Some features and examples of each are outlined in Figure 3.3.

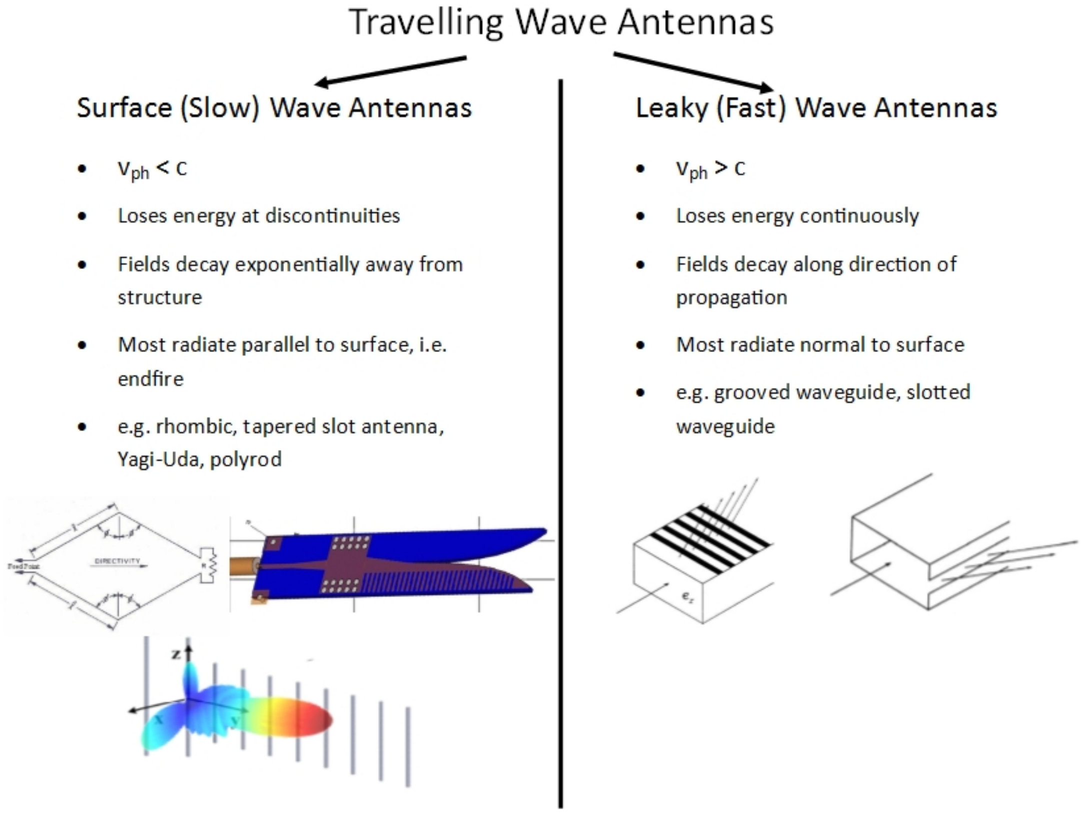

Surface (Slow) Wave Antennas

- $V_{ph} < C$
- Loses energy at discontinuities
- Fields decay exponentially away from structure
- Most radiate parallel to surface, i.e. endfire
- e.g. rhombic, tapered slot antenna, Yagi-Uda, polyrod

Leaky (Fast) Wave Antennas

- $V_{ph} > C$
- Loses energy continuously
- Fields decay along direction of propagation
- Most radiate normal to surface
- e.g. grooved waveguide, slotted waveguide

Figure 3.3: The tapered slot antenna is a type of surface wave antenna. Together with leaky wave antennas, they constitute the larger family of travelling wave antennas.

The radiation mechanism of the tapered slot antenna, being a type of travelling wave antenna, is a travelling wave propagating along the surface of the antenna taper.[1] The electromagnetic wave spectral components propagate along the increasingly separated metallized tapers until the distance between the edges is equal to half of its wavelength, allowing wave separation from the antenna structure, and radiation occurs [43]. The high frequencies radiate first, when the aperture is narrow, while the low frequencies radiate at the end of the antenna. Most non-radiated currents are dissipated in the metal corrugations near the aperture, minimizing the reflection back to the antenna input. This absorptive end of the circuit is a feature of the travelling wave antenna, where an absorptive end is required to prevent standing waves. The aperture end is properly terminated in that it matches the impedance of free space; $\eta = 120\pi\ \Omega$. Despite its planar nature, the TSA like Yagi-Udas and polyrod antennas can produce highly directive farfield beams with nearly equal beamwidth in both E- and H-planes beams due to the travelling wave gradually building up the fields along the surface taper. The orientation of the E- and H-planes are depicted in Figure 3.4 and explained in Section 3.2.1.

Early comprehensive studies [44, 43, 45, 46] present a guide for designing well behaved TSAs with roughly symmetric beams, i.e. HPBW of E-plane pattern = HPBW of H-plane pattern. The recommended substrate width is based on effective dielectric thickness, t_{eff}, ensuring main beam integrity, beamwidth and impedance effects of various dielectric substrates and taper shapes, and the fundamental radiation mechanism are covered. Korzeniowski makes important conclusions, notably that HPBW can increase with frequency [47] and explains the contributing factors to E- and H-plane pattern shapes; E-plane depending heavily on taper shape and antenna length, whereas H-plane depending on length only, relatively insensitive to flare angle as the aperture width dimension is not present in this plane. Other antennas with variations in taper and configuration include the continuous width slot antenna (CWSA), bunny-ear, balanced antipodal Vivaldi antenna (BAVA) [48], and the Fermi antenna [49].

3.2.1 Coordinate System Definitions

The physical antenna geometry is defined in Figure 3.4, using the Cartesian coordinate system, and is oriented with the propagation along the $\hat{z}$ axis and substrate in the $y - z$ plane with the substrate thickness in the transverse direction, x. The farfield

---

[1] Travelling wave antennas are defined as an antenna for which the fields and currents can be represented by one or more travelling waves, usually in the same direction. A proper impedance termination is necessary to support the travelling wave, minimizing the reflected wave.

patterns are measured in the spherical coordinate system, and as per convention, ϕ is measured from $\hat{x}$ in the $x - y$ plane and θ away from $\hat{z}$. Because the electric field vector is perpendicular to the metal faces, it is oriented in $\hat{x}$ in the SIW region and in $\hat{y}$ at the aperture as the tapers transition to free space. Thus the E-plane is $y - z$ at $\phi = 90°$ and the H-plane is $x - z$ at $\phi = 0°$.

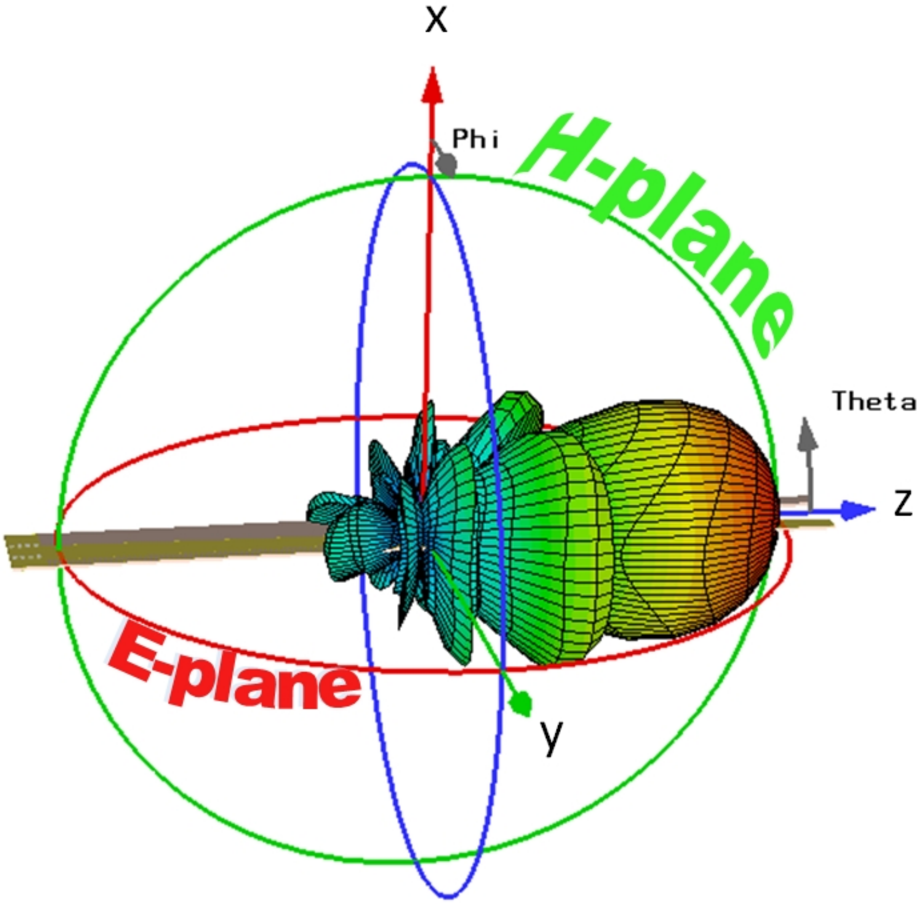

Figure 3.4: TSA geometry cartestian coordinate system and far-field spherical coordinates (ϕ, θ) including E-plane ($\phi = 90°$) and H-plane ($\phi = 0°$) definitions.

3.2.2 Substrate

Microstrip antennas have a few disadvantages inherited from microstrip circuit technology such as low radiating efficiency due to losses in the substrate, it is less physically robust than waveguide, and cryogenic cooling of substrate material is largely untested. However, microstrip components are less expensive than waveguide, have narrower profiles, can be integrated with circuits and components and can be easily manufactured into arrays. For these reasons, microstrip was chosen as the medium for the antenna.

The substrate used, 0.381 mm (15 mil) thick Rogers RT/duroid 6010LM ($\varepsilon_r = 10.2$, $\tan\delta = 0.003$ at 20 GHz), microwave laminate is a flexible ceramic-PTFE composite with 0.0175 mm copper cladding on top and bottom faces, has excellent thermal conductivity, 31 W/mK at 20 °C for active component heat dissipation, and a high mechanical strength. The datasheet is in Appendix B. The 0.381 mm thickness is a compromise between mechanically unstable thin substrates, and undesireable surface waves propagating through thick substrates.

Microwave theory states that the first undesirable surface wave mode in a grounded dielectric slab waveguide with thickness, $t = 0.381$ mm will be the TE_1 mode with cutoff frequency, f_c [50]:

$$f_c = \frac{\mathrm{c}}{4t\sqrt{\varepsilon_r - 1}} = 49\ \mathrm{GHz}. \tag{3.9}$$

Therefore, operation up to 49 GHz will be surface-wave mode free.

Yngvesson [46] provides a general formula for the effective substrate thickness, t_{eff} in Equation 3.10 and a recommended range for main lobe integrity and low sidelobes in Equation 3.11 normalized to free space wavelength λ_0.

$$t_{eff} = t\sqrt{\varepsilon_r - 1} = 1.156\ \mathrm{mm} \tag{3.10}$$

$$0.005 < \frac{t_{eff}}{\lambda_0} < 0.03 \tag{3.11}$$

For 0.381 mm Rogers 6010 substrate, the effective substrate thickness $t_{eff}/\lambda_0 = 0.07$ at 18 GHz and 0.10 at 26 GHz. These values are above the recommended range in Equation 3.11 however, the far-field simulation of the main beam and sidelobes in Section 3.3 show that the substrate thickness is acceptable when used in conjunction with corrugations which will be described in Section 3.2.3. For future arrays at higher frequencies the inequality in Equation 3.11 will become more difficult to satisfy and will largely determine the type and thickness of dielectric required.

The maximum width of each antenna element, W_{sub}, determines the pitch of the array in the plane of the substrate. This pitch is constrained by the requirement to avoid grating lobes in arrays; W_{sub} is recommended to be less than 0.5 λ_0 to 0.6 λ_0 to avoid grating lobes [46]. In order to accommodate the smallest wavelength: $\lambda_{min} = c/f_{max} = 11.5\ \mathrm{mm} \Rightarrow \lambda_0$. This is the free-space wavelength. W_{sub} is set to

6.2 mm. This 0.53 λ width is a tough criterion to meet over the entire 18 - 26 GHz frequency range while maintaining quasi-symmetrical beamwidth and low reflection coefficient but can be accomplished by careful design, especially the taper shape parameter, R, and the metal cross-over point, z_{metal} and cut depth of the substrate, z_{cut}. These parameters are defined in Figure 3.11 in Section 3.2.6.

Tapered slot antenna theory, as mentioned in Section 3.2, presents a second size constraint in that the aperture size be greater than $\lambda/2$ for each operating frequency. If the pitch size is set to 6.2 mm the tapered slot condition is only met for the highest end of the frequency band. Simulations show that the antenna functions moderately well at the lower frequencies, and the full K-band can be adequately served.

Skin Depth

If the thickness of the copper layers on top and bottom of the substrate is comparable to the skin depth δ_s then we can ignore this factor and consider the metal loss-less. But this is not the case:

$$\delta_s = \sqrt{\frac{2}{\omega\mu\sigma}} = \sqrt{\frac{\rho}{\pi f \mu_r}} = 0.485\ \mu\text{m} \tag{3.12}$$

where ρ is the resistivity of the copper metal (1.69 x 10^{-8} $\Omega\cdot$m), f is the frequency in Hz and $\mu_r = 1$ is the relative permeability. Since the metal thickness is 17.5 μm = 36.1 δ_s, a significant value as the amplitude of the fields in the copper conductor will decay by $1/e = 36.8\%$ for each δ_s. Thus it is imperative to include an accurate value for the copper conductivity as it will affect the insertion loss and antenna efficiency values of the simulations.

3.2.3 Corrugations

Thick substrates and or high frequencies can lead to a failure of Yngvesson's condition, Equation 3.11, and result in unwanted substrate modes leading to split main beams and high sidelobes. This is a serious drawback for TSAs as they are needed to function at high frequencies and on mechanically supportive substrate thicknesses. Some techniques to overcome this problem are:

- substrate removal within the tapered aperture opening [46],
- micromachining holes or dimples into the substrate [51], and

- comb-like corrugations in the metal layers along the outer edges of the antenna [52].

The first two items, substrate removal and micromachining, reduce the effective dielectric constant eliminating the undesired surface waves for a smoother free space transition, however it results in a more fragile antenna. The third item, corrugations, work by forming an electronic band gap structure making the undesired substrate mode cut off at the operating frequency [53]. Corrugation dimensions are obtained by optimizing Sugawara's design [52] [54].

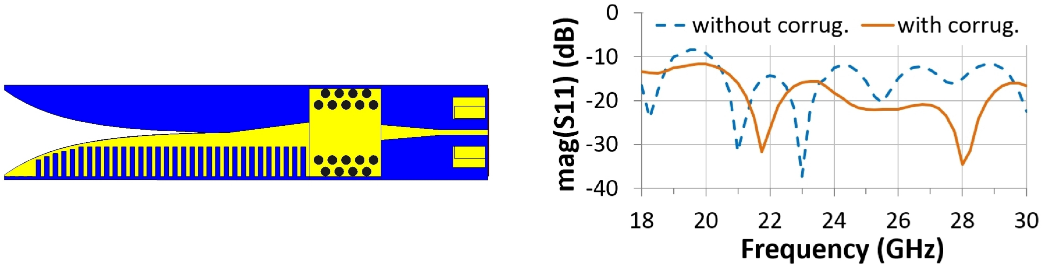

(a) Physical KPAF antenna, top, corrugations in copper layer (yellow), substrate (blue).

(b) KPAF antenna corrugation effect on $|S_{11}|$, without corrugations (dotted blue) and with corrugations (solid red).

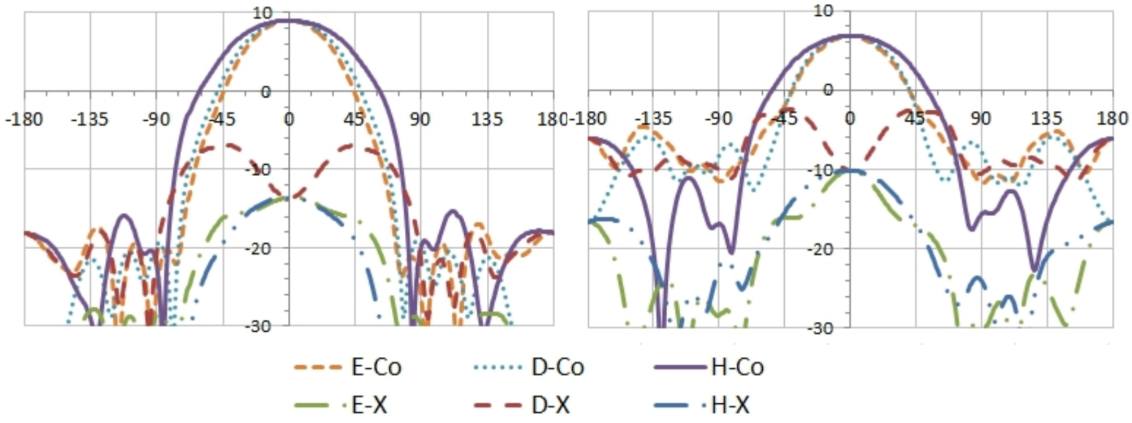

(c) Gain (dB) beam patterns vs $\theta(°)$ for parametric TSA study, Antenna 07. Left: with corrugations, right: without corrugations. E-plane $\phi = 90°$, H-plane $\phi = 0°$, D-plane $\phi = 45°$

Figure 3.5: Corrugations and effects on the TSA. (a) KPAF physical antenna, (b) $|S_{11}|$ and (c) far-field gain beam patterns for principle co-polar and cross-polar planes.

The KPAF design uses two of the above methods; a combination of the substrate removal from the tapered aperture section and corrugations in the metal layers along the outside length of the TSA in the direction of propagation. This has resulted in an absence of substrate modes, well behaved main beam and side lobes, and two unexpected features: substantially lower cross-polarization values and improved S_{11}. The physical antenna with cut-out substrate section and the corrugations can be seen in Figure 3.5 along with the effect of the corrugations on S_{11}, the far-field co-polar and cross-polar gain, and cross-polarization levels. Corrugations reduce $|S_{11}|$, increase gain from 7.0 to 9.5 dB and reduce cross-polarization levels in D-plane from -16 to -23 dB.

3.2.4 Antipodal Configuration and SIW Feed

Tapered slot antennas can be configured as uniplanar and antipodal. Uniplanar tapered slot antennas have two metallized tapers on the same side of the substrate. This is shown in Figure 3.6a [55] with a broadband microstrip feed on the bottom side. Antipodal tapered slot antennas as in Figure 3.6b have two tapers, each on opposite sides of the substrate, and lend themselves well to both microstrip and SIW feeds.

The KPAF design evolved from two previous antipodal TSA designs incorporating SIW feed, a K-band 1λ wide design [10] and a 90-120 GHz narrow beamwidth design [11]. The antipodal and SIW feed combination functioned well in these designs and was retained for KPAF.

(a) Uniplanar Vivaldi antenna with microstrip feed. Light blue: top conducting plane. Dark blue: bottom conducting plane. Substrate not shown.

(b) Antipodal Vivaldi antenna with microstrip feed. Green: top conducting plane. Magenta: bottom conducting plane. Substrate not shown.

Figure 3.6: Possible configurations

The antipodal LTSA with SIW feed has flared metallic faces on opposite sides of the substrate, matching the two-conductor SIW feed perfectly. In the SIW, the electric field is oriented perpendicular to the substrate. This is similar to the fundamental mode in an all-dielectric waveguide. As the top and bottom metallization begin to flare, the electric field, due to the changing boundary conditions, is slowly rotated to be parallel with the substrate in the antenna aperture. Note that this transition is extremely wideband and covers the entire fundamental mode range of the feeding substrate integrated waveguide. Antipodal LTSAs have poor cross-polarization performance [56] due to the non-zero transverse distance between the metal faces, allowing the small unwanted perpendicular (cross-polar) component to the co-polar field. The corrugations ameliorate this problem, leading to improved cross-polarization and reduced VSWR as seen in Figure 3.5.

The proposed feed structure is a substrate integrated waveguide (SIW) [57], an innovative planar transmission line paradigm that allows for waveguide like transmission and offers a compromise between bulky expensive waveguide and lossy planar microstrip. The SIW performs as a planar waveguide, with substrate metallized on both top and bottom surfaces and is flanked by two parallel arrays of circular via holes, which allows for a contained propagating wave. Short SIW transitions to microstrip [12, 10] or coplanar waveguide [58] are provided for integration with MMICs. The combination of planar antipodal LTSA elements and SIW feeding structure is ideally suited for array imaging systems due to its compact nature, high gain, and excellent beam symmetry and frequency scalability above 100 GHz.

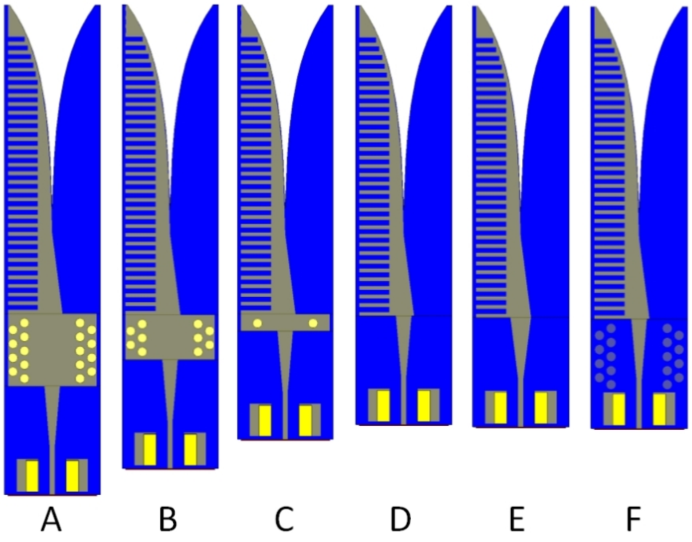

Figure 3.7: SIW and microstrip feeding arrangements investigated, A is the design for KPAF.

Alternate feed structures are investigated as illustrated in Figure 3.7 for models marked A through F. A through C differ in the number of rows of SIW holes. D and E employ only a microstrip feed; E is slightly changed so that the end of the microstrip taper is aligned with the start of the taper. F has SIW holes alongside the microstrip taper, to investigate whether confining the fields offered any benefit to $|S_{11}|$.

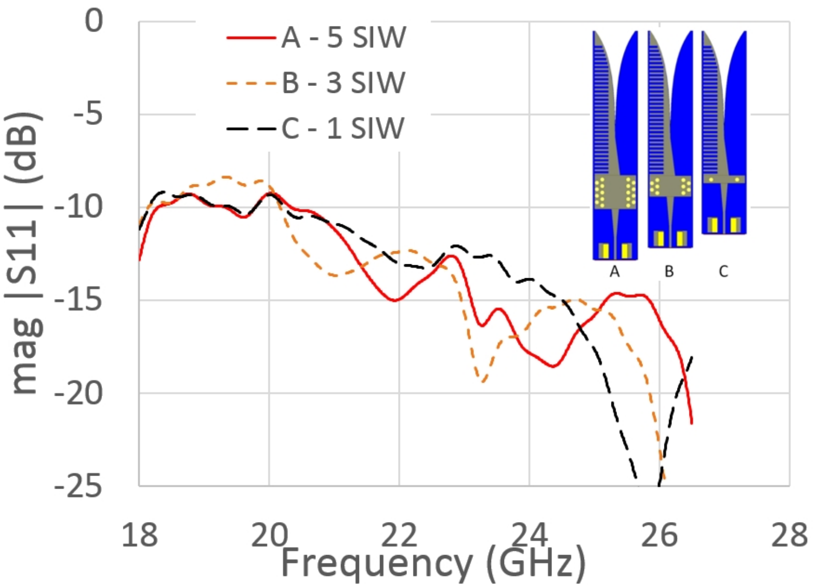

Figure 3.8: Results of SIW and microstrip feeding arrangements, models A, B and C. A is the design for KPAF.

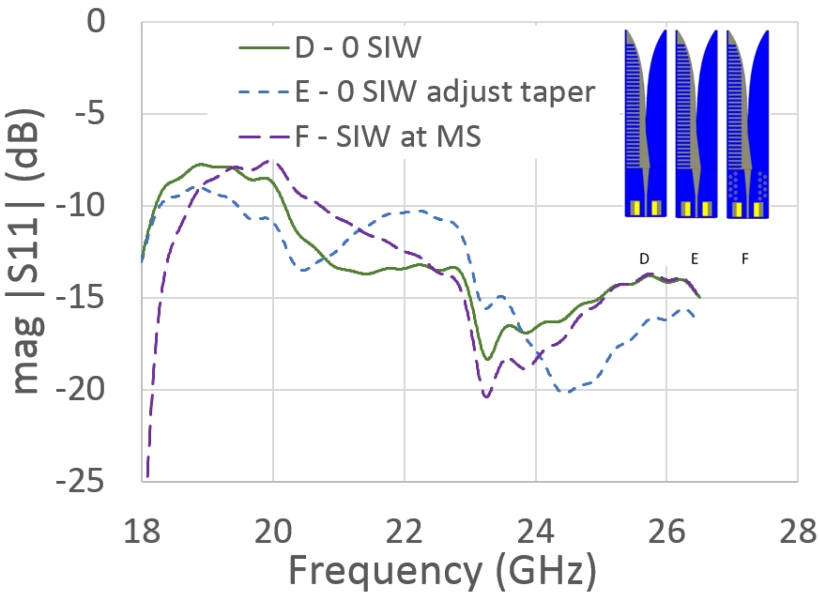

Figure 3.9: Results of SIW and microstrip feeding arrangements, models D, E and F.

The results are shown in Figures 3.8 and 3.9. Even though most other antipodal

TSAs in the literature use microstrip only [59], [60], when comparing S_{11} for the various feed configurations, the longest, A - 5 SIW, a combination of SIW and microstrip taper is selected for the best performance.

3.2.5 Taper

Given two points (y, z) on the exponential, $(y1, z1)$ and $(y2, z2)$, where y is the axis perpendicular to the axis of propagation, and z is the axis of propagation as seen in Figure 3.10, two constants, c_1 and c_2 can be calculated as:

$$c_1 = \frac{y_2 - y_1}{e^{Rz_2} - e^{Rz_1}} \tag{3.13}$$

$$c_2 = \frac{y_1 e^{Rz_1} - y_2 e^{Rz_1}}{e^{Rz_2} - e^{Rz_1}} \tag{3.14}$$

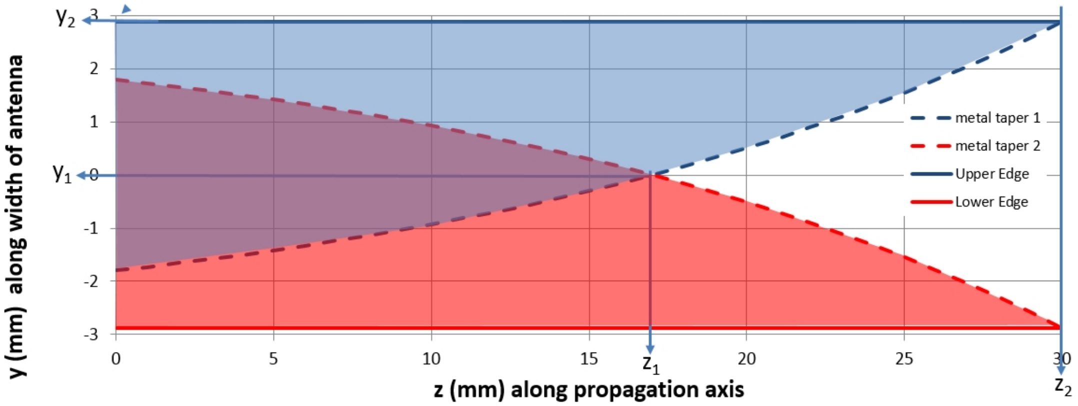

Figure 3.10: Graphing the TSA metal taper. (y_1, z_1): metal cross-over point, (y_2, z_2): endpoint of taper.

The exponential curve that forms the taper of the TSA is

$$y(z) = c_1 e^{Rz} + c_2. \tag{3.15}$$

For the parametric study antenna $R = 0.05$ and the KPAF antenna $R = 0.25$ are determined by optimization. Other tapers in the literature are Vivaldi: $R = 1$, linear: $R = 0$ and Fermi-Dirac: an exponential variant [54] [61].

3.2.6 Parametric Study

A suitable antenna element for the the KPAF antenna is needed, so this preliminary study shows the effects of certain parameters of the LTSA in Figure 3.11.

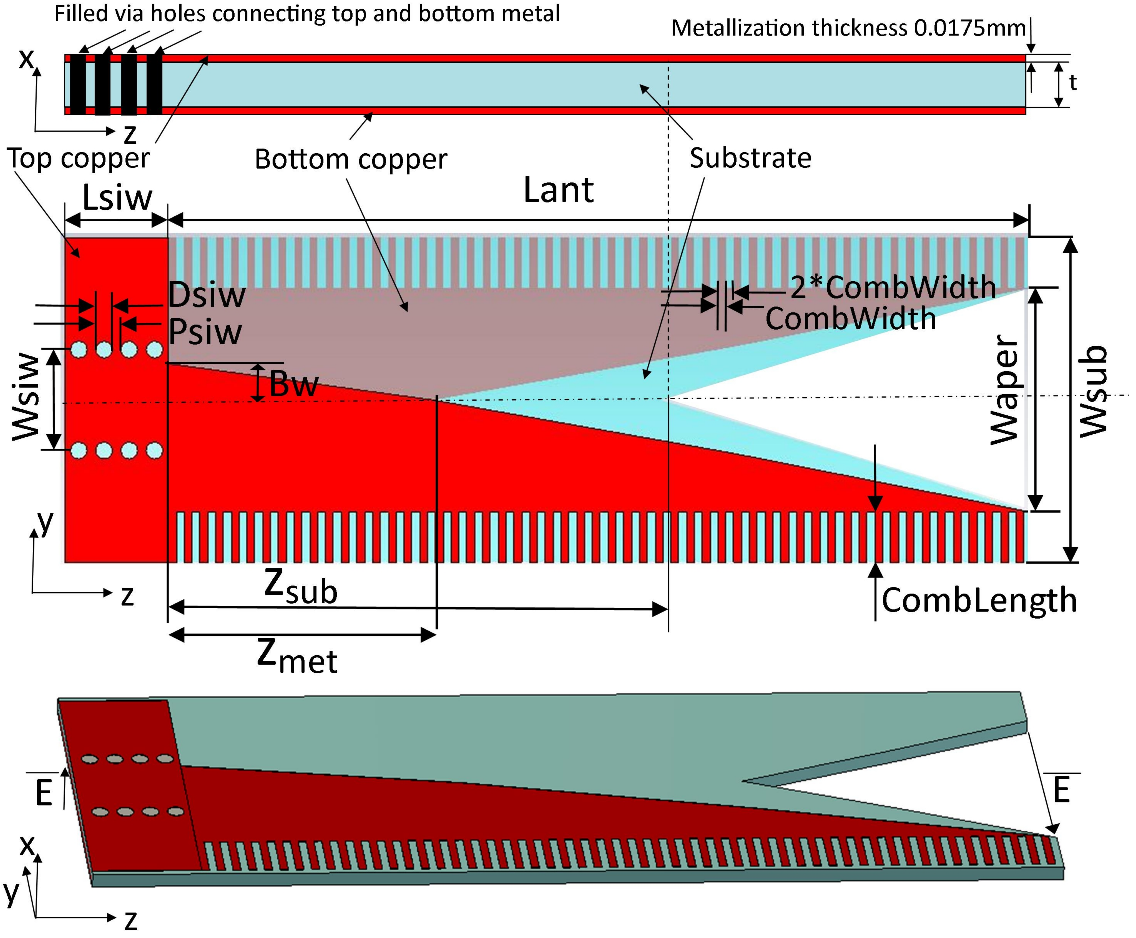

Figure 3.11: LTSA dimensions for parametric study. Top: side view, copper layers (red), and Rogers 6010LM substrate, $\varepsilon_r = 10.2$ (blue). Middle: Top view with slightly transparent substrate to visualize antipodal placement of copper flared layers, and cut substrate. Bottom: Perspective view. E-vector is vertical at SIW feed and rotates through 90° along the antipodal copper flares to the aperture.

The parameters in Figure 3.12 include the antenna length, L_{ant}, the antenna width, W_{sub}, and the aperture width, W_{aper}, while keeping constant the substrate thickness, t, the SIW feed configuration and the corrugation dimensions.

The eight designs, Antennas 01 through 08, and variables including the aspect ratio of L_{ant} to W_{aper} follow in Figure 3.13. Antennas 01-04 have constant length and varying aperture width: aspect ratios vary from the highest 16:1 to the lowest 11:1.

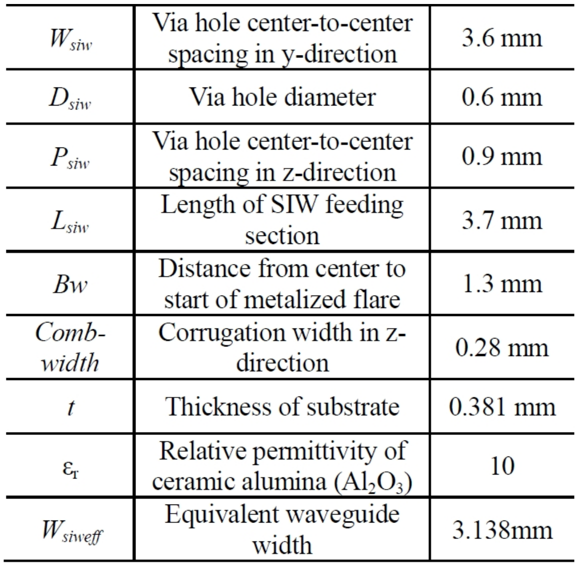

W_{siw}	Via hole center-to-center spacing in y-direction	3.6 mm
D_{siw}	Via hole diameter	0.6 mm
P_{siw}	Via hole center-to-center spacing in z-direction	0.9 mm
L_{siw}	Length of SIW feeding section	3.7 mm
Bw	Distance from center to start of metalized flare	1.3 mm
Comb-width	Corrugation width in z-direction	0.28 mm
t	Thickness of substrate	0.381 mm
ε_r	Relative permittivity of ceramic alumina (Al_2O_3)	10
W_{siweff}	Equivalent waveguide width	3.138mm

Figure 3.12: Antenna and feed constants for LTSA parametric study.

Antennas 05-08 have varying length and constant aperture width: aspect ratios vary from the highest, 8:1, to the lowest, 3:1.

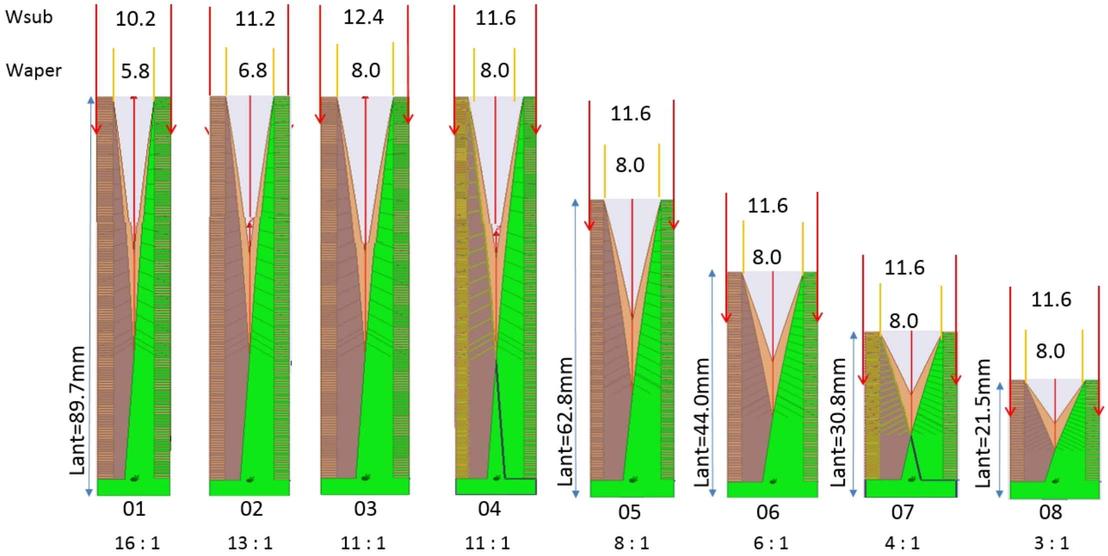

Figure 3.13: Antennas 01 to 08 dimensions for parametric study. W_{sub} (mm) is the antenna width, W_{aper} (mm) is the aperture width. L_{ant}, the length of the antenna is noted as well as the aspect ratio L_{ant}:W_{aper} along the bottom.

All eight designs are simulated with the Ansys HFSS frequency domain solver, which uses the finite element technique, over an extended K (18 - 30 GHz) frequency band.

Results

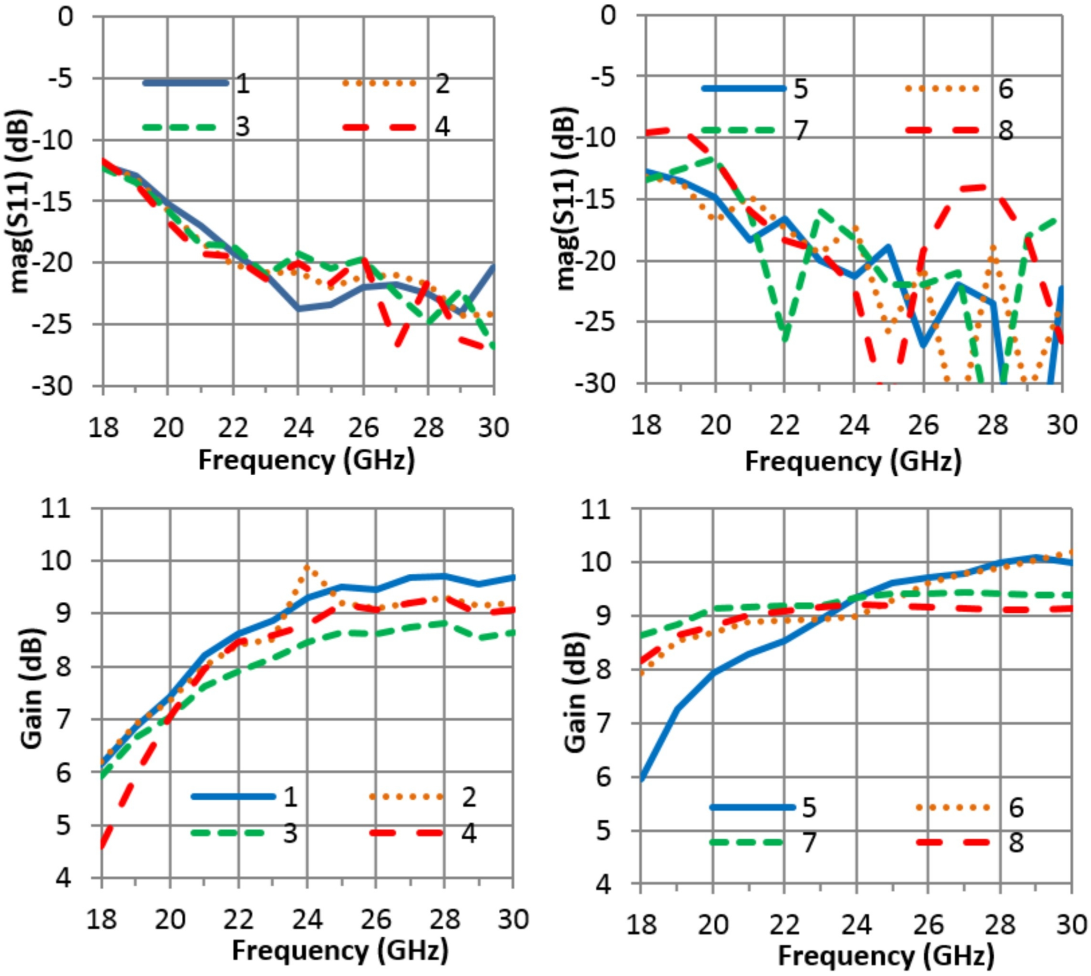

Figure 3.14: Parametric study results: $|S_{11}|$ and Gain for antennas 1 to 8.

From the graphs in Figures 3.14, 3.15 and 3.16 it can be concluded:

$|S_{11}|$ is generally better with higher aspect ratios. This is expected with travelling wave antennas as the reflections have more time to die out and produce a better termination for the wave.

Gain is relatively insensitive to antenna length at higher frequencies, but at lower frequencies increases dramatically for decreasing aspect ratios.

Gain flatness over the frequency band is maximized with small aspect ratio, (6:1 and lower).

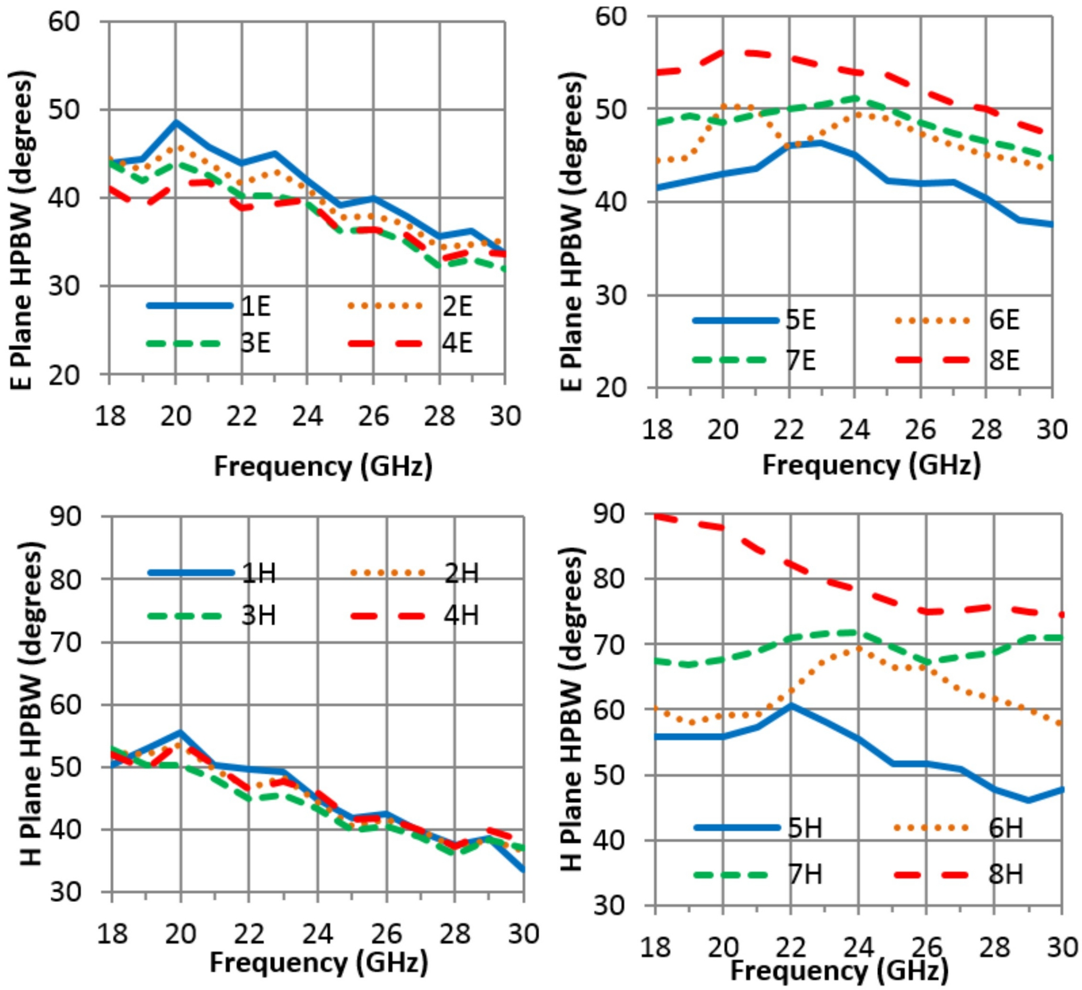

Figure 3.15: Parametric study results: HPBW for antennas 1 to 8.

E- and H-plane HPBWs The HPBW for E- and H-planes are weakly proportional to aspect ratio as seen in 3E, 4E and 3H, 4H. The HPBW for E- and H-planes are inversely proportional to antenna length as seen in 5E-8E and 5H-8H. They may also be dependent on the taper angle, but since this variable cannot be decoupled from the antenna length, further studies are required for verification.

Beam symmetry, $\mathbf{HPBW_E/HPBW_H}$ is maximized with a high length:width aspect ratio. For Antenna 01 with highest aspect ratio 16:1, the beam symmetry is the highest, 0.91. As the aspect ratio is reduced, so too is the degree of beam symmetry, as found in [47].

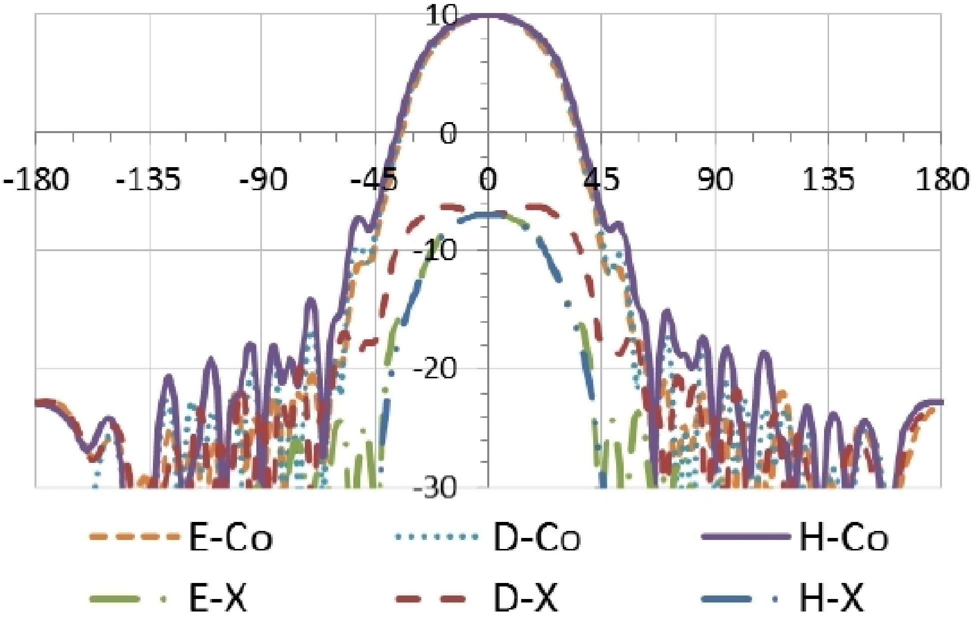

(a) Design 1 - Gain

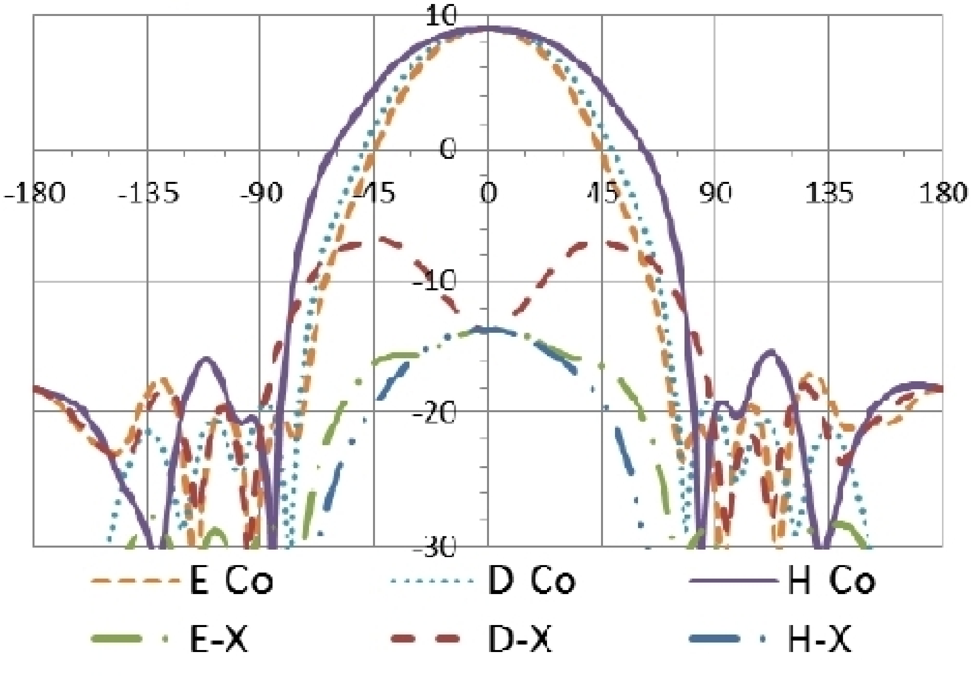

(b) Design 7 - Gain

Figure 3.16: Parametric study results: Gain (dB) beam patterns vs $\theta(^\circ)$ for (a) Design 1 and (b) Design 7 including principle co-polar and cross-polar planes: E-plane $\phi = 90^\circ$, H-plane $\phi = 0^\circ$, D-plane $\phi = 45^\circ$.

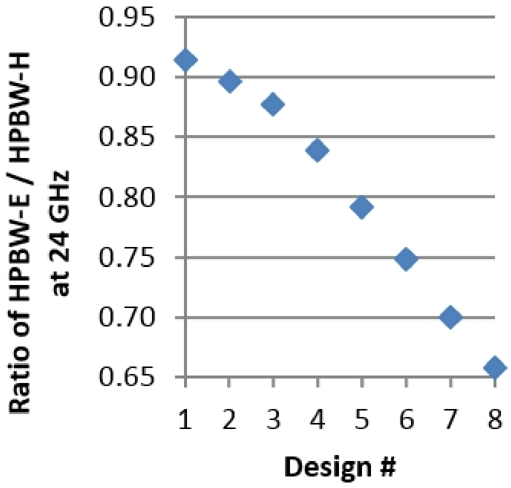

Figure 3.17: Parametric study results: Beam symmetry for Designs 1 to 8. E to H plane beam symmetry is highest, i.e. most circularly symmetric, for Design 1.

3.3 KPAF Design

3.3.1 Requirements

With insight gained from the parametric study, the KPAF antenna array element was designed that includes a feeding structure and coaxial transition to connect with standard coaxial cable. The physical antenna requirements are:

- 5.75 mm wide element (0.5 λ to avoid grating lobes)
- minimize loss for maximum antenna efficiency
- feeding structure to minimize input reflections and allow for a miniSMP coaxial connection

The antenna RF/farfield performance requirements are

- full K-band (18 - 26 GHz) frequency coverage
- wide ($> 90°$) HPBW to efficiently illuminate a moderate F/D = 0.45 focal length primary reflector
- axially symmetric (equal E- and H-planes) beams to maximize FoV on sky
- moderate gain (5 - 10 dB)

3.3.2 Design Summary

A tapered slot antenna, a type of travelling wave antenna, was fabricated on microstrip substrate, as this provided an inexpensive design, allowed a narrow 6.2 mm profile, and can be integrated with MMIC and coaxial components, and can be easily manufactured into arrays. The substrate chosen is 0.381 mm (15 mil) Rogers RT Duroid 6010 LM ($\epsilon_r = 10.2$, $\tan\delta = 0.003$ at 20 GHz). The high dielectric permits a $\lambda/2$ element width = 6.2 mm satisfying the grating lobe condition. The 0.381 mm substrate thickness creates unwanted substrate modes that are eliminated using comb-like corrugations to form an electronic band gap structure cutting off the substrate mode at the operating frequency [53]. Also, thick substrates incur added insertion loss. The loss can be reduced by cutting away the substrate material in the aperture opening using a 355 nm UV laser with a 2 mil kerf and 35 μm beam.

The antipodal configuration of the top and bottom metallic tapers matches the two-conductor substrate integrated waveguide (SIW). The SIW section allows for a waveguide-like transmission line carrying a TE_{10} mode [57]. Like rectangular waveguide, the SIW can work single-mode from slightly above the cutoff frequency, f_c, to 2 f_c, i.e. 15.1 GHz to 30.2 GHz, easily covering the full K-band. Note there are no TM modes owing to the non-continuous waveguide walls by the discrete vias.

This is followed by a tapered microstrip section to standard 50 Ω microstrip line and then a Rosenberger miniSMP connector. Custom Rosenberger RTK Flex405 low loss coaxial cable with miniSMP connector is used on the antenna end and K-type male on the other for connection to the amplifier.

The designed antenna is drawn in Figure 3.18, the manufactured antennas and calibration circuits are in Figure 3.19 and the design variables defined in Table 3.1.

3.3.3 Grounding Issue

A small grounding problem in all the calibration circuits and antennas was discovered when passing a copper bar near the underside of the microstrip, supposedly grounded, seen in Figure 3.20. Originally, the only connection to microstrip ground was through the two via holes flanking the miniSMP connector. Since the outer shell of the gold-plated miniSMP is also ground, soldering it directly to the microstrip ground plane solved the problem and dramatically improved the effectiveness of the calibration standards and the KPAF antenna measurement.

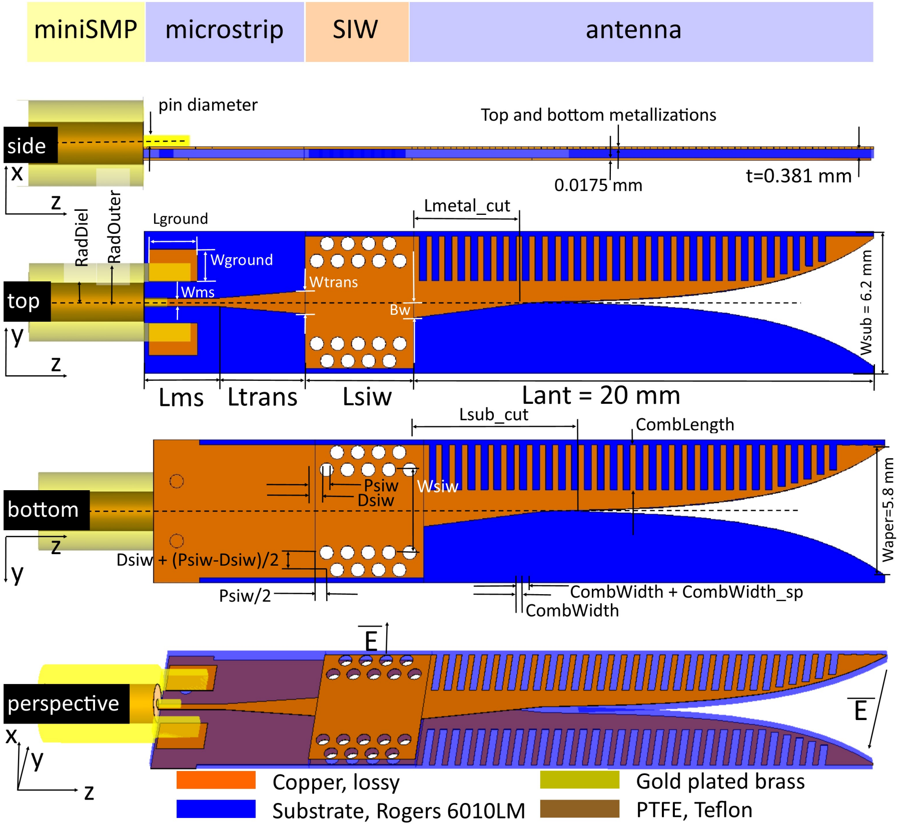

Figure 3.18: KPAF antenna, SIW feed, microstrip taper, miniSMP connector dimensions, 2D projections and perspective view. All dimensions to scale except top and bottom copper metalizations.

3.3.4 Calibration

In any vector network analyzer (VNA) measurement, it is advisable to calibrate out the effects of the VNA itself and any cables and components used in order to make a better measurement of the device under test (DUT).

The measurement setup includes the VNA, precision grade coaxial cable with V-connector[2] ends, V-K adaptor, coaxial cable with miniSMP end and the KPAF antenna with miniSMP plug. Ideally, the calibration plane should be placed so that

---

[2] The 2.92 mm connector, also known as the K-connector, was named as such by Wiltron, now Anritsu, because it covers all the K-bands, i.e. it is useable up to 40 GHz. The 1.85 mm connector, also known as the V-connector, was named by Anritsu because it covers the V frequency band, i.e. up to 60 GHz.

Table 3.1: KPAF variables from Figure 3.18. Coordinate(s) indicated in parenthesis.

Variable	**Value**	**Description**
Bw	0.669 mm	distance from centre to edge of taper (y)
CombLength	1.1 to 1.8 mm	lengths of corrugation (y)
CombWidth	0.24 mm	metal on corrugation (z)
CombWidthsp	0.32 mm	space between corrugations (z)
Dsiw	0.6 mm	via hole diameter (y and z)
Lground	2.3 mm	length of ground pad (z)
Lmetalcut	5.2 mm	distance to virtual metal cross-over point (z)
Lms	3.0 mm	length of constant-width microstrip (z)
Lsiw	4.7 mm	length of SIW section (z)
Lsubcut	6.8 mm	distance to substrate cut-point (z)
Ltrans	4.0 mm	length of microstrip taper (z)
Psiw	0.9 mm	via hole period (z)
RadDiel	0.838 mm	coaxial cable dielectric radius (x,y)
RadOuter	1.70 mm	mini-SMP outer diameter (x,y)
t	0.381 mm	thickness of substrate (x)
tmetal	0.0175 mm	thickness of copper metalization (x)
Waper	5.55 mm	aperture width (y)
Wground	1.4 mm	width of ground pad (y)
Wms	0.32 mm	width of constant-width microstrip (y)
Wsiw	3.6 mm	distance between vias across SIW section (y)
Wsub	5.75 mm	width of substrate (y)
Wtrans	1.0 mm	maximum width of microstrip taper (y)

all cables and the microstrip transition and the SIW section are removed.

There are three possible calibrations for the KPAF antenna circuit, the SOLT, the de-embedded calibration, and the SSST. Both the SOLT and the SSST are capable of performing a full 2-port calibration defining all 12 error terms, however, the SSST uses all three offset short standards to define the source match and reflection tracking providing a more accurate reflection measurement of the one port antenna, whereas the SOLT only uses two, the Short and Open [62]. The SSST is a more accurate calibration at higher frequencies than SOLT [63]. For these reasons the SSST is the recommended calibration for the KPAF antenna.

The de-embedded calibration provides only a transmission calibration, which is simpler to perform, but does not provide any reflection information. Each calibration option will be described further and the resulting calibration planes shown in

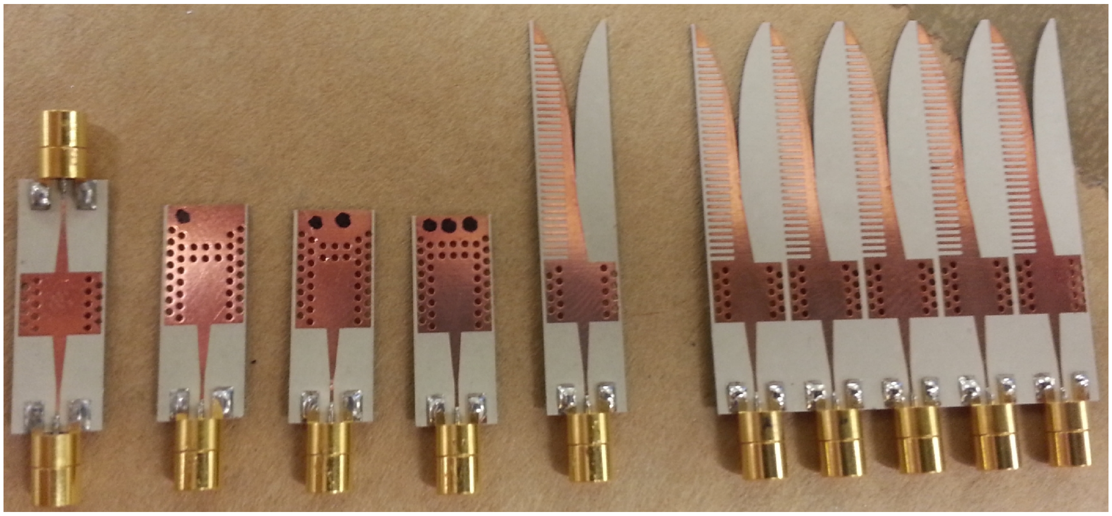

(a) top side

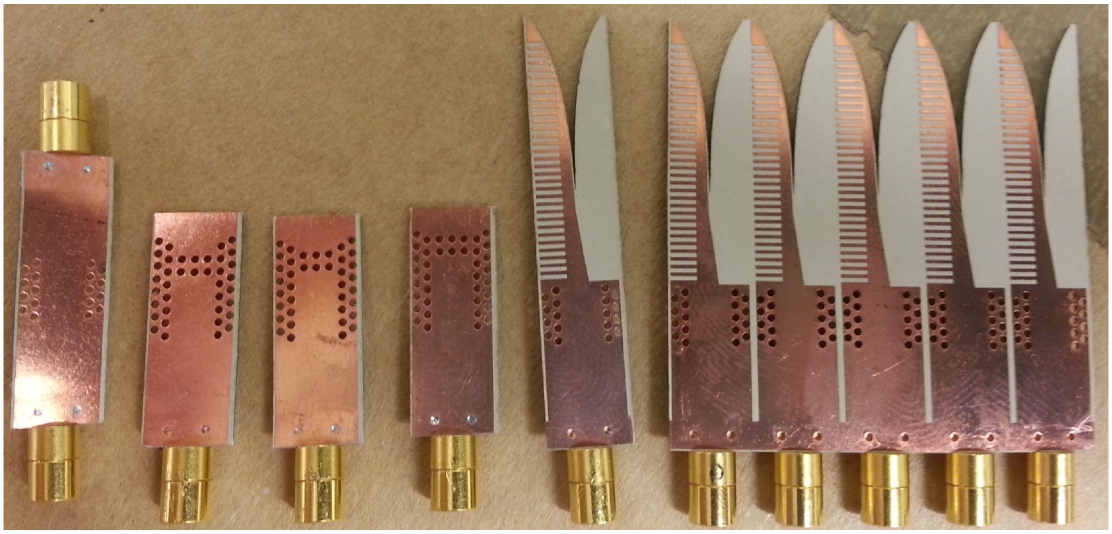

(b) bottom side

Figure 3.19: Manufactured calibration circuits and DUTs (antennas) with soldered miniSMP connectors. L to R: Thru (4.7 mm), Short 1 (4.7 mm), Short 2 (5.13 mm), Short 3 (5.65 mm), single antenna, 1x5 antenna array.

Figure 3.21.

1. Standard Coaxial SOLT (Short Open Load Through) calibration.

    - Standards used: Short (coaxial, K), Open (coaxial, K), 50Ω load (coaxial, K).
    - Degree of calibration: Full 2 port (all 12 parameters), $|S_{11}|$, $|S_{12}|$, $|S_{21}|$, $|S_{22}|$

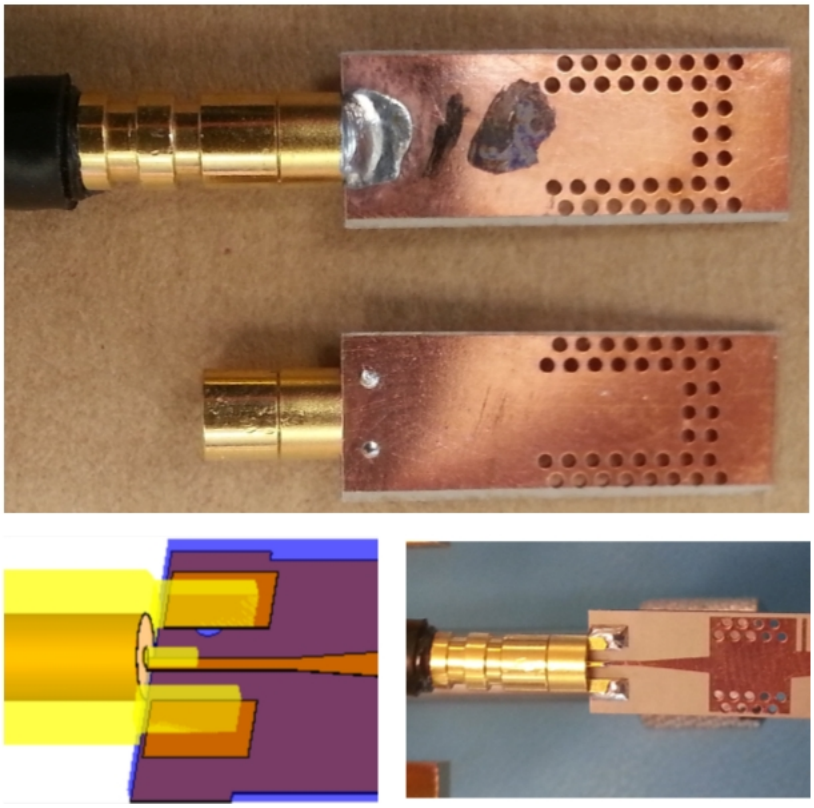

Figure 3.20: Solving the grounding problem in the SSST calibration standards. Top: Bottom view of Short1 standard with grounding problem solved using a solder connection between miniSMP cable housing and microstrip ground plane. Original Short1 below. Bottom left: Original grounding only through via holes to gold plated tabs common to the connector housing. Bottom right: miniSMP ground tabs soldered to via holes.

- DUT: small coax + miniSMP + microstrip transition + SIW + antenna
- Calibration Plane: end of V-K adapter

The K connector at the end of the precision coaxial cable offers a convenient point to perform a standard full 2-port coaxial SOLT calibration as the K-connector calibration kit is readily available. This offers a quick sanity check for the system as it removes the effects of the VNA and the loss in the precision coaxial cable. However, this is insufficient to accurately characterize the antenna as the effects of the second coaxial cable and miniSMP connector, microstrip and SIW are still masking the antenna performance; it is just good enough to see if it is working. Let's move the calibration plane further in to get closer to having the antenna only.

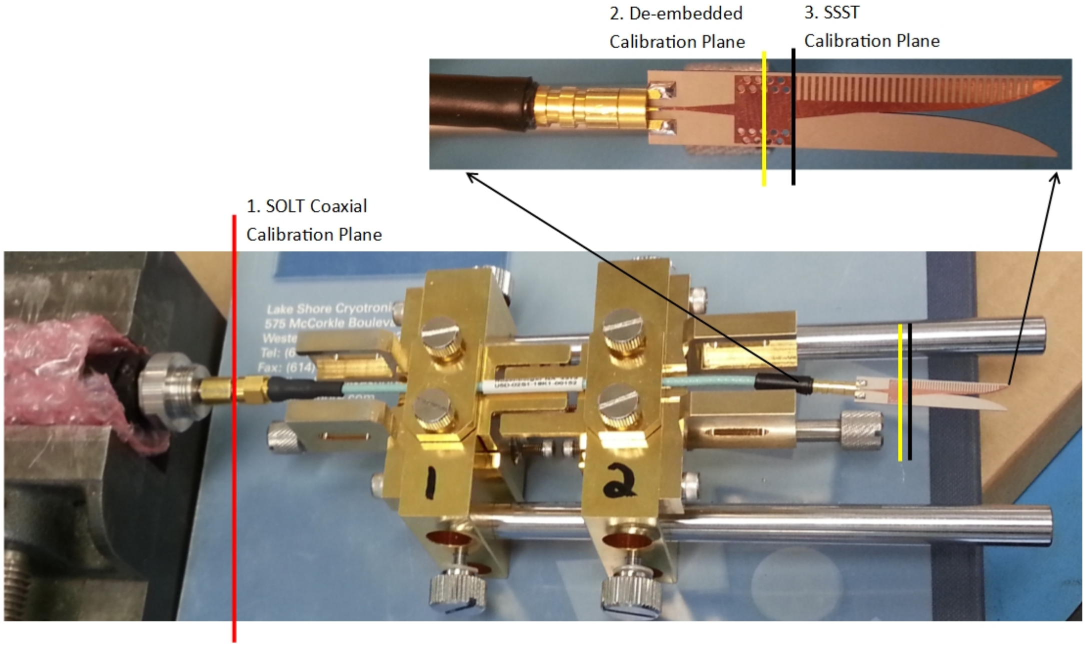

Figure 3.21: Calibration options for VNA measurements and the associated calibration planes.

2. De-embedded Calibration

   - Standards used: SOLT coaxial standards as in no.1. at the V-K transition point, and microstrip THRU
   - Degree of Calibration: A transmission calibration, only $|S_{21}|$ parameter is valid.
   - DUT1: small coax + miniSMP + microstrip transition + SIW + antenna
   - DUT2: small coax + microstrip THRU + small coax
   - Calibration Plane: midway through SIW section before antenna.

   The de-embedded calibration uses two sequential calibrations to move the calibration plane so that only half of the SIW plus the antenna is included.

   Assuming that the DUT2 is well matched and symmetrical, a good assumption, the calibration plane can be calculated and placed directly in the centre of DUT2. This places the plane at the yellow line in Figure 3.21. However, since only one standard, the THRU was used for this second calibration, it is basically only a transmission calibration, so only $|S_{21}|$, $|S_{12}|$ are valid, and the reflection values are highly suspect. The goal is to measure $|S_{11}|$ of the antenna, so this calibration is not useful beyond proving that the manufactured custom THRU standard performs well.

3. SSST Calibration - Custom Microstrip Calibration
    - Standards used: SHORT1, SHORT2, SHORT3 (custom microstrip)
    - Degree of Calibration: Full 2 port, $|S_{11}|$, $|S_{12}|$, $|S_{21}|$, $|S_{22}|$
    - DUT: Antenna only
    - Calibration Plane: at intersection between SIW and antenna

Using the SSST (triple short) calibration technique, three slightly different length shorts are used to determine all 12 error terms of the calibration model. SHORT1 has the shortest length and SHORT3 the longest.

$$a = L_{SHORT2} - L_{SHORT1} \tag{3.16}$$

$$b = L_{SHORT3} - L_{SHORT2} \tag{3.17}$$

$$20^\circ < A = \frac{a \cdot f \cdot 720^\circ}{v_{ph}} < 90^\circ \tag{3.18}$$

$$20^\circ < B = \frac{b \cdot f \cdot 720^\circ}{v_{ph}} < 90^\circ \tag{3.19}$$

$$20^\circ < (A + B) = \frac{(a + b) \cdot f \cdot 720^\circ}{v_{ph}} < 160^\circ \tag{3.20}$$

where a and b are in [m], A and B are in [°], $v_{ph} = \lambda_g / f, \lambda_g = \frac{c\sqrt{\varepsilon_r}}{\sqrt{f^2 - f_c^2}}$, and f_c = cutoff frequency

Frequency (GHz)	**A(°)**	**B(°)**
18	33	40
22	53	65
26	70	85

Table 3.2: SSST calibration phase lengths

If $a = 0.43$ mm and $b = 0.52$ mm and given that the SIW section to be calibrated out is 4.70 mm, the resulting shorts are SHORT1 = 4.70 mm, SHORT2 = 5.13 mm and SHORT3 = 5.65 mm. The electrical lengths in degrees of A and B for 18, 22 and 26 GHz are calculated in Table 3.2.

The advantage of using the SSST calibration is that it is highly accurate as long as the common sections of the circuits are perfectly the same. And except for the solder connection at the mini-SMP - microstrip boundary, and any differences incurred when attaching the three standards during the calibration, this is true.

The calibration plane is now brought up to the transition between the SIW section and the antenna, an ideal place in order to characterize the antenna alone.

3.3.5 S-parameters

The RF setup includes: Anritsu 37397C (40 MHz - 65 GHz) vector network analyzer with V-male type connector, precision standard cables with V(f)/V(m) connectors, V(f) to K(f) adapter, the Rosenberger coaxial cable with K(m) and miniSMP(m) connectors, and the KPAF antenna with miniSMP(f) connector. A sleeve of absorber in Figure 3.22 is placed around the antenna to prevent any stray signals from the environment affecting the measurement. The $|S_{11}|$ of the single KPAF antenna is measured while the antenna is covered with ambient temperature absorber.

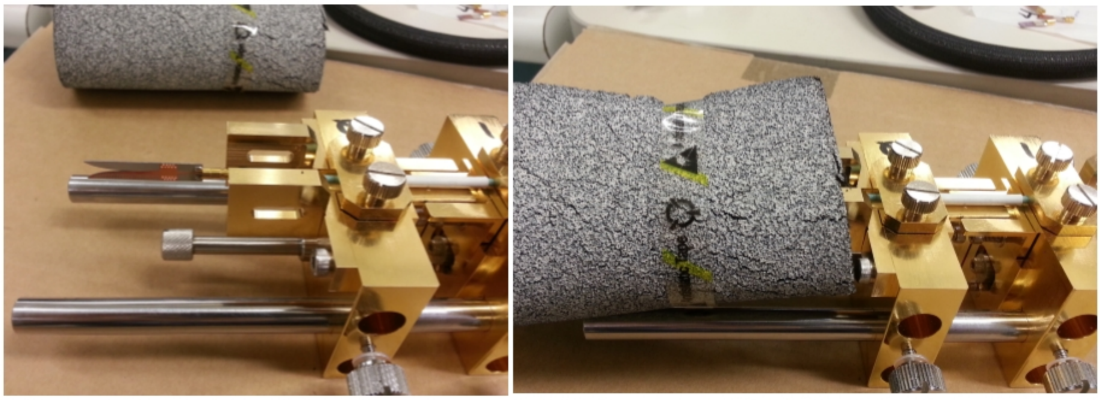

Figure 3.22: KPAF VNA setup (left) and with absorber around antenna (right) to prevent stray radiation from disturbing the S-parameter measurements.

The calibration for this measurement was Option 3: SSST. Using the three custom made shorts, the resulting DUT is the antenna section only. The microstrip, SIW section and all cables are removed by the calibration.

Measured results for the antenna only are shown in Figure 3.23a along with three simulated results; two from CST and one from HFSS. The simulations are from CST Microwave Studio's frequency domain solver, the time domain Finite Integration Technique (FIT) solver, and Ansys HFSS's frequency domain Finite Element Method (FEM) solver.

Figure 3.23b shows that adding the SIW section, the microstrip taper and the ground tabs has minimal effect on the existing antenna performance, when comparing similar solver results.

3.3.6 Radiation Patterns

The KPAF single antenna's gain pattern is measured using both near-field and far-field scanner systems.

Near Field Scanner Measurement

Near-field techniques involve the acquisition and processing of two complex, nearly orthogonal polarization components along a particular coordinate system. The near field data set is converted to far-field by the mathematical Fourier transform. The disadvantage to near-field methods is the limited scan angle off boresight for low-directive antennas. Still, they allow testing in a physically small area resulting in improved climate-control, security and accuracy.

As shown in Figure 3.24, the system used is the Nearfield Systems Inc. (NSI) planar near-field scanner, model 300V-6x6, located in the millimetre lab at NRC Herzberg, Victoria, with scan area of 2 m x 2 m covered with absorber material. A 0.3 m x 0.3 m piece of absorber is placed around a WR42 K-band waveguide probe. The probe is connected to a waveguide variable attenuator and a Narda waveguide to coaxial transition, Model 4608, 18 - 26 GHz, both mounted on the underside of the absorber. The probe scans a plane in front of the antenna under test (AUT), a single KPAF antenna mounted vertically.

As mentioned there are angular limitations for the KPAF antenna. The region ±70° away from boresight is included in the calculated far-field beam, and any energy outside of this will effectively confuse and distort the true far-field beam, so this region was protected with absorber material. Despite this, the ability to compare the calculated radiation patterns to other far-field techniques makes it a useful

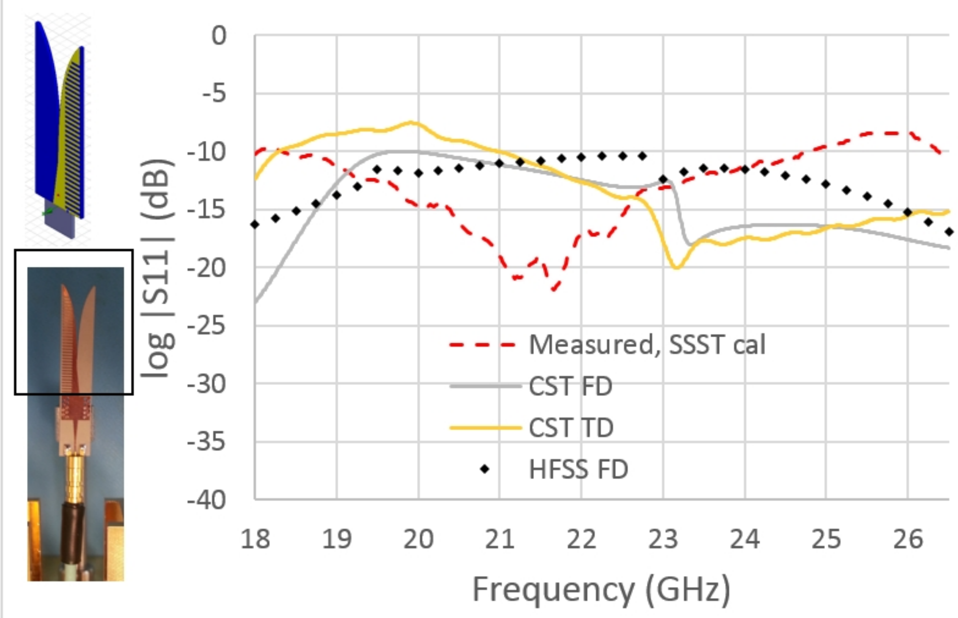

(a) KPAF antenna only

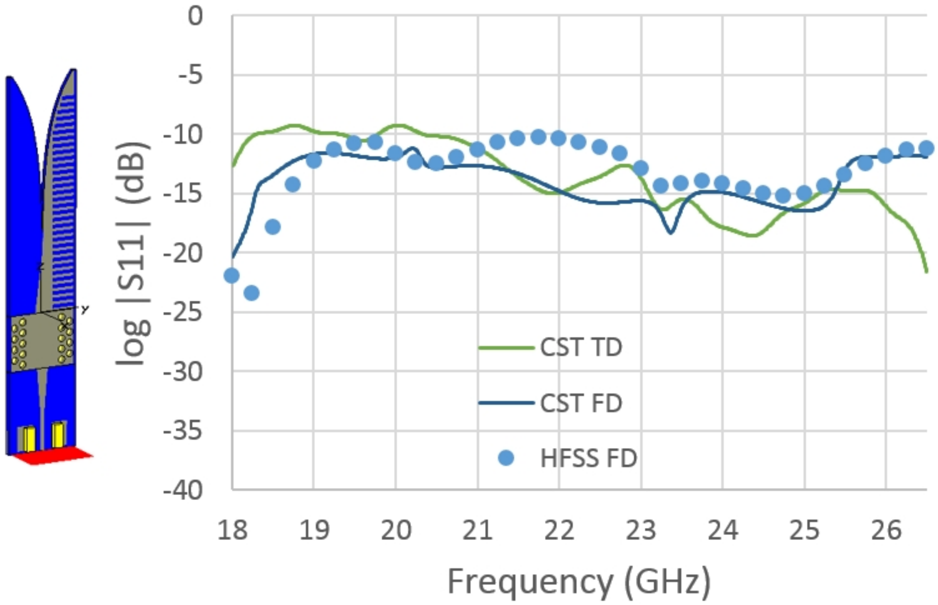

(b) KPAF antenna plus SIW, microstrip and ground tabs.

Figure 3.23: KPAF antenna $|S_{11}|$ simulated and measured. SSST calibration removes all contributions except that outlined with black rectangle.

experiment.

The separation distance between the AUT and probe should be in between the near-field and far-field distance of the AUT to ensure evanescent (non-propagating)

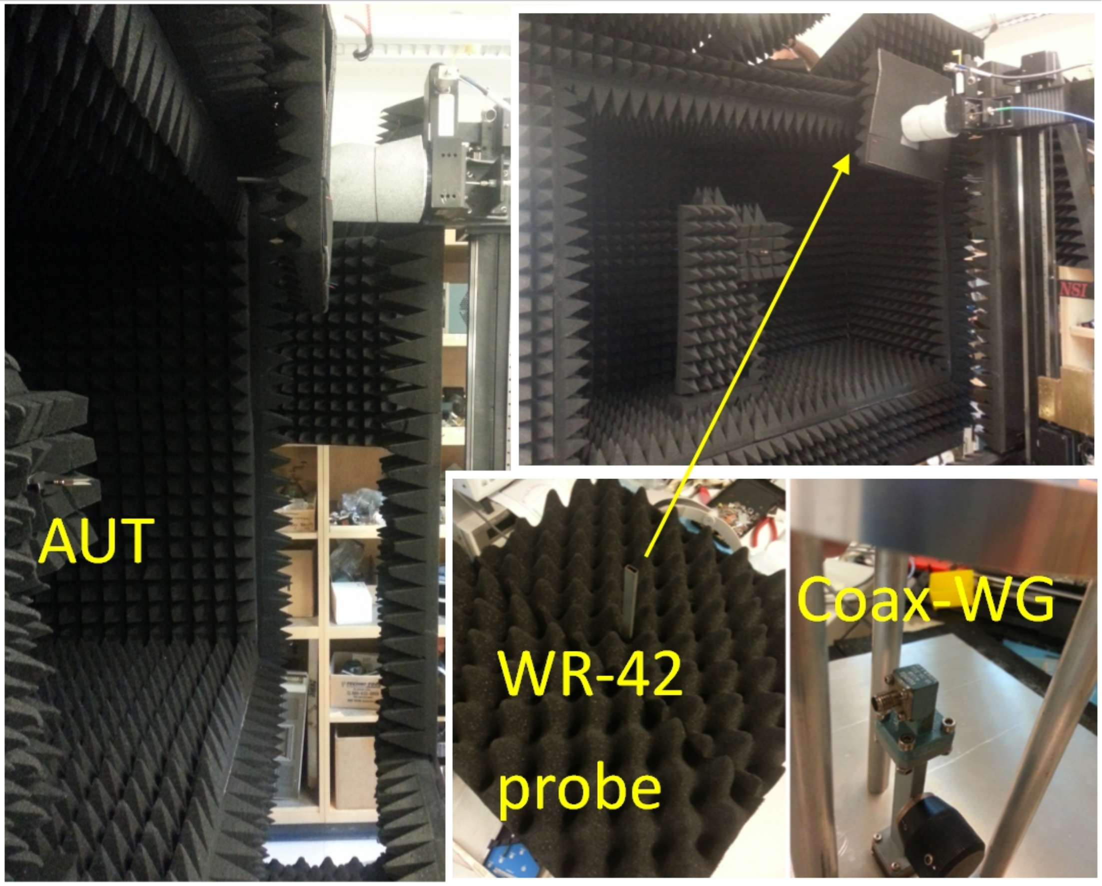

Figure 3.24: Near-field testing setup at NRC Herzberg. The antenna under test (AUT) is the vertically mounted stationary KPAF antenna. The moveable probe is a WR42 rectangular waveguide scanning a rectangular 2 m x 2 m region. The probe connects to a waveguide variable attenuator and a waveguide to coax transition.

modes are not significantly contributing to the measured near-field data. The near- and far-field distances for the array antenna with maximum dimension $d = 31$ mm at the minimum wavelength $\lambda = 11.5$ mm are

$$R_{near} = 0.62 \times \sqrt{d^3/\lambda} = 32 \text{ mm} \tag{3.21}$$

$$R_{far} = \frac{2d^2}{\lambda} = 167 \text{ mm}. \tag{3.22}$$

Therefore, any AUT-probe distance between 32 and 167 mm will be valid. The antenna is measured at 18 GHz with AUT-probe distance 110 mm and at 20 GHz with AUT-probe distance 155 mm. This corresponds to a maximum far-field angle of +/- 75° and +/- 70°, respectively. Since the expected HPBW of the KPAF antenna exceeds this, only the data within this region should be valid. The network analyzer on the near-field system limited the upper frequency to 20 GHz, so only radiation patterns at 18 and 20 GHz are taken. Usual near-field measurement practice is to make multiple measurements where the scanning planes are separated by $\lambda/4$, calculate the far-field for each measurement and compute the difference [64]. This is done internally by the NSI software in order to minimize reflections caused when some of the probe signal scatters multiple times to the AUT and back.

The near-field scanning measurement results are graphically depicted in Figure 3.25 for 110 mm AUT distance at 18 GHz and in Figure 3.26 for 155 mm AUT distance at 20 GHz. In each figure the near-field patterns are (a, b, e) and the far-field patterns are (c, d, f). The near-field patterns are used as a sanity check to ensure proper operation of the far-field calculations. For both near- and far-field patterns, gain is normalized to the peak value at boresight and is in units of dB and the graphs descriptions are:

- a. Near-field co-polar gain, 2D raster, axes: X (m), Y (m)
- b. Near-field cross-polar gain, 2D raster, axes: X (m), Y (m)
- c. Far-field co-polar gain, 2D raster, axes: azimuth (°), elevation (°)
- d. Far-field cross-polar gain, 2D raster, axes: azimuth (°), elevation (°)
- e. Near-field co-polar gain, E- and H-plane cuts from a., axes: X (m), gain (dB)

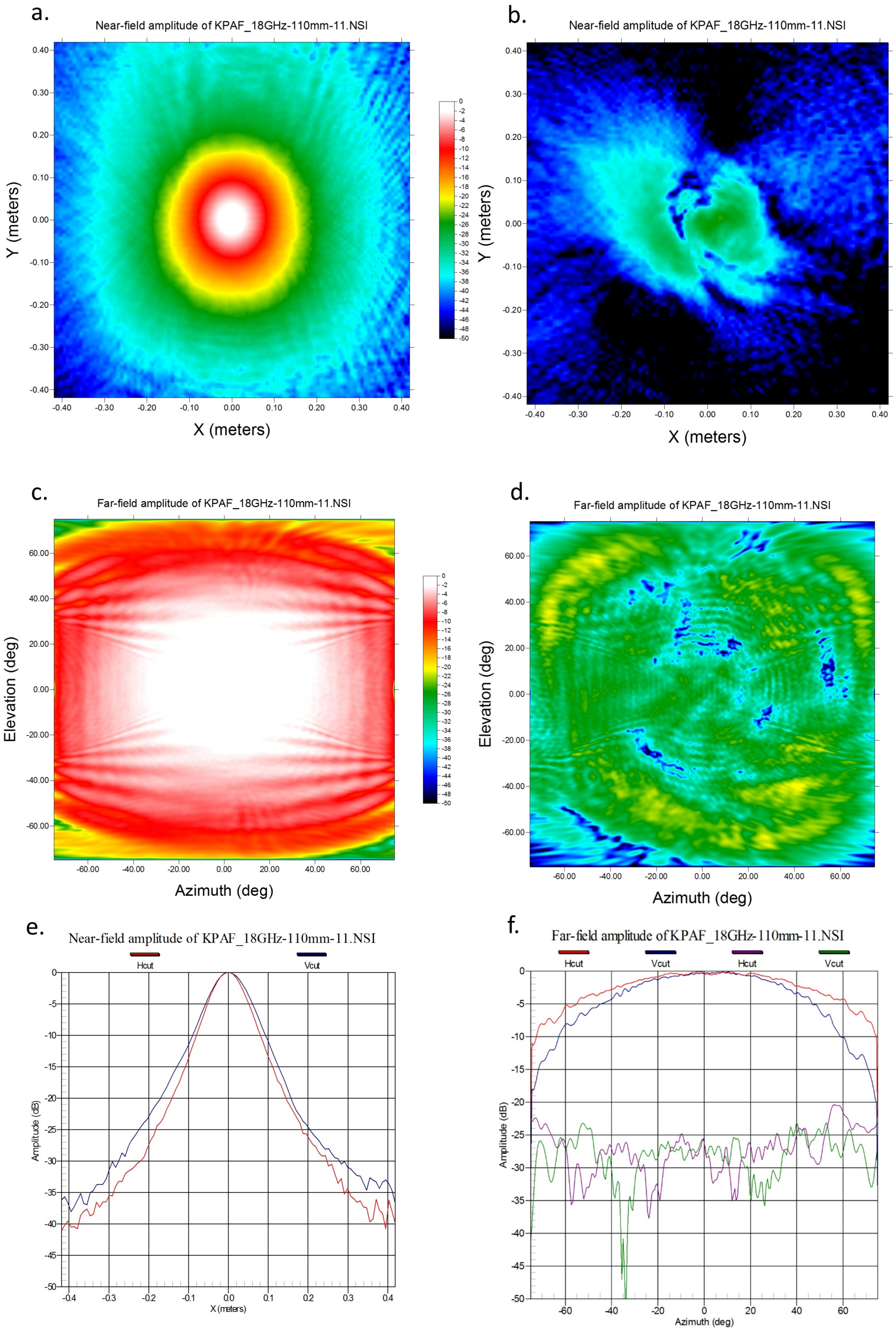

Figure 3.25: 18 GHz near-field: (a, b, e) and far-field: (c, d, f) radiation patterns from near-field scanning measurement, single KPAF antenna. Near-field 2D raster: (a) co-polarization and (b) cross-polarization. Far-field 2D raster: (c) co-polarization and (d) cross-polarization. E- and H-plane cuts: (e) near-field co-polarization and (f) far-field co- and cross-polarization. AUT-probe distance 110 mm.

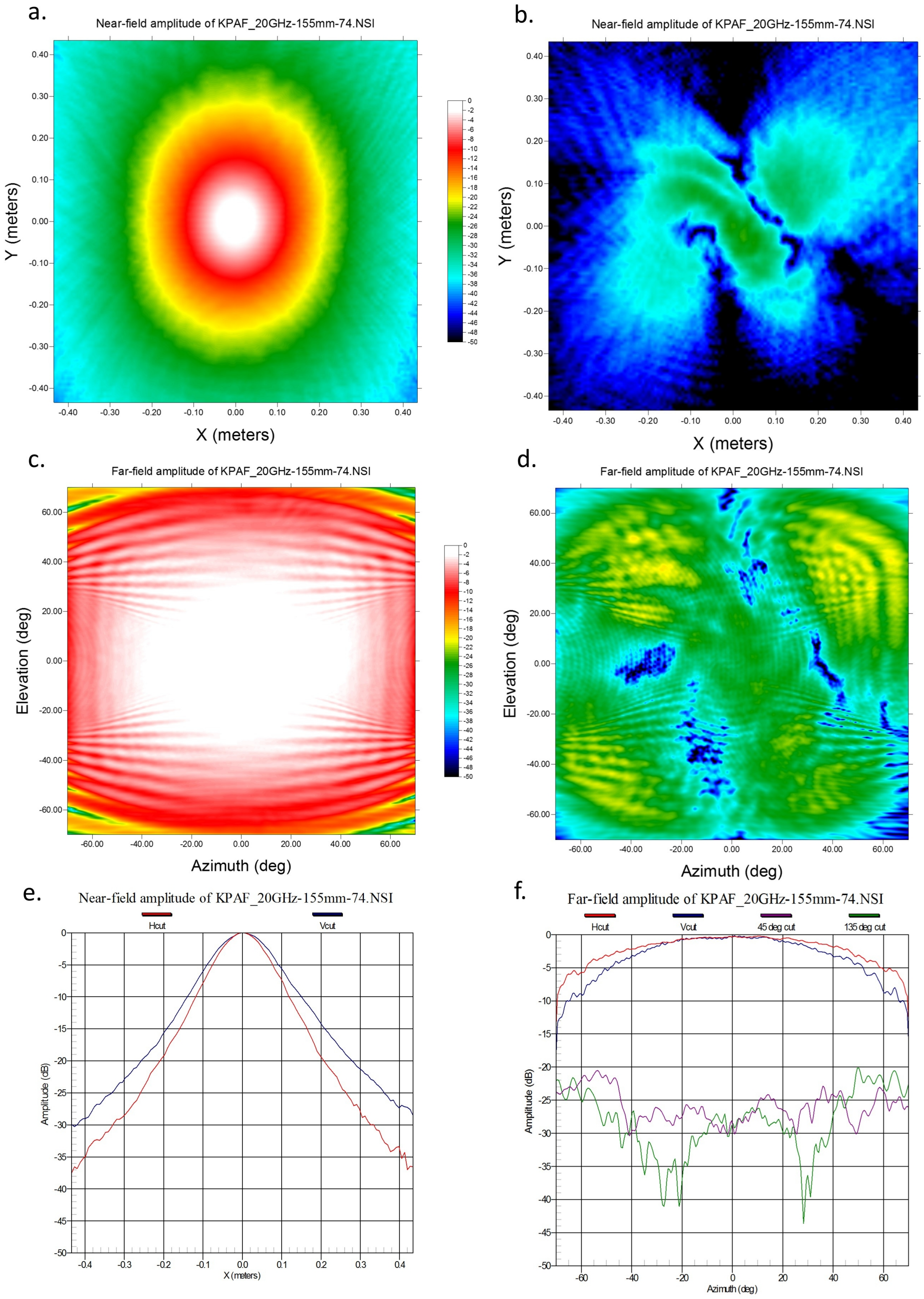

Figure 3.26: 20 GHz near-field: (a, b, e) and far-field: (c, d, f) radiation patterns from near-field scanning measurement, single KPAF antenna. Near-field 2D raster: (a) co-polarization and (b) cross-polarization. Far-field 2D raster: (c) co-polarization and (d) cross-polarization. E- and H-plane cuts: (e) near-field co-polarization and (f) far-field co- and cross-polarization. AUT-probe distance 155 mm.

- f. Far-field co- and cross-polar gain, E- and H-plane cuts from c., axes: azimuth (°), elevation (°)

The near-field co-polar gain patterns in Figure 3.25a and Figure 3.26a show the expected concentrated near-field radiation from the end of the antenna in the narrow beamwidth. The asymmetry in the principle E- and H-planes is evident even in the near-field measurements.

Figure 3.25b and Figure 3.26b confirm that the near-field cross-polarization is at most 25 dB below the peak co-polarized gain even along the worst 45° and 135° diagonals at X=Y and X=-Y respectively.

The far-field co-polar gain patterns in Figure 3.25c and Figure 3.26c show the expected beamwidths and relative asymmetry in the E- and H-planes, summarized in Table 3.3.

The cross-polarization gain patterns in Figure 3.25d and Figure 3.26d display a respectable 20 dB below the peak co-polarized gain.

Cut planes in Figure 3.25 and Figure 3.26 sections e (near) and f (far) depict the E- and H-planes. The ratio of E- to H-plane beamwidths is around 85% shown in Table 3.3 agreeing with simulations. The absolute 10 dB measurements are slightly larger than those obtained by far-field techniques, both summarized in Table 3.4. The near-field technique as expected yields values slightly in error to the far-field techniques due to the angular scanning limitation for antennas with low directivity.

Freq. (GHz)	E:10 dB	H:10 dB
18	123°	146°
20	132°	140°

Table 3.3: Near-field scanning measurement radiation 10 dB beamwidths for E- and H-plane cuts.

Far-Field Scanner Measurement

The anechoic chamber at the University of Victoria is used for far-field antenna testing, using an ORBIT/FR Legacy series Az/El positioner that can rotate the AUT through 360° in azimuth and 180° in elevation and is controlled remotely on a local workstation. A stationary transmitting antenna is a 25 dB K-band 18 - 26 GHz standard gain horn (SGH) from A-InfoMW, P/N LB-42-25-C-KF with a K-type coaxial connector and mounted on the AL-4906-3A controller/encoder.

The farfield of the largest antenna dimension the standard gain horn is $d = 10$ cm. Therefore, the farfield of the system will be $2d^2/\lambda = 1.74$ m $= d_{far}$. The distance between the standard gain horn and the AUT is set to 2 m to allow for a margin of error, and the expected free space loss at d_{far} at the highest frequency is:

$$\text{Loss} = (4\pi d_{far}/\lambda)^2 = 4.7\text{x}10^6 => 10\ \log(4.7\text{x}10^6) = 66.7\ \text{dB}. \tag{3.23}$$

Setting port 1 of the VNA to -7 dBm out, and with the gains and losses noted in Figure 3.27, the power at port 2 at 18, 26 GHz respectively will be:

$$\begin{aligned}\text{Power at Port 2} = {} & \text{Power at Port 1 - 72" cable loss + SGH - free space loss +} \\ & \text{KPAF gain - miniSMP cable loss - 60" cable loss} \\ & \text{+ AML amp gain - 72" cable loss} \\ = {} & \text{-12 dBm at 18 GHz, -34 dBm at 26 GHz}\end{aligned}$$

Even though the 10 - 20 GHz AML amplifer has a dramatic negative gain slope, it provides enough gain to keep a healthy signal to noise ratio (> 30 dB) at the high end of the band. Care was taken to ensure that the AML amplifier was not approaching the first order compression point, nor was the power into the VNA anywhere close to dangerous levels. A SOLT 2-port calibration removed the three Microcoax cables, the VNA effects and the amplifier as shown in Figure 3.27. Therefore the DUT is the SGH, the free space loss, the KPAF antenna and the Rosenberger mini-SMP cable.

Final results of the far-field scanner measurements of co-polar and cross-polar values in the E- and H-planes are shown in Figures 3.28 and 3.29.

Measured data is shown at least for azimuth angles 0° to +90° and when possible over the full azimuth circle, -180° to +180°. Simulated data for both CST and HFSS full-wave solvers are included. The peak co-polar gains before normalization at 18/20/22/26 GHz are 8.2/7.2/7.0/7.1 dB for the CST simulation and 8.5/7.6/6.9/7.5 dB for the HFSS simulation, the values are similar as expected. The agreement between measured and simulated data are very good for the co-polarized data and adequate for the cross-polarized data. The cross-polarized measurements would benefit from an RF setup with more signal to noise headroom by adding an amplifier, which was not available at the time.

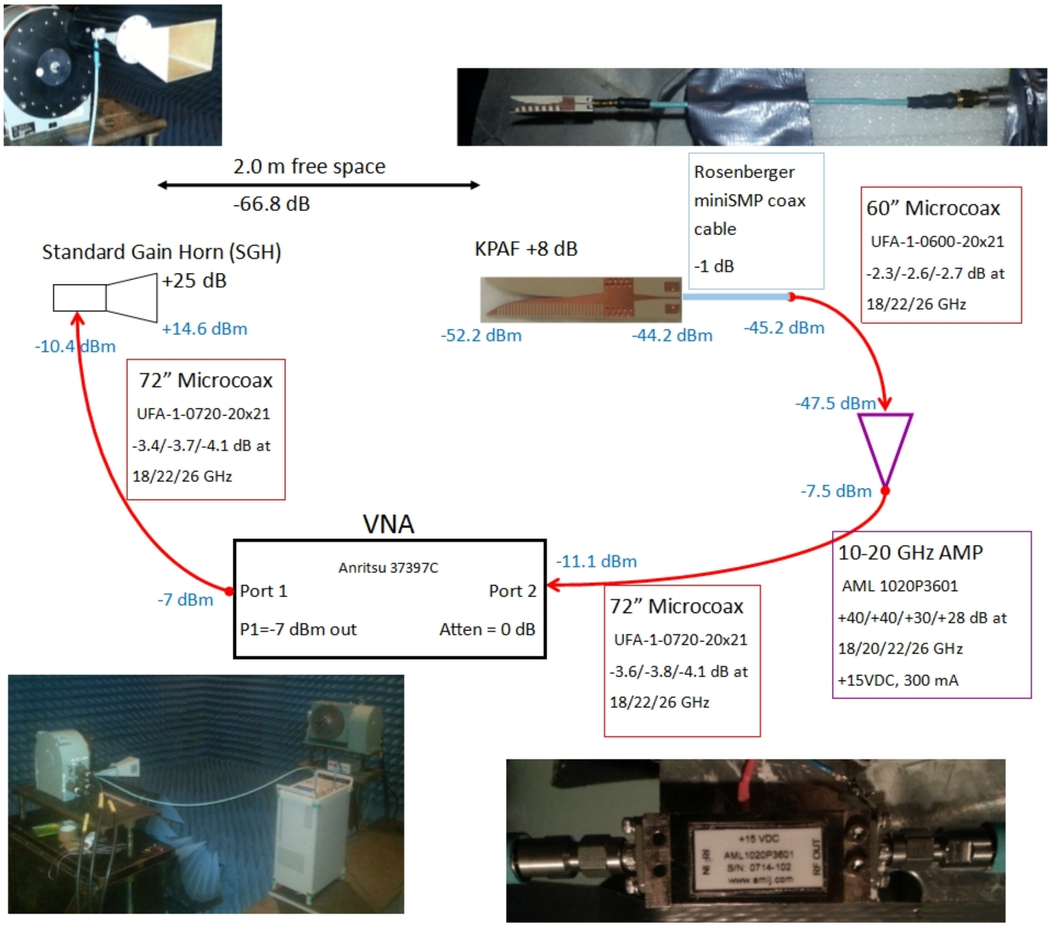

Figure 3.27: Far-field KPAF radiation pattern measurement setup, with absolute power levels marked in blue and relative gains and losses of the cables, amplifier, free space and antennas noted.

Simulated D-plane cross-polar values from HFSS and CST are shown in Figure 3.30 for azimuth angles -180° to +180°. Measured results in this plane were not taken due to time constraints, however the the E- and H-plane values are measured in Figures 3.28 and 3.29. The D-plane is usually the azimuthal location for the worst-case cross-polarization results, when compared with the simulated and measured E- and H-plane values show similar expected normalized values around -20 dB and slightly higher for 22 and 26 GHz, peaking at -10 dB.

Comparisons and Conclusions

A summary of the near- and far-field scanning measurement and simulation results follow. All values are relatively close except those marked in boldface in Table 3.4.

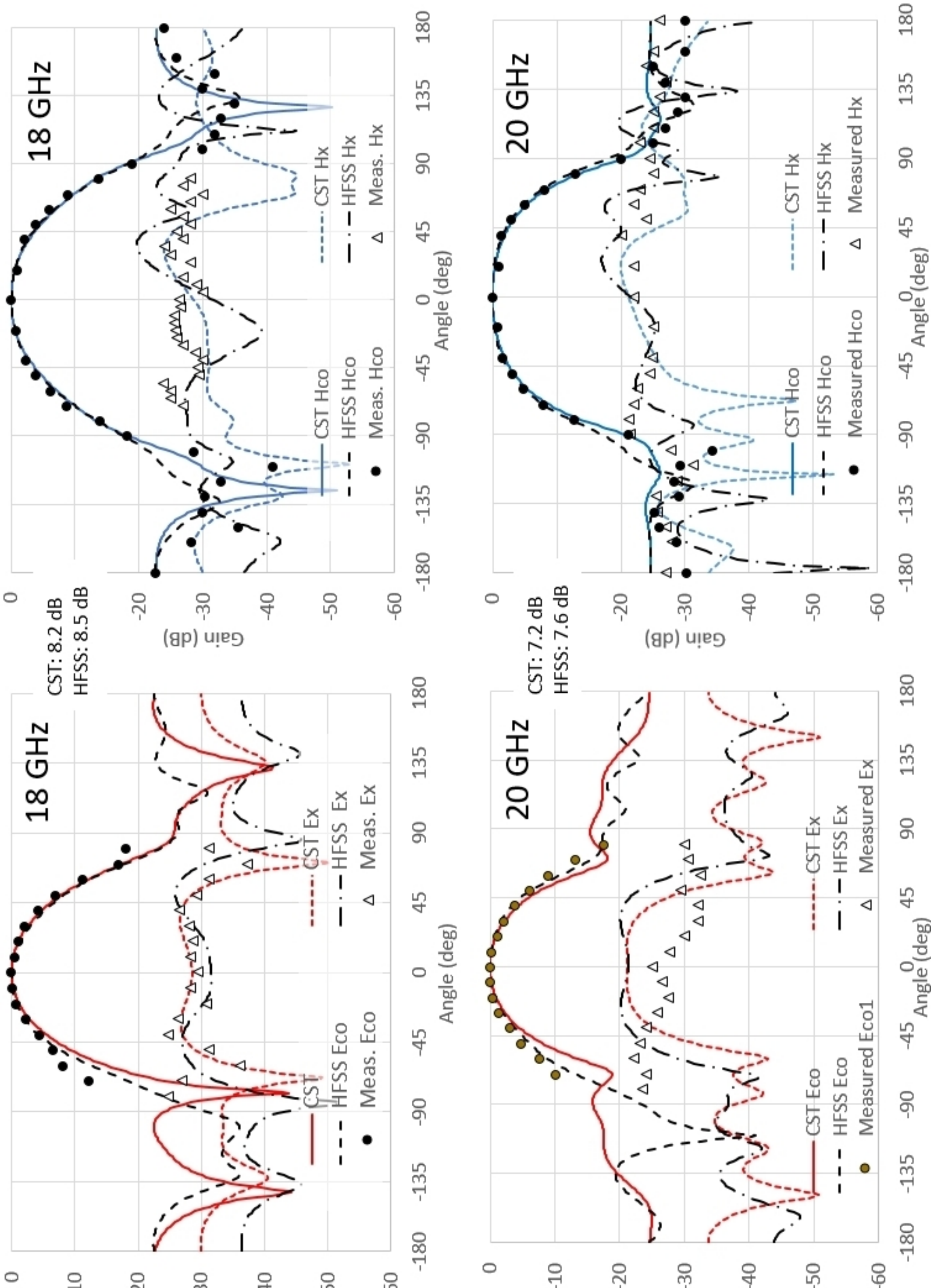

Figure 3.28: Far-field scanning measurement and simulated radiation patterns for E and H principle planes, co-polar (co) and cross-polar (x) at 18 and 20 GHz. Normalized gain (dB). Peak gains noted for each frequency and simulator.

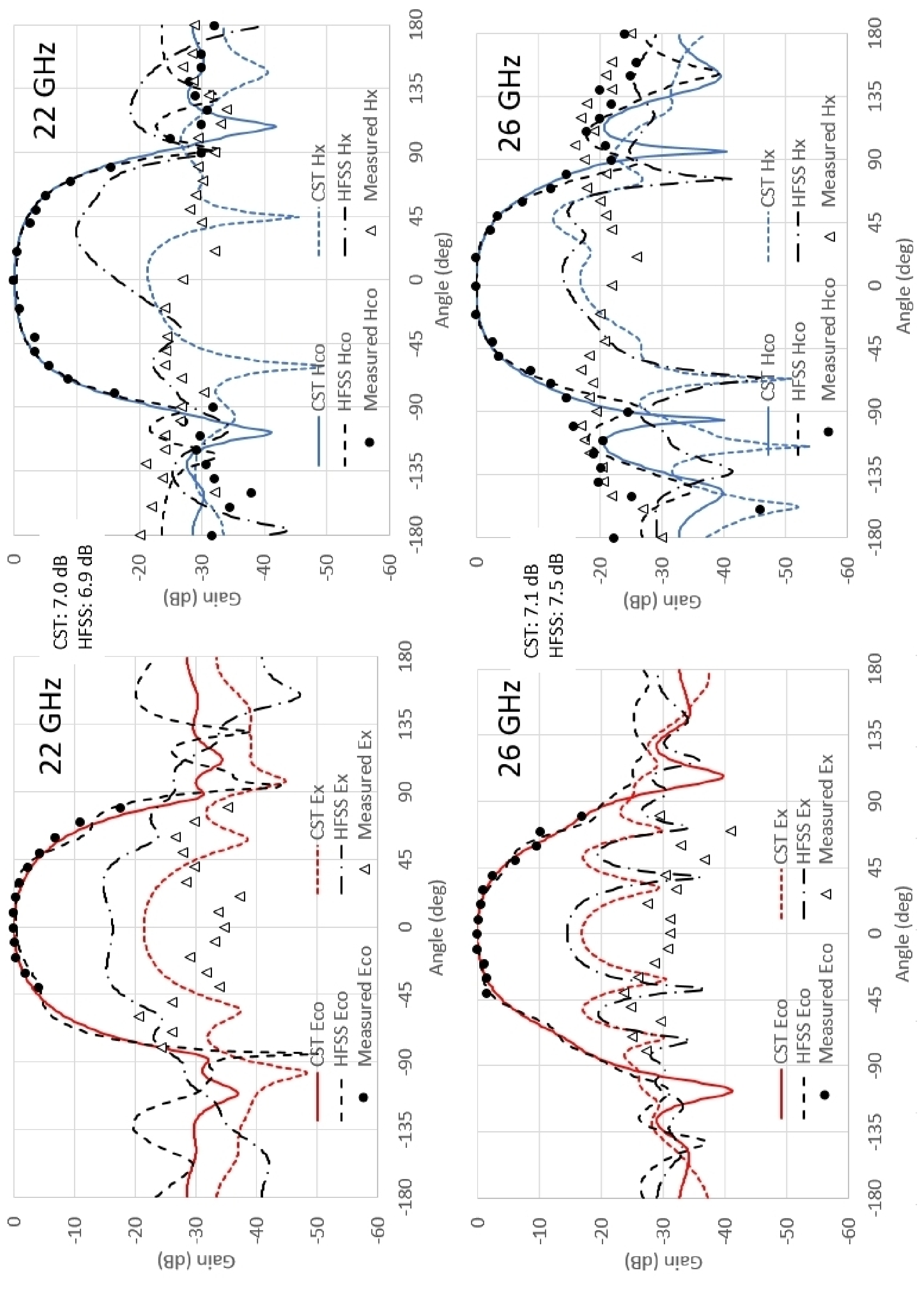

Figure 3.29: Far-field scanning measurement and simulated radiation patterns for E and H principle planes, co-polar (co) and cross-polar (x) at 22 and 26 GHz. Normalized gain (dB). Peak gains noted for each frequency and simulator.

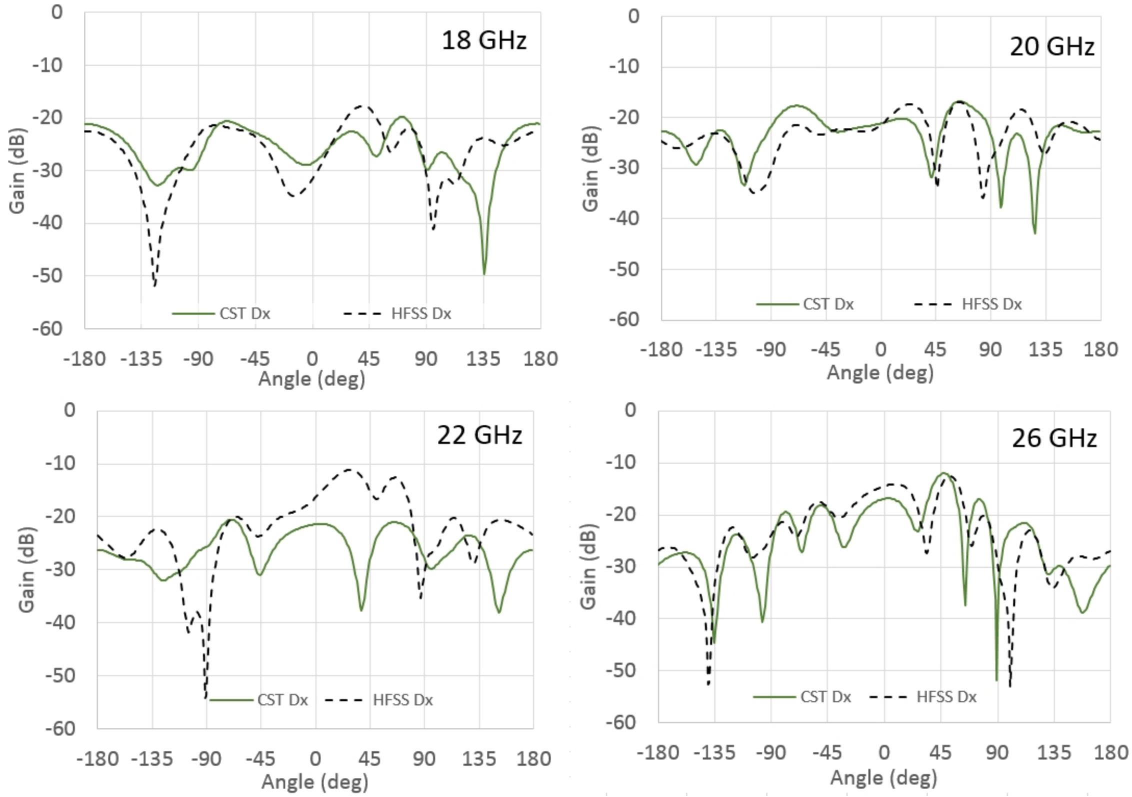

Figure 3.30: Far-field scanning simulated radiation patterns for D crosspol plane at 18, 20, 22 and 26 GHz. Normalized gain (dB) to values in Figures 3.28 and 3.29.

The near-field scanning method is not expected to yield very accurate results due to the limited scanning range in angle from boresight, yet the values are surprisingly close. A visual comparison of the D-plane simulated data at 18 and 20 GHz in Figure 3.30 and the near-field scanner measured data at 18 and 20 GHz in Figures 3.25e and 3.26e yield the same average values and lend credence to the near-field scanning measurement technique despite the KPAF's low directivity.

3.3.7 Estimated Antenna Noise Contribution from Efficiency

The insertion loss of a one-port device such as an antenna is difficult to measure in the lab but is necessary for estimating total system temperature. The loss can be estimated through the total antenna efficiency, e_0, which is a product of reflection efficiency, e_r due to impedance mismatch and radiation efficiency e_{cd} due to metal

Freq. (GHz)	CST E/H	HFSS E/H	NF E/H	FF E/H
18	107/140	110/140	**123**/146	110/145
20	112/150	112/152	**132**/140	**130**/150
22	120/146	120/147	-	130/144
26	120/138	120/147	-	120/130

Table 3.4: E-plane and H-plane (E/H) 10 dB beamwidths (degrees) for single KPAF antenna. CST and HFSS simulations and near-field scanning (NF) and far-field scanning (FF) measurements. Data farthest from average are marked in bold.

conduction loss and dielectric loss of the substrate of filling material.

$$e_0 = e_r \cdot e_{cd} \tag{3.24}$$

Γ is the impedance reflection coefficient of a transmission line with characteristic impedance Z_0 that feeds an antenna of input impedance Z_{in} as shown in Figure 3.31.

$$e_r = (1 - |\Gamma|^2) \tag{3.25}$$

$$\Gamma = \frac{Z_{in} - Z_0}{Z_{in} + Z_0} \tag{3.26}$$

P_{in} is the total power input to the antenna and P_{rad} is the total radiated power assuming a transmitting mode. For a lossless antenna $P_{in} = P_{rad}$. The radiation efficiency is also called the conduction and dielectric efficiency and can be defined as the ratio of the antenna gain G to directivity D.

$$e_{cd} = \frac{P_{rad}}{P_{in}} = \frac{G}{D} \tag{3.27}$$

Figure 3.32 displays the simulated total efficiency e_0 calculated by CST Microwave Studio for 18/20/22/26 GHz to be 0.90/0.86/0.93/0.92 respectively. The equivalent noise temperature T_{loss} can be estimated [15] from Equation 3.28 at the physical temperatures $T_p = 16$ K and 300 K of the antenna. For a room temperature antenna $T_p = 300$ K, the equivalent noise temperatures at the previously mentioned frequencies are 34.3/47.0/23.9/26.2 K, but at the cryogenic temperature $T_p = 16$ K the noise drops to 1.83/2.51/1.28/1.40 K. This dramatic reduction in noise temperature of the antenna decreases the total system temperature and is the primary reason for

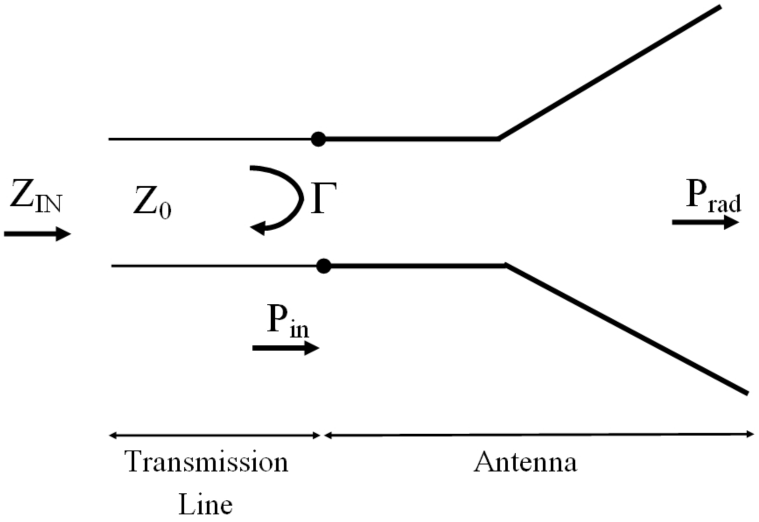

Figure 3.31: Transmission line and antenna model for efficiency calculations.

cryogenic cooling any receiver system.

$$T_{loss} = \left(\frac{1}{e_0} - 1\right) T_p \tag{3.28}$$

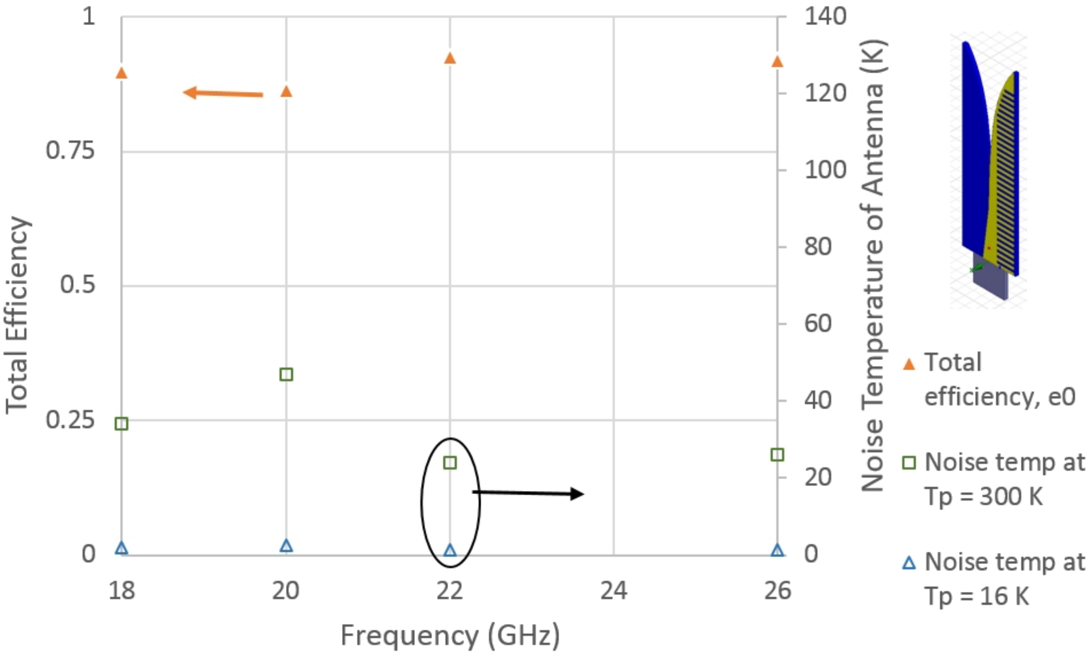

Figure 3.32: Simulated KPAF antenna total efficiency e_0 and equivalent noise temperature T_{loss} (K) for physical temperatures $T_p = 300$ K and 16 K.

Chapter 4

Antenna Array

The sky calls to us.
- Carl Sagan

An array is defined by its individual element radiation characteristics, the relative spacing between elements, and the geometrical layout including maximum extent.

4.1 Geometrical Parameters

A planar array with antenna centres on a rectangular xy-grid is used. The y coordinate is aligned along each 1 x 5 antenna "blade" module and the x coordinate is aligned between each blade, as demonstrated in Figure 4.1. In this section the element spacing d_x and d_y is determined followed by two estimates for maximum array size or extent.

4.1.1 Element Spacing

Classically for coherent antenna arrays not coupled to a reflector, the maximum element spacing is set to 0.5λ in order to avoid grating lobes [46]. However, when the antenna array is coupled with a parabolic reflector for added gain and increased resolution, the shape of the reflector defined by the ratio of the focal length to the diameter, F/D, must also be taken into account. For an axially symmetric parabolic reflector with F/D = 0.45, the half-angle, θ_m is:

$$\theta_m = 2 \arctan \left[\frac{1}{4(F/D)} \right] = 58.1^\circ \tag{4.1}$$

The maximum element spacing for a rectangular array in the substrate plane, d_y is [65]:

$$\begin{aligned} d_y = \frac{\lambda}{(1+\sin\theta_m)} &= 0.54\lambda = 9.00 \text{ mm @ 18 GHz} && \text{(4.2a)} \\ &= 6.21 \text{ mm @ 26 GHz} && \text{(4.2b)} \end{aligned}$$

The element spacing d_y is set to 6.20 mm to ensure grating lobe-free operation at 18 - 26 GHz. For similar reasons, the element spacing perpendicular to the plane of the substrate is $d_x = d_y$. In terms of the variables used in Figure 3.18 for the single antenna element geometry, $d_y = W_{sub}$.

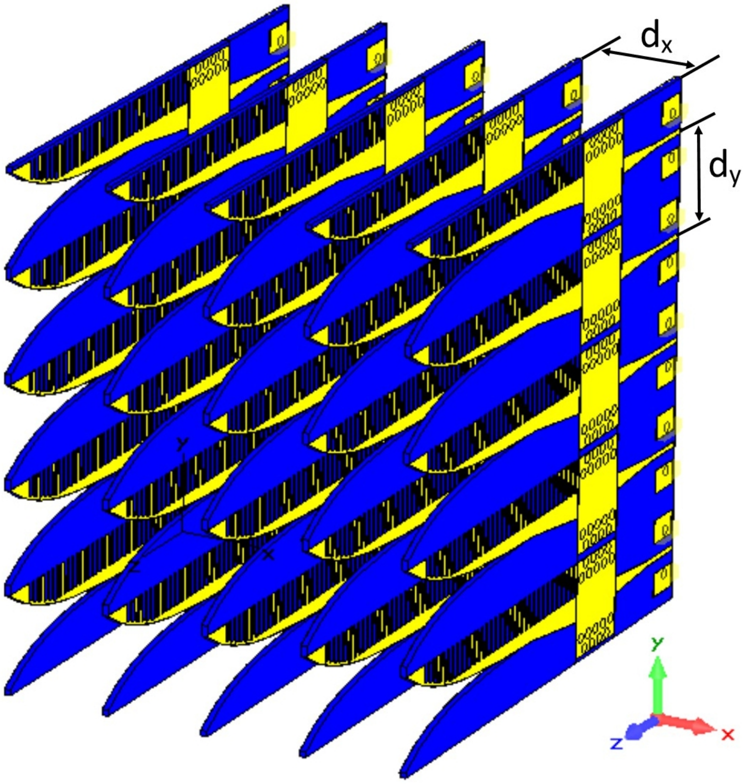

Figure 4.1: KPAF array element spacing definitions and coordinate system.

4.1.2 Maximum Extent

The maximum array size is estimated via two approaches, Minnett and Thomas' maximum extent calculations and Hayman's encircled power theory.

1. Minnett and Thomas' 1968 classical work [66] describes fields scattered by circularly symmetric paraboloidal reflectors illuminated by a linearly polarized wave incident on the aperture. As expected, these fields have inherent symmetry about the paraboloid's axis of revolution $\hat{z}$. The maximum acceptable paraxial distance (from the axis of revolution) is determined by the degree of defocus of the electric and magnetic fields, setting an upper bound for the array radius.

   The geometry is defined in Figure 4.2. The direction of propagation is along $\hat{z}$, the reflector is centered at V, the focal plane at P and the far-field at the coordinate origin O. The array is oriented in the $x-y$ plane so that P is the centre of the array and Q is the farthest point on the array from centre. The maximum radius of the array is set by $\overline{\mathrm{PQ}} = \rho$, a function of r_0. The angle ψ between the centre of the array and a point M on the parabolic reflector reaches a maximum ψ_{max} at the edge of the reflector. For a parabola with F/D = 0.45, D = 10 m, $\psi_{max} = \theta_m = 58.1°$. The maximum array radius ρ in the focal plane is a function of r_{0max}:

   $$r_{0max} = \frac{2F}{1+\cos\psi_{max}} = \frac{2(4.5 \text{ m})}{1+\cos(58.1°)} = 5.88 \text{ m} \tag{4.3}$$

   $$\rho \leq 0.35\sqrt{r_{0max}\lambda} = 91 \text{ mm} \tag{4.4}$$

   The largest square array circumscribed in a circle with radius $\rho = 91$ mm is $\rho\sqrt{2} \times \rho\sqrt{2} = 129$ mm x 129 mm. This corresponds to 11.2 x 11.2 elements at 26 GHz and 7.7 x 7.7 elements at 18 GHz.

2. The encircled power method explained by Hayman [22] can be used to estimate focal plane array radius ρ as a function of F/D and reflector diameter D. A plane wave illuminates an axially symmetric paraboloid reflector with axis of symmetry $\hat{z}$, and the focal plane disk is normal to $\hat{z}$. The Poynting vector, **S** is the power flow in an electromagnetic field composed of electric field **E** and magnetic field **H**.

   $$\mathbf{S} = \frac{1}{2}\,\mathbf{E} \times \mathbf{H}^* \tag{4.5}$$

   Summing S_z, the component of the Poynting vector in the $\hat{z}$ direction, over the

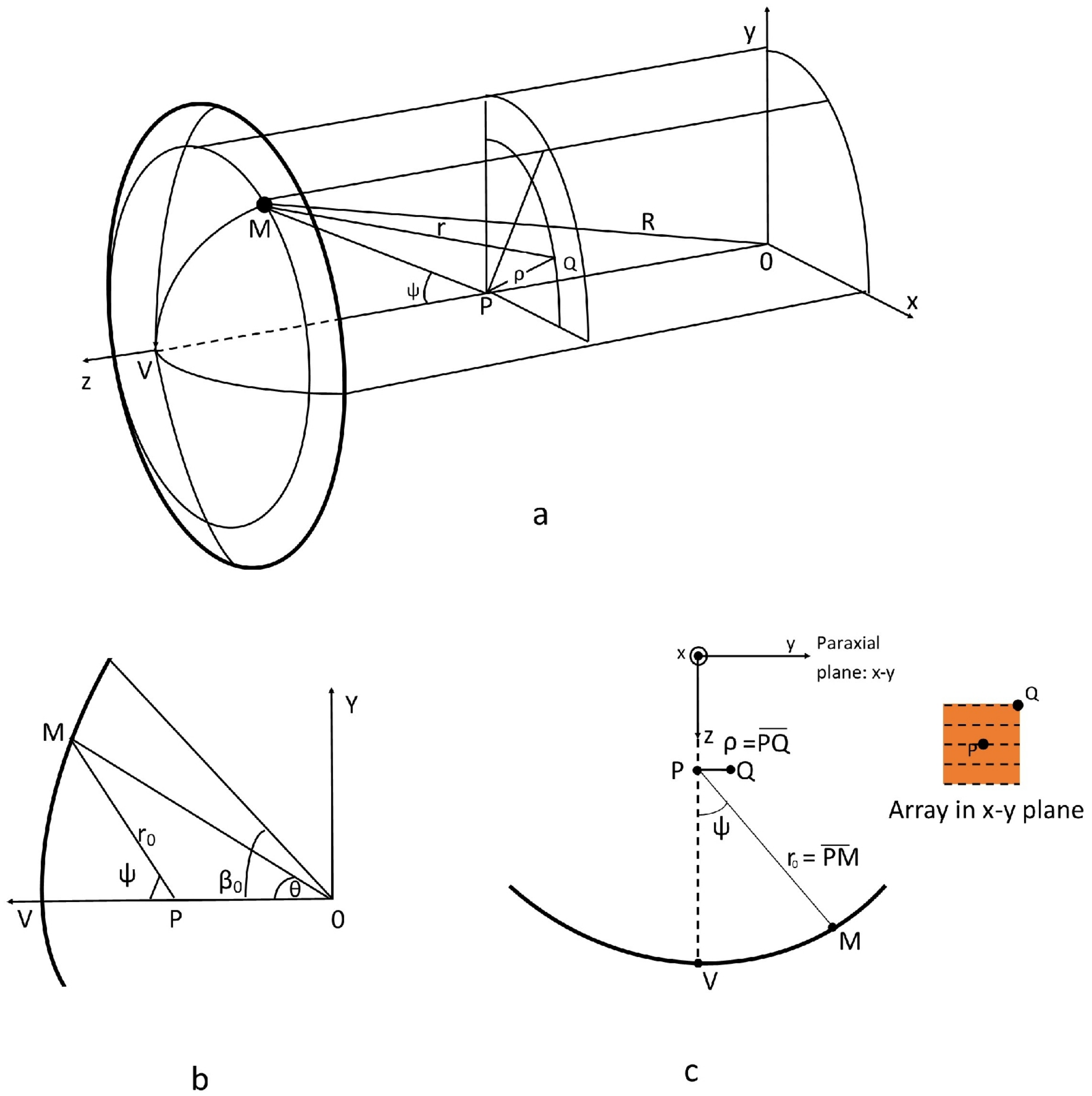

Figure 4.2: Paraboloidal geometry and definitions for array maximum extent calculations. a: Cartesian co-ordinate system of reflector centered at V, the focal plane at P with maximum radius Q and far-field centered at orgin O, b: Incidence plane including reflector and r_0, c: Paraxial x-y plane with array center P and maximum radial extent Q.

focal plane disk results in the the power, P:

$$P = \mathrm{Re} \oint_{disk} S_z ds \tag{4.6}$$

P is calculated for disks of radii corresponding to -1 dB and -3 dB (79% and

50%). The closed form Equation 3.41 in [22] calculates the radius for a circular array at 79% encircled power, reflector diameter D = 10 m and $\lambda = 11.5$ mm to be $\rho = 75$ mm.

The largest square array circumscribed in a circle with radius $\rho = 75$ mm is $\rho\sqrt{2} \times \rho\sqrt{2} = 106$ mm x 106 mm. This corresponds to 9.2 x 9.2 elements at 26 GHz and 6.3 x 6.3 elements at 18 GHz.

A 5 x 5 K-band array is proposed at element spacing 6.2 mm x 6.2 mm for an overall size of 31 mm x 31 mm with the future possibility of using this building block to form a 10 x 10 array, a maximum size of 62 mm x 62 mm. This is well within the most conservative array size estimate set forth by the encircled power method of 106 mm x 106 mm. Economically, arrays larger than 10 x 10 would be prohibitive due to the high price of receiver elements in addition to the added mechanical complexity and amplifier thermal heat load.

4.2 Definitions

The far-field results, both S-parameters and radiation patterns, employ the following phrases defined here:

Gain: $\frac{4\pi U}{P}$: where U is the antenna's radiation intensity in a given direction, P is the total power accepted by the antenna.

Element: gain pattern due to a single antenna element.

Composite: gain pattern of complex sum of all antenna elements. Amplitude and phase weights are applied to each element, although for this chapter, each element is weighted equally in amplitude and phase. Section 5.5 will explore other element weighting configurations.

Co-polar: linear E-field component in y-direction for KPAF antenna, e.g. along aperture width, using Ludwig's third definition of cross-polarization [67].

Cross-polar: linear E-field component in x-direction for KPAF antenna, e.g. perpendicular to aperture width, also using Ludwig's third definition of cross-polarization.

Primary beam patterns: far-field radiation patterns of the feed elements only, not including coupling to the reflector.

Secondary beam patterns: far-field radiation patterns of the feed-reflector combination.

4.3 Gaussian Array

To verify the estimated element spacing and maximum extent, a 5 x 5 and an extended 15 x 15 array of simple horn feeds at the prime focus of a F/D = 0.45, 10 m diameter paraboloidal reflector are simulated, first at the recommended pitch 6.2 mm and next at a 100 % increased pitch, 12.4 mm. The far-field gain difference between centre and corner elements are compared, the cross-over gain levels of neighbouring elements are calculated and the pattern distortion of the outermost elements are qualitatively evaluated.

The antenna software GRASP[1] v.10.1. employs physical optics (PO) and physical theory of diffraction (PTD) techniques to calculate near- and far-field complex radiation patterns of reflector-antenna combinations [68]. One of the software's default feed types is an ideal Gaussian, a function of only the frequency, the reflector half-angle θ_m and taper value at that half-angle. While using this object for the feed array does not incorporate mutual coupling between feeds, it is a logical step for validating element separation and maximum extent. Figure 4.3 shows the reflector and array configuration in GRASP. The Gaussian feed parameters are 22 GHz, $\theta = 58.1^\circ$ and an edge taper of 3 dB, the taper is chosen to ensure maximum illumination of the reflector at the expense of decreased efficiency due to excess spillover noise.

4.3.1 6.2 mm element separation: 5 x 5 and 15 x 15

For a 5 x 5 array with Gaussian element spacing $d_x = d_y = 6.2$ mm at the prime focus of a reflector, the individual element secondary gain patterns are superimposed in Figure 4.4. The far-field contours are spaced by 3 dB; the red/blue contours are -3 dB/-6 dB, respectively, down from the corner element maximum. As expected the centre nine elements have the most gain as they are closest to the reflector's focus point. The contours show an element to element overlap of approximately 3 dB, a more accurate crossover level can be seen in the cut plane in Figure 4.5.

---

[1] GRASP is a registered trademark of TICRA, Denmark.

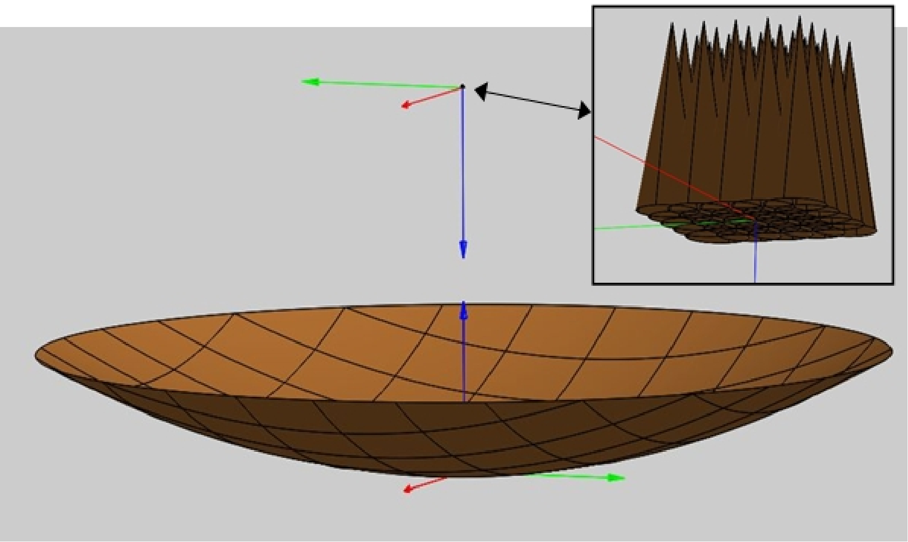

Figure 4.3: Paraboloidal reflector with focal length F = 4.5 m with 5 x 5 array at prime focus configuration in GRASP.

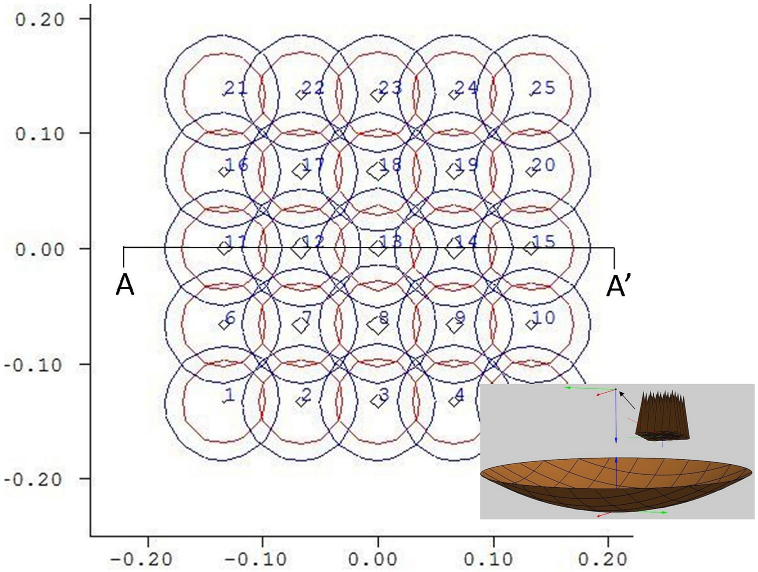

Figure 4.4: Co-polar element gain (dB) of 5 x 5 Gaussian feed array at 6.2 mm pitch in x and y, 22 GHz. 3 dB (red) and 6 dB (blue) gain contours of each individual element, normalized to corner element gain value. The cross-sectional plane A-A’ is displayed in Figure 4.5. Inset: 0.45 F/D paraboloid with 5 x 5 on-axis feed array. x-axis: azimuth (°), y-axis: elevation (°).

Figure 4.5 shows the cross-section at A-A’ in Figure 4.4 of the co-polar element gain. The maximum gain drop relative to the centre element at the edge of the 5 x 5 array is only 0.2 dB and at the edge of the 15 x 15 array, a respectable -1.5 dB.

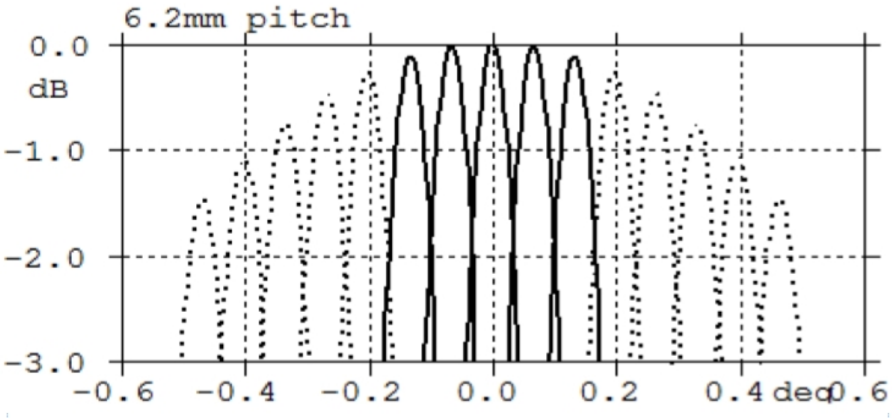

Figure 4.5: Co-polar element gain (dB) vs azimuth (°) of 5 x 5 (solid line) array along cut plane A-A' of Figure 4.4 and 15 x 15 (dotted line) array. The -2.0 dB cross-over level between Gaussian element beams validates the 6.2 mm element spacing value. These 22 GHz simulated secondary radiation patterns incorporate the reflector and are normalized to the centre beam maximum.

The overlap between element gains is -2.0 dB for the 5 x 5 array and -2.8 dB at the edge of the 15 x 15 array. This is an acceptable gain differential between centre and outer elements; the cross-over levels between elements all validate both the 6.2 mm element spacing and the 5 x 5 and 15 x 15 array extent values.

4.3.2 12.4 mm element separation: 5 x 5 and 15 x 15

To ensure the narrow element pitch of 6.2 mm is required, the spacing is doubled to 12.4 mm and the same simulations performed on both a 5 x 5 and 15 x 15 array of Gaussian feed elements. The cut plane through the centre row for both 5 x 5 and an extended 15 x 15 array in Figure 4.6 shows each element's gain. The large 12.4 mm element separation results in a cross-over level worse than -6 dB between elements. Although the maximum gain drop relative to the centre pixel at the edge of the 5 x 5 array is only -0.6 dB and at the edge of the 15 x 15 array is -5.8 dB, the 12.4 mm spacing is not recommended due to the low-gain results and sparse field of view.

GRASP simulations of Gaussian feeds do not take into account mutual coupling between antenna elements which is likely to be significant with closely spaced planar antennas. This must be done for the antenna array on a full-wave 3D solver, and the far-field patterns imported to GRASP. The secondary far-field patterns resulting from the reflector-antenna combination are calculated in the next section.

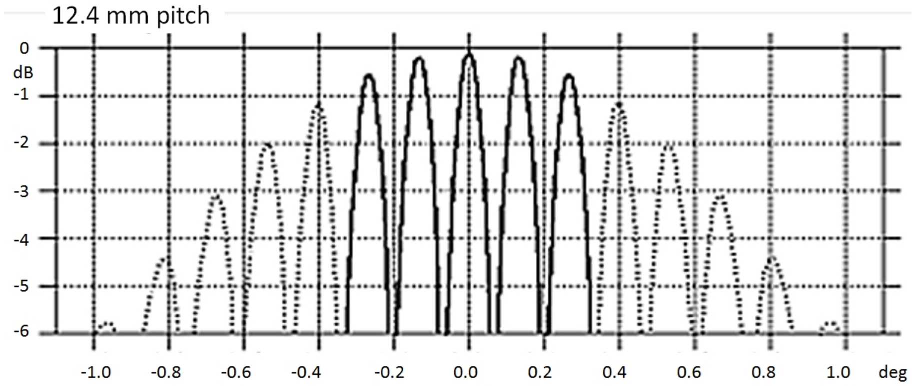

Figure 4.6: Co-polar composite and element gain (dB) of 5 x 5 Gaussian feed array at 12.4 mm pitch in x and y, 22 GHz. Element gain (dB) along cut plane through array centre of 5 x 5 (solid line) and 15 x 15 (dotted line) normalized to centre element. x-axis: azimuth (°).

4.4 KPAF Array

The fabricated and connectorized 1 x 5 blade array is detailed in Figure 4.7 including (a) the top side, (b) the bottom grounded side, (c) the custom made extraction tool to detach miniSMP connectors from coaxial cable, (d) the precision mounting bracket for VNA measurement setup, and (e) the coaxial cables and 50Ω terminations for unused ports during testing.

4.4.1 1 x 5 Radiation Patterns

Like the single KPAF element, the far-field radiation patterns of the 1 x 5 array are measured with far-field scanner setup. E- and H-plane co-polar gain patterns and simulated D-plane cross-polarized gain at 22 GHz are shown in Figure 4.8 showing very good agreement between simulated (solid lines) and measured (dots) maximum gain at boresight $\theta = 0$ and for beamwidth values. The array gains and beamwidths are summarized in Table 4.1 for each of five array elements and also compared to the single KPAF antenna measurements from Figures 3.28 and 3.29.

Referencing Table 4.1, a summary and comparison of the 1 x 5 array and single antenna measurements are as follows.

Absolute gain: The single KPAF antenna yields 7.0 dBi gain and the average array antenna yields 5.7 dBi. Since the calibration and measurement setup for the single and array antennas are identical, the losses must be due to the array con-

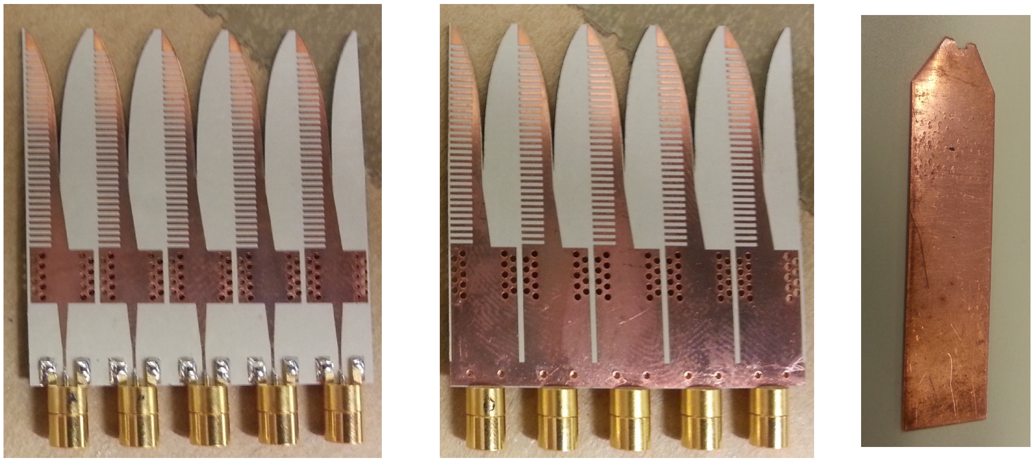

(a) Top (b) Bottom (c) Tool

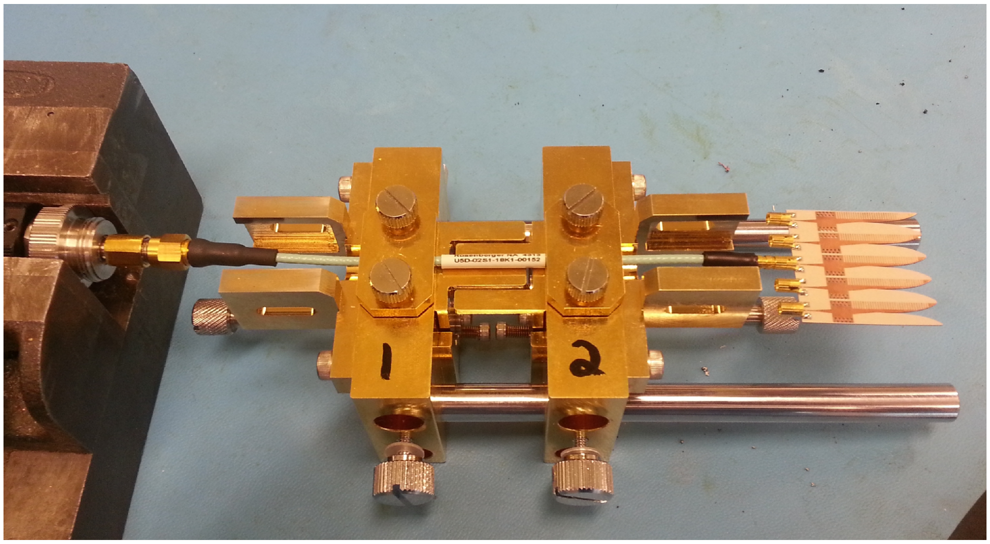

(d) VNA measurement setup

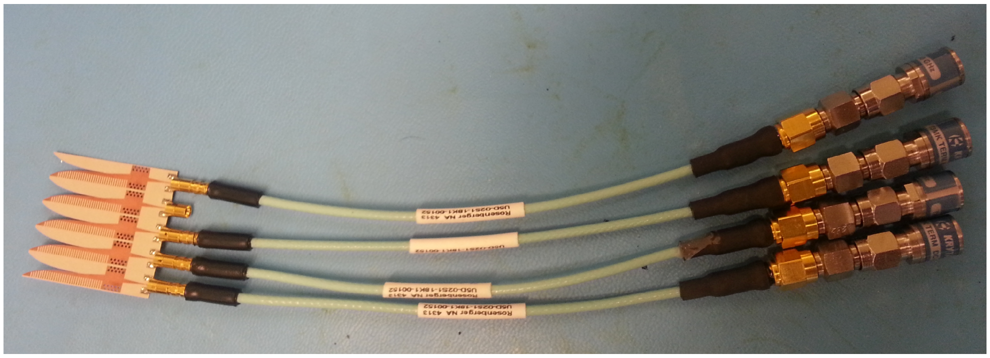

(e) Terminated unused ports

Figure 4.7: KPAF 1 x 5 antenna blade (a) top and (b) bottom. (c) Custom made mini-SMP extraction tool. (d) VNA S-parameter measurement setup. (e) Open ports terminated with coaxial cable and 50Ω commerical loads.

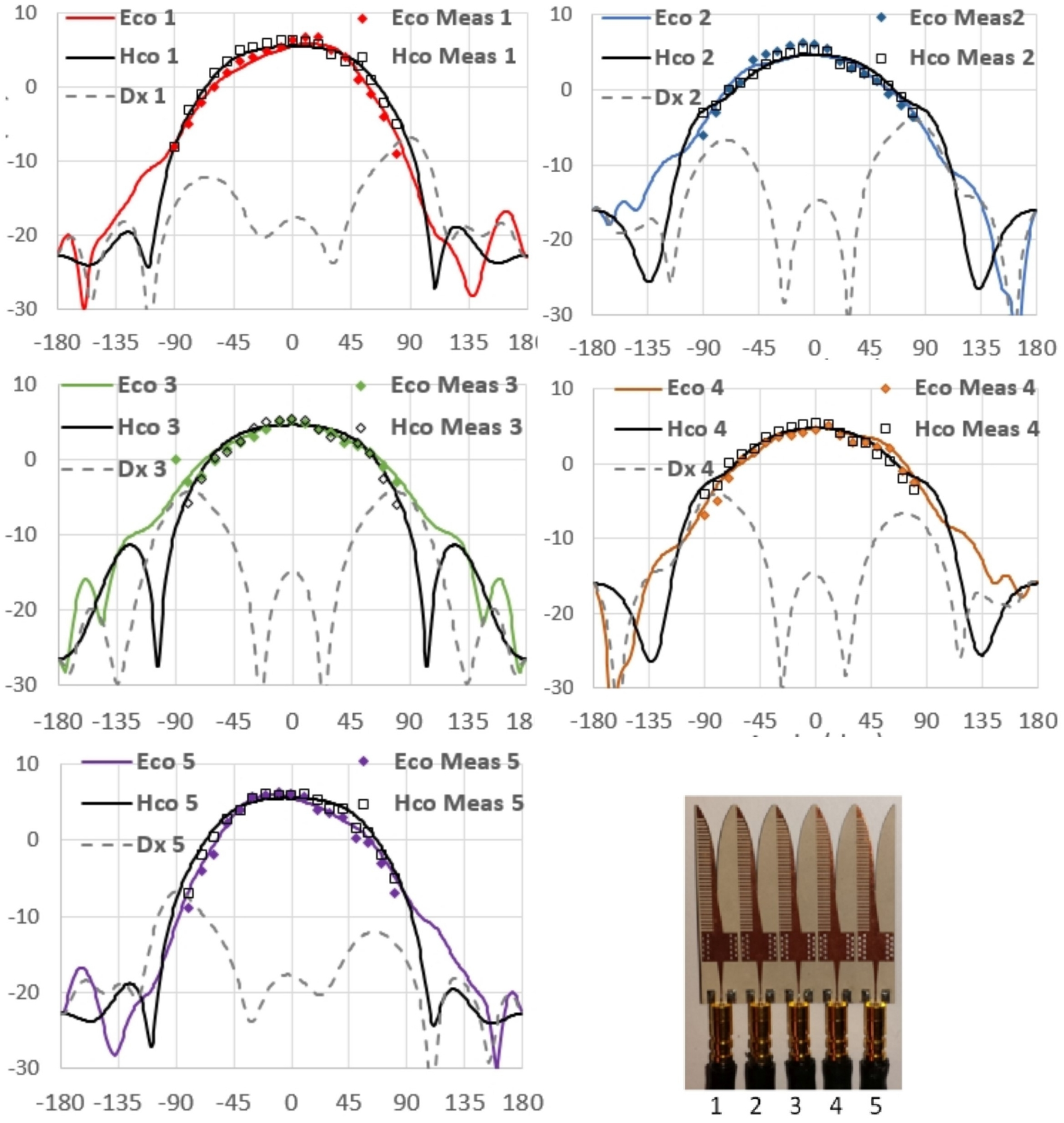

Figure 4.8: Simulated and measured co-polar (Co) and cross-polar (X) gain (dBi) patterns vs $\theta(°)$ for 1 x 5 KPAF array, with far-field scanner at 22 GHz. E-plane ($\phi = 90°$), H-plane ($\phi = 0°$), D-plane ($\phi = 45°$). Array port definitions as shown.

figuration; the radiation efficiencies are lower due to increased input reflections which will be demonstrated in Section 4.4.2. The antenna input reflection is optimized for 50 Ω as the cryogenic amplifier chip has been designed for optimum noise and then transformed to 50 Ω input and output impedance. An extensive redesign could improve the S_{11} and the gain. As for all travelling wave antennas, gain performance could also be increased by adding more length. However

	Gain (dBi)	**E-plane (°)**	**H-plane(°)**	**E/H ratio**
Single element	7.0	120	146	0.82
Array element 1	6.5	148	164	0.90
Array element 2	5.7	178	200	0.89
Array element 3	5.3	186	164	1.13
Array element 4	4.9	186	202	0.98
Array element 5	5.9	158	162	0.96
Array average	5.7	171	178	

Table 4.1: Measured KPAF single element and 1 x 5 array elements with far field scanner. Gain, E- and H-plane 10 dB beam widths, and the E- to H-plane beam width ratio.

the 1.3 dB reduction in absolute gain should not pose a problem in subsequent beamforming stages.

Relative gain: Array element gains vary from 4.9 dBi to 6.5 dBi. These relative differences are not problematic since elements with relatively high cross-over levels, when summed in the beamformer, tend to even out most variations. This is shown for the 18 GHz 5 x 5 KPAF element contour results in Figure 4.14a which vary in peak gain across the elements from 59.8 to 58.1 dBi.

Beam widths: The 10 dB array element beam widths are larger than the single antenna, on average 30% (51°) and 18% (18°) for E- and H-planes, respectively. Also, the ratio of E- to H-plane beam widths increases from 0.82 for the single element to 0.89 to 1.13 for the array elements. Since the test setup for element and array measurements are identical, the mutual coupling between array elements must be responsible for the larger beam widths and higher E- to H-plane ratios.

4.4.2 1 x 5 S-Parameters

Full S-parameters for the 1 x 5 array characterize the input reflection, S_{nn}, and degree of mutual coupling between ports, S_{nm}. They are measured with the VNA with SSST calibration to move the reference plane up to the intersection between the SIW and antenna, exactly the same procedure as with the single KPAF antenna in Section 3.3.5. The results are shown in Figure 4.9, along with the port numbers.

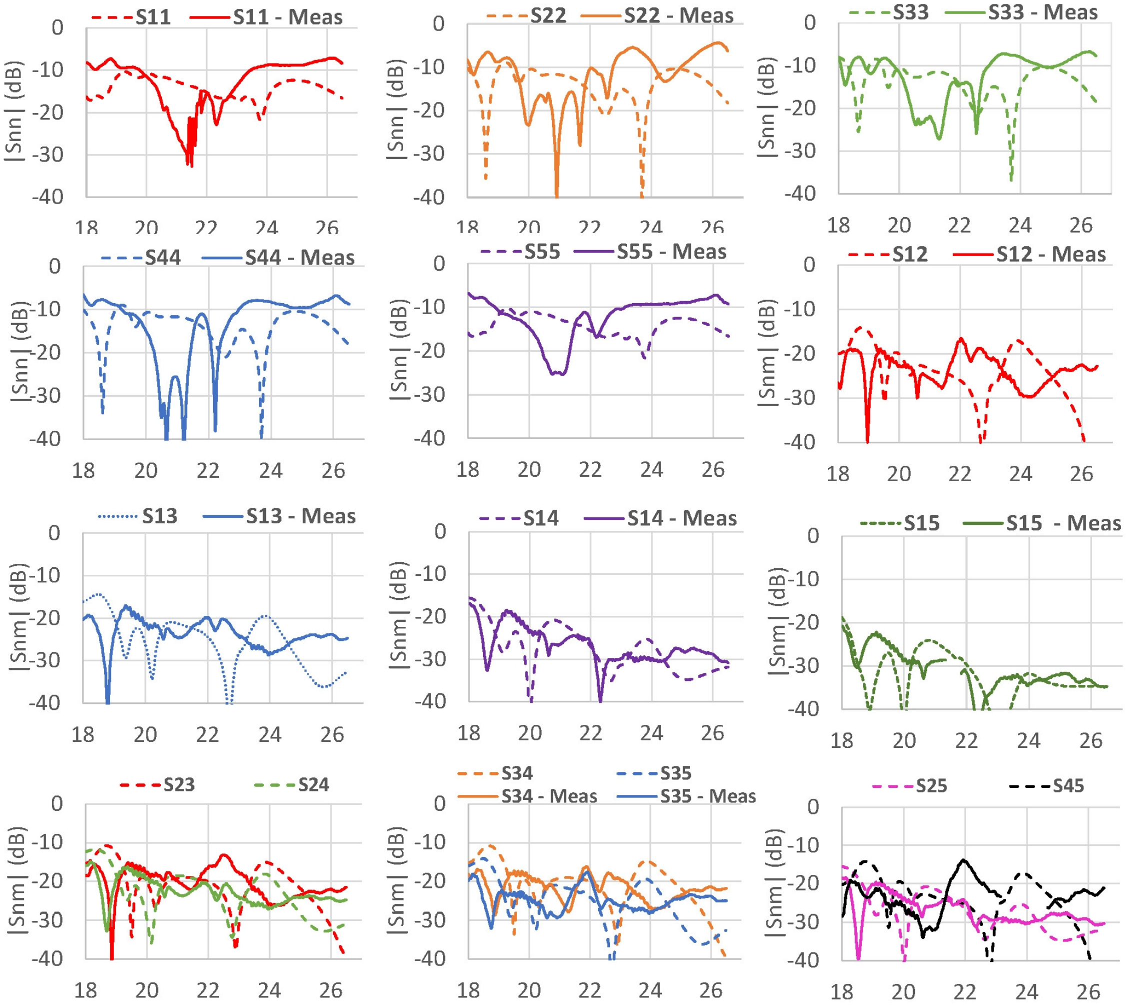

Figure 4.9: KPAF 1 x 5 array embedded single element S-parameter measured and simulated results including input reflection, S_{nn}, and mutual coupling, S_{nm}. Unused ports are terminated in 50Ω coaxial loads. x-axis: frequency (GHz), y-axis: 20 log|S| (dB). Simulated (dashed lines) and measured (solid lines). Array port definitions are shown in Figure 4.8

There is good agreement between simulated and measured average values for the mutual coupling data and input reflection values. Although there are differences in both the input reflection data and mutual coupling as per locations of resonances, the mean levels are maintained. Comparing the input reflection of the antenna elements with that of the single KPAF antenna in Figure 3.23a, the measured result trends from -10 dB at 18 GHz to a minimum near 20-23 GHz and then back up to -10 dB at 26 GHz. This general shape is echoed in the array data.

The array and single KPAF input reflection measurements are perhaps the most strict tests for evaluating the quality of the VNA SSST calibration over the full frequency range. The limitations of the SSST calibration are best seen here, as in theory all circuitry up to the antenna - SIW boundary should be removed. However, the common sections of the three standard shorts proved not perfectly the same, leading to different resonance sections in input reflection, although good average levels.

4.4.3 5 x 5 Mechanical

Stacking five 1 x 5 antenna arrays creates the 5 x 5 array in Figure 4.10. Mechanically, the aluminum mounting allows the coaxial cables to be pulled through the plate. Each miniSMP connector is pressed into and locked with its mating 1 x 5 blade connector. With the five cables attached to the blade, the connector line is lowered into the aluminum mount; when aligned, the cable connector notch slides back into the aluminum mount slot edge. Having the five cable end connectors in place, the aluminum retainer is inserted into the five openings and fastened to the mount with cap screws holding the cable end connectors and blade in place. The manufactured 5 x 5 array is in the construction phase waiting on fabrication of the aluminum mechanical mount.

4.4.4 5 x 5 Radiation Patterns

From Section 4.1.1 the adequate spacing between elements for both x- and y-directions is 6.2 mm, resulting in a -2 dB gain cross-over between Gaussian far-field element beams. The Gaussian feed element is now replaced with the KPAF antenna element design from Section 3.3. Since GRASP alone is unable to model mutual coupling between the feeds, modelling the array and solving all elements concurrently with a full-wave electromagnetic simulator allows for such coupling to be included.

Using CST Microwave Studio, the primary radiation patterns are created for each element embedded within the array structure and incorporating the simultaneous mutual electromagnetic interactions. The proximity effects of all other elements are included by performing this step. Generating the primary radiation characteristics in CST first provides a more realistic estimate of the actual array performance at the expense of simulation complexity.

Each element's far-field primary gain pattern, both linear co-polarization and cross-polarization, are then exported to GRASP format via a CST macro "Farfield

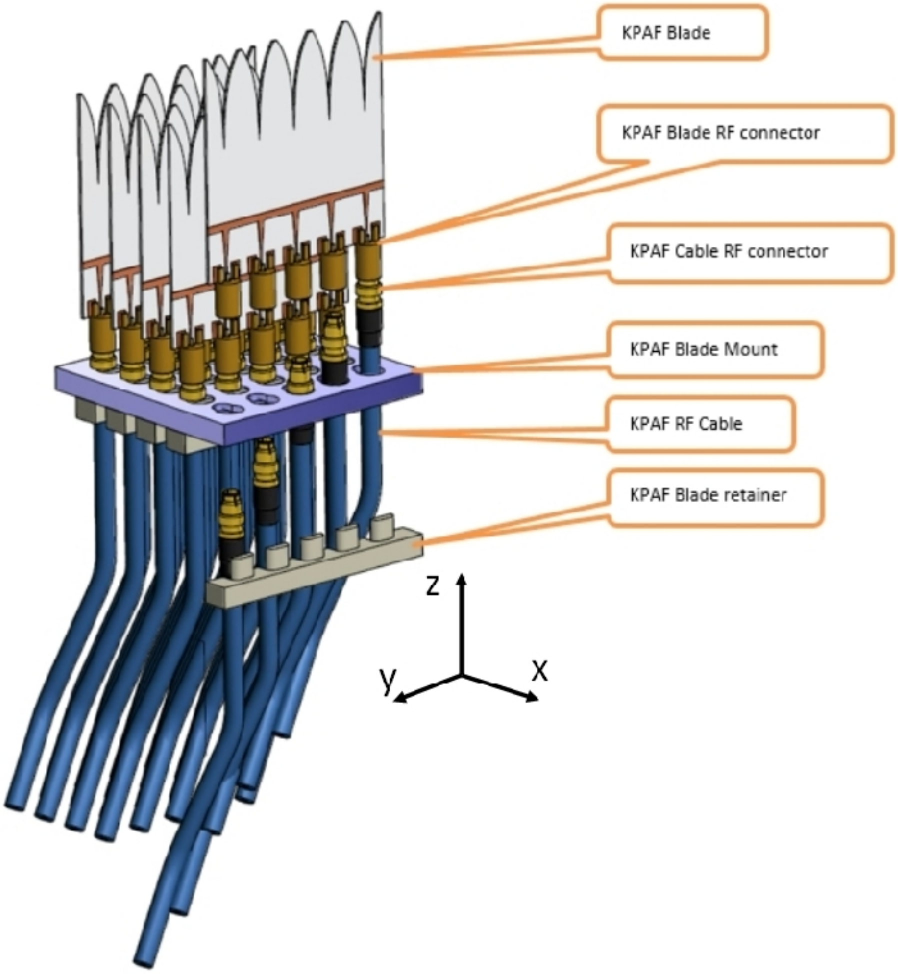

Figure 4.10: KPAF 5 x 5 array mechanical mounting design, expanded view.

Export to GRASP”, with the following parameters for each of 25 feed elements at 18, 22 and 26 GHz:

- `elevation`: $-175 \leq \theta \leq 175°$, step 5°
- `azimuth`: $0 \leq \phi \leq 150°$, step 30°[2]
- `farfield origin`: Free (x_{mm}, y_{mm})[3]
- `polarization type`: Ludwig 3: Horizontal, Vertical

Once the patterns have been imported to GRASP, the combined array patterns are now placed at the focal point of a 10 m reflector, with each beam co-located to its

---

[2] Slowly varying gain values in azimuth justify the 30° step size.

[3] (x_{mm}, y_{mm}) is the feed location for each element relative to the corner element, set to (0, 0).

original placement on a x, y grid with $d_x = d_y = 6.2$ mm spacing. Using PO/PTD the currents on the reflector and then the secondary far-field gain patterns are calculated. The resulting secondary co-polar and cross-polar gain patterns taking into account the mutual coupling of the beams are shown for 18, 22 and 26 in Figures 4.11 through 4.13.

Element Raster

Figures 4.11, 4.12 and 4.13 show the KPAF 5 x 5 array element secondary gain patterns for co-polarization and cross-polarization for 18, 22 and 26 GHz, respectively. Each image shows the gain pattern contributed by a single embedded element located at that location marked with a black dot. In essence these are the individual contributions from each KPAF element including mutual coupling. The gain values of individual elements range from 57 to 60 dBi depending on the frequency and location within the array. Generally, the element beams for 22 and 26 GHz have higher axial symmetry than at 18 GHz. This is likely due to the narrow KPAF antenna aperture, 5.8 mm, not being wide enough to provide at least a width $\geq \lambda/2$ for the electromagnetic wave to detach from the increasing antenna tapers, according to radiation mechanism for tapered slot antennas [43]. This perceives the antenna in transmit mode which is allowed by the reciprocity theorem. As mentioned in Section 3.2.2, the antenna pitch is a compromise between satisfying the grating lobe condition and the theory of radiation for tapered slot antennas favouring the higher frequency range. Thus it is likely that the beamshapes at the lower edge of the band, 18 GHz, would not be as axially symmetric as the higher frequency beams. The level of cross-polarization is extremely respectable for a densely packed planar antenna array, varying from 42 to 44 dBi, a difference of -18 to -16 dB below the median 60 dBi co-polar level.

Element Contour

Figures 4.14, 4.15 and 4.16 are contoured versions of the previous raster images in Figures 4.11, 4.12 and 4.13 for 18, 22 and 26 GHz, respectively. Co-polar and cross-polar gain contours are displayed. The contour view shows more clearly the co-polar overlap level between each element beam than in the raster image and includes the absolute gain values for each contour. The specific contour levels were chosen to minimize beam confusion.

As previously mentionend for the raster image, the element co-polar contours for

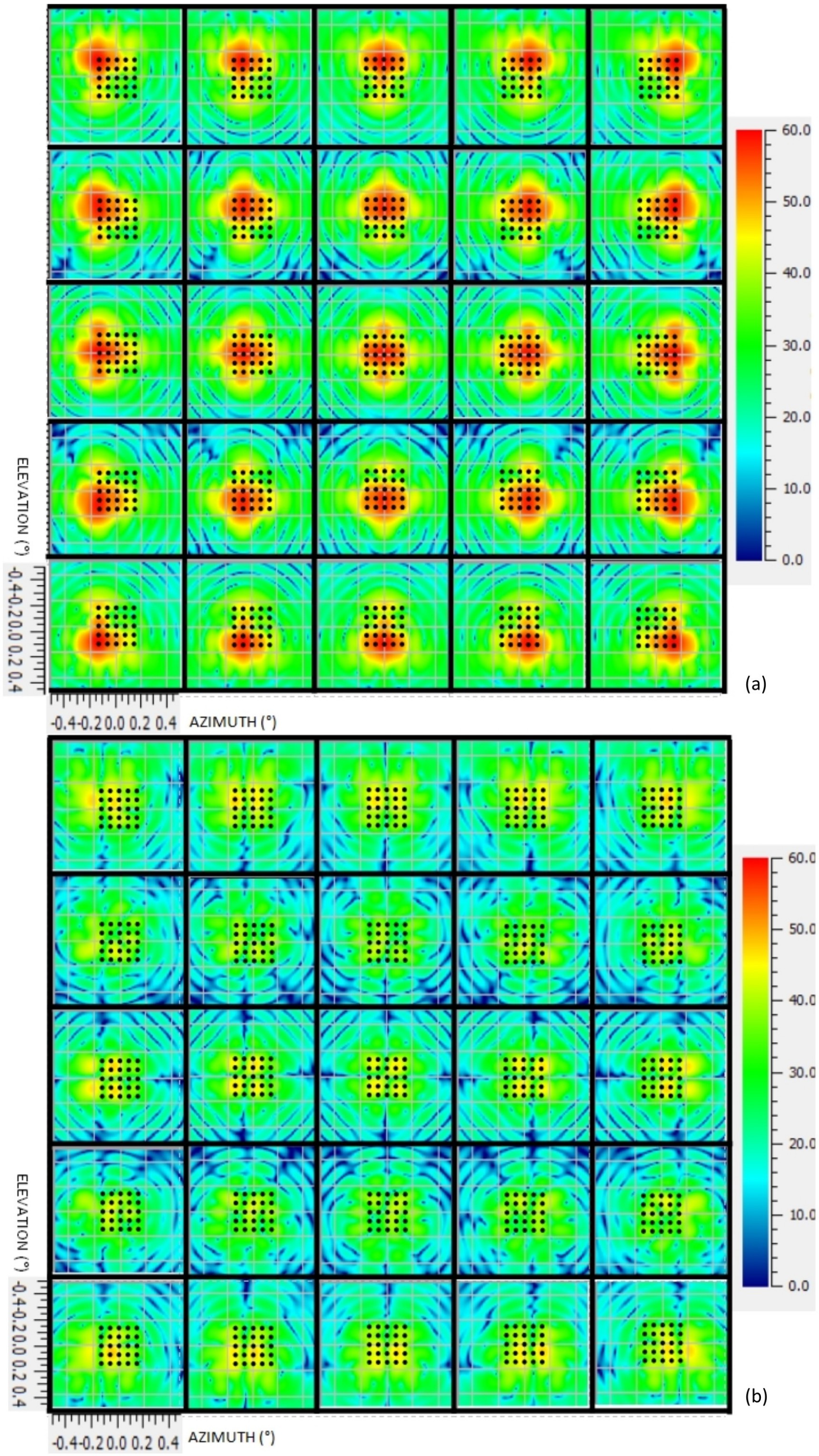

Figure 4.11: KPAF 5 x 5 array element secondary gain raster image (dBi), 18 GHz, top: co-polar, bottom: cross-polar.

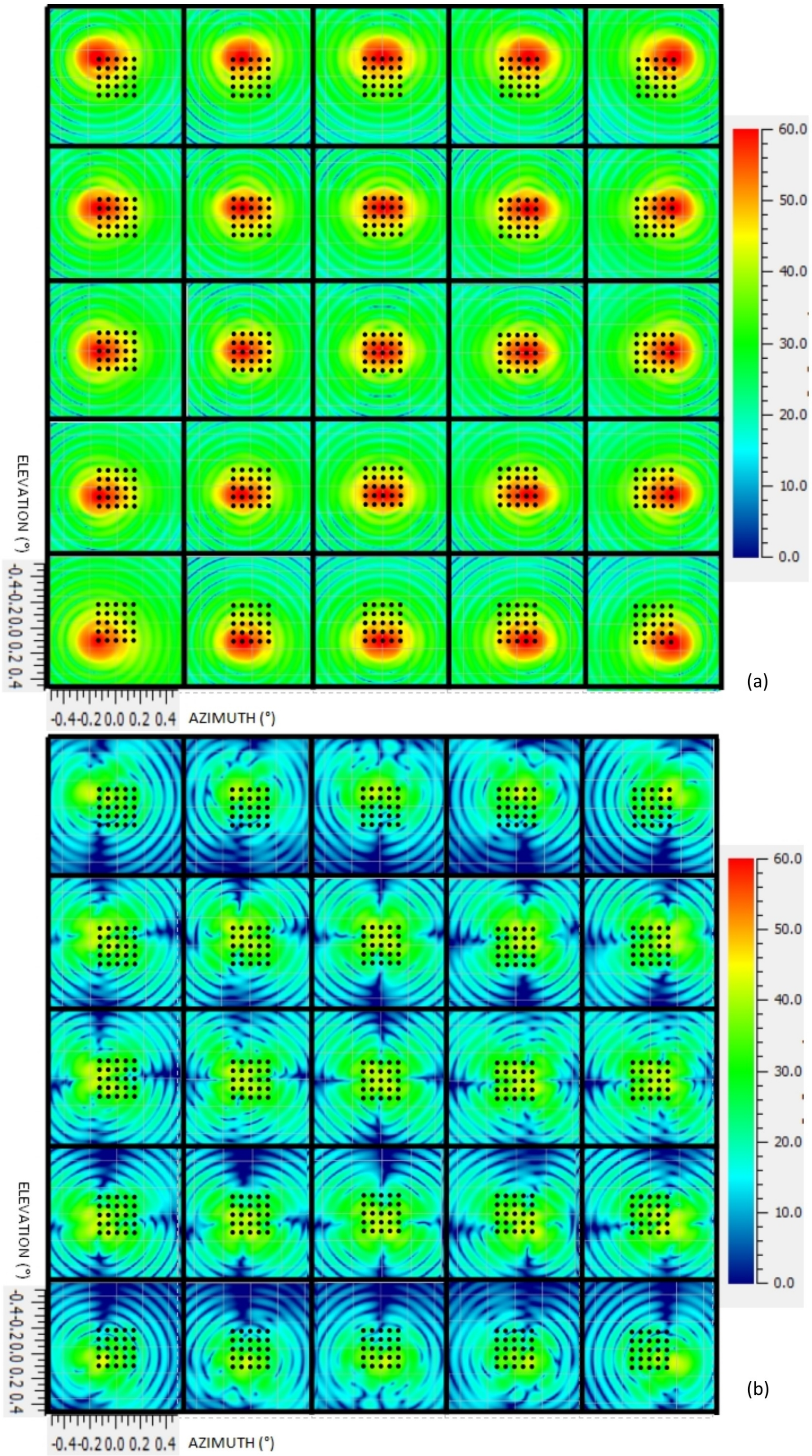

Figure 4.12: KPAF 5 x 5 array element secondary gain raster image (dBi), 22 GHz, top: co-polar, bottom: cross-polar.

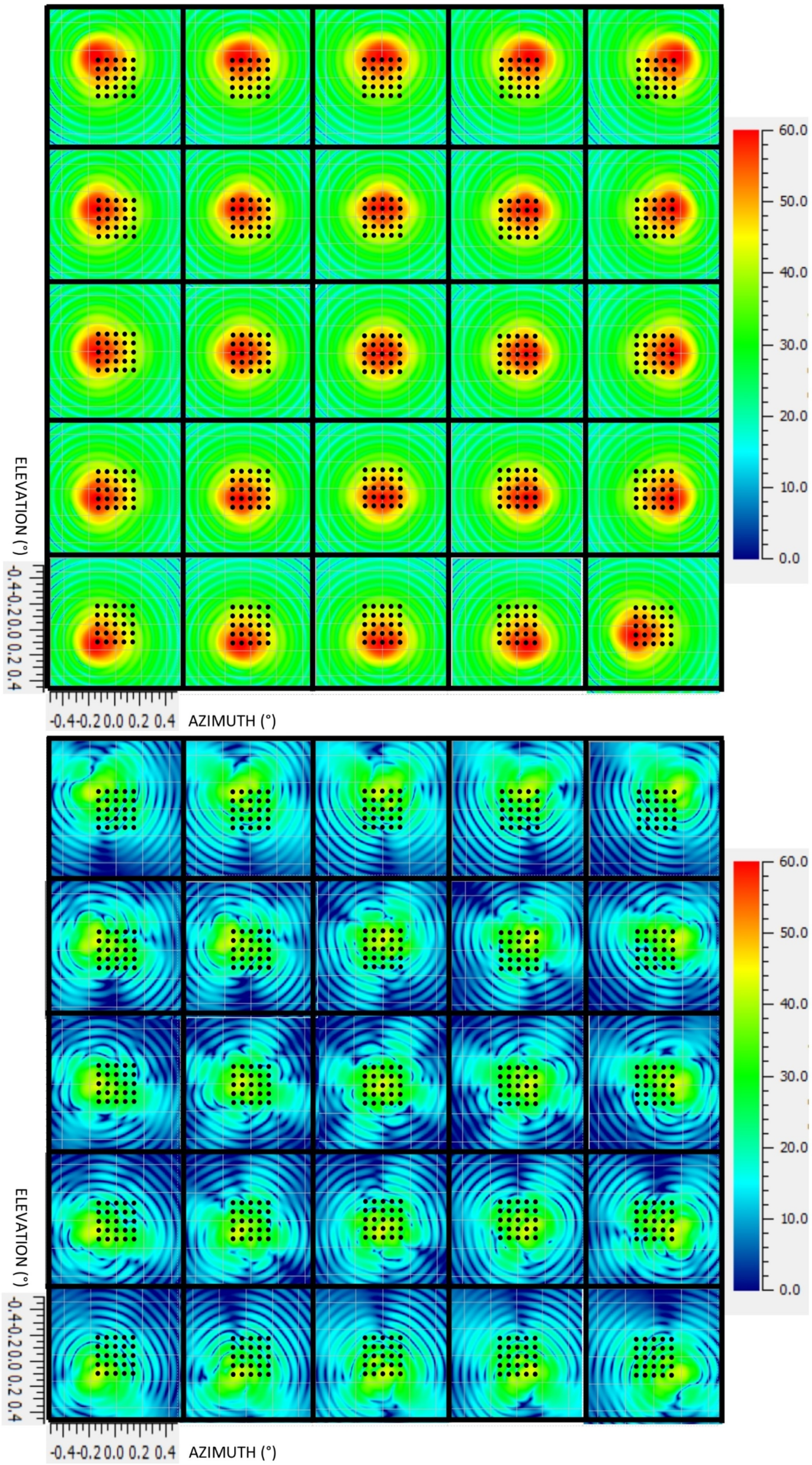

Figure 4.13: KPAF 5 x 5 array element secondary gain raster image (dBi), 26 GHz, top: co-polar, bottom: cross-polar.

18 GHz, Figure 4.14a, are not as well-shaped as for 22 GHz, Figure 4.15a, and 26 GHz, Figure 4.16a. The second and fourth rows of elements are distorted enough to alter the location of the maximum gain values for those peaks. However, the beam shapes for 22 and 26 GHz have high axial symmetry and the overlap gain levels for 18, 22 and 26 GHz over all the element beams are at most 3 dB below peak. The worst case cross-polarization levels is defined as the difference between the maximum co-polar and maximum cross-polar levels of all 25 beams are 11.6, 18.8 and 17.9 dB. This cross-polarization performance is marginal for 18 GHz but very good for 22 and 26 GHz.

In the next chapter, a synthesized beam will be produced by applying amplitude weights to the individual element. The resultant field of view is dependent on the embedded element patterns which were determined in this section and also the chosen weighting patterns. By optimizing the amplitude weightings to maximize beam efficiency and adding more elements to form a 10 x 10 or 15 x 15 array, the number of synthesized beams will be increased thus increasing the field of view.

4.4.5 5 x 5 S-Parameters

The S-parameters for a 2-port network are the input and output reflection coefficients S_{11} and S_{22} and the forward and reverse transmission coefficients S_{21} and S_{12}. For a reciprocal network of $z = 25$ antennas, the 25-port S-parameters can be displayed by one set of reflection coefficients $|S_{z,z}|\big|_{z=1,2,\ldots 25}$ and one set of transmission coefficients $|S_{z,15}|\big|_{z=1,2,\ldots 25}$, also called the mutual coupling with respect to only the centre element, $z = 15$. Only the centre element was chosen in the interest of displaying a reasonable amount of data while providing a good understanding of the array performance. The simulations are performed in the full-wave electromagnetic solver, CST Microwave Studio.

Mutual Coupling Coefficient

The mutual coupling, $|S_{z,15}|\big|_{z=1,2,\ldots 25}$ with respect to the centre element, number 15, of the 25-port antenna array are depicted in Figure 4.17. The element numbering scheme is shown which is also used for Figure 4.18. Although all twenty-five antennas are simulated, the similar datasets identify two orthogonal planes of symmetry, reducing the data to nine independent sets, outlined with the yellow square. This was unexpected as the antenna element itself is not symmetrical due to the antipodal

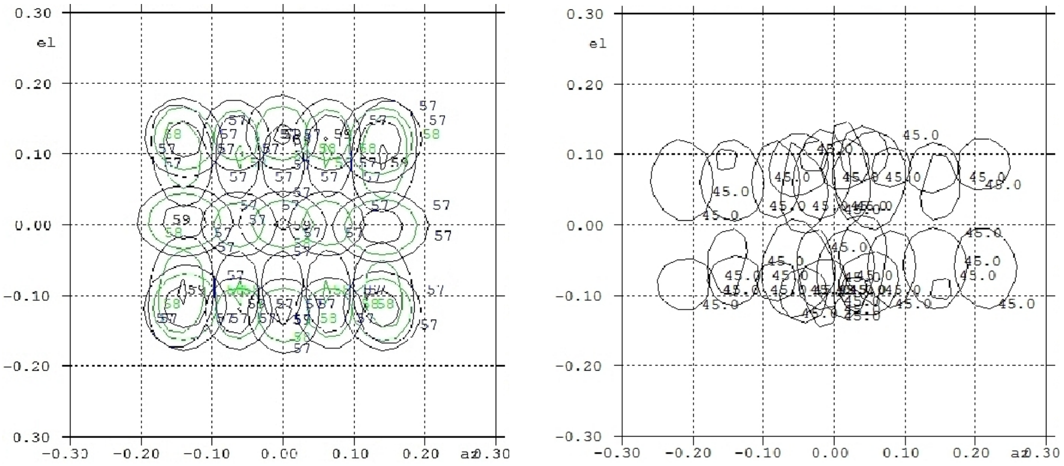

(a) element co-polar, 18 GHz.

(b) element cross-polar, 18 GHz.

Figure 4.14: KPAF 5 x 5 array element secondary gain contours (dBi), 18 GHz, x: azimuth (°), y: elevation (°). Absolute gain values noted on contours: (a) 57, 58 and 59 dBi (b) 45 dBi. Maximum peak: (a) 59.8 dBi (b) 48.2dBi.

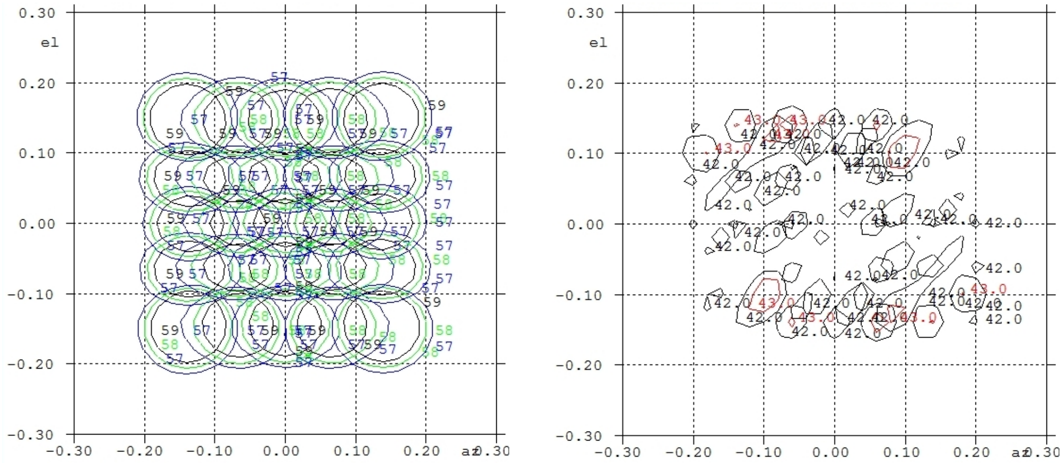

(a) element co-polar, 22 GHz.

(b) element cross-polar, 22 GHz.

Figure 4.15: KPAF 5 x 5 array element secondary gain contours (dBi), 22 GHz, x: azimuth (°), y: elevation (°). Absolute gain values noted on contours: (a) 57, 58 and 59 dBi (b) 42, 43 dBi. Maximum peak: (a) 62.6 dBi (b) 43.8 dBi

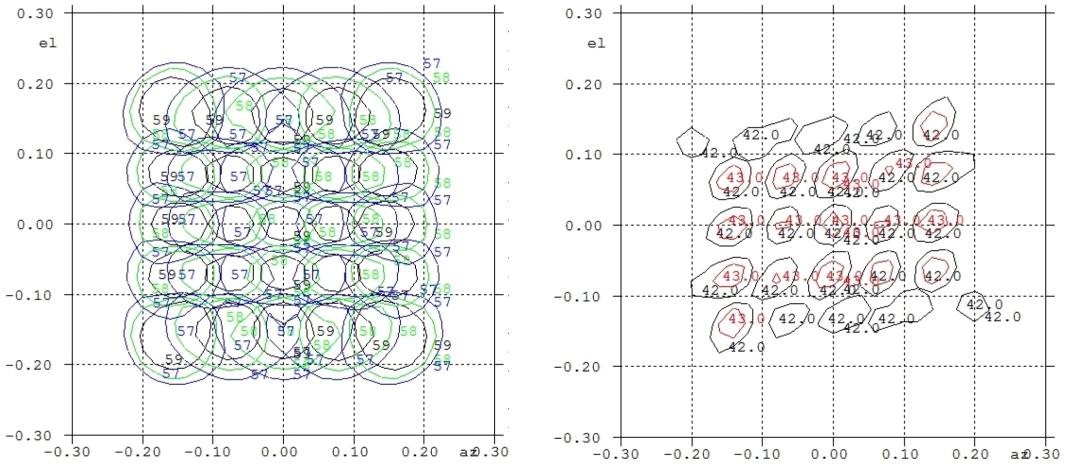

(a) element co-polar, 26 GHz.

(b) element cross-polar, 26 GHz.

Figure 4.16: KPAF 5 x 5 array element secondary gain contours (dBi), 26 GHz, x: azimuth (°), y: elevation (°). Absolute gain values noted on contours: (a) 57, 58 and 59 dBi (b) 42, 43 dBi . Maximum peak: (a) 61.7 dBi (b) 43.8 dBi.

nature of the tapered slot section, thus the array does not strictly possess symmetry which would be advantageous in reducing computation complexity. However, when computing the effects of mutual coupling, each antenna element is treated as a unit, and the relative offsets from the centre pixel create two functional planes of symmetry which is seen in the data displayed in the figure. These nine sets of data are shown under the port numbering scheme, with the included S-parameters noted.

The simulated mutual coupling coefficients of the neighbouring elements, numbers 11 and 19, peak at -12.2 dB, but the rest are low, generally below -20 dB. For a simulated densely packed array, this is a very good result. $|S_{15,15}|$ is technically is input reflection dataset and is discussed next.

Input Reflection Coefficient

The input reflection coefficients $|S_{z,z}|\big|_{z=1,2,\ldots 25}$ for each port are simulated and displayed in Figure 4.18. The element numbering pattern for the 5 x 5 array is defined in the mutual coupling graph, Figure 4.17. Similar coloured squares yield same patterns, resulting in two planes of symmetry, resulting in nine unique patterns outlined with a yellow square.

The simulated input reflection coefficients for elements $z = 1, 2, \ldots 25$ display very similar features, a minimum around 19.5 GHz and a rather lacklustre performance around -5 dB in the upper half of the frequency band. Above 21 GHz, the antenna element location is irrelevant as all elements have the same values within ±2 dB. Overall, since the antenna array performs well, the element far-field gain patterns at 18, 22 and 26 GHz are sufficient and symmetric to compose evenly illuminated fields of view. Thus the individual element performance, including the input reflection coefficient is justified.

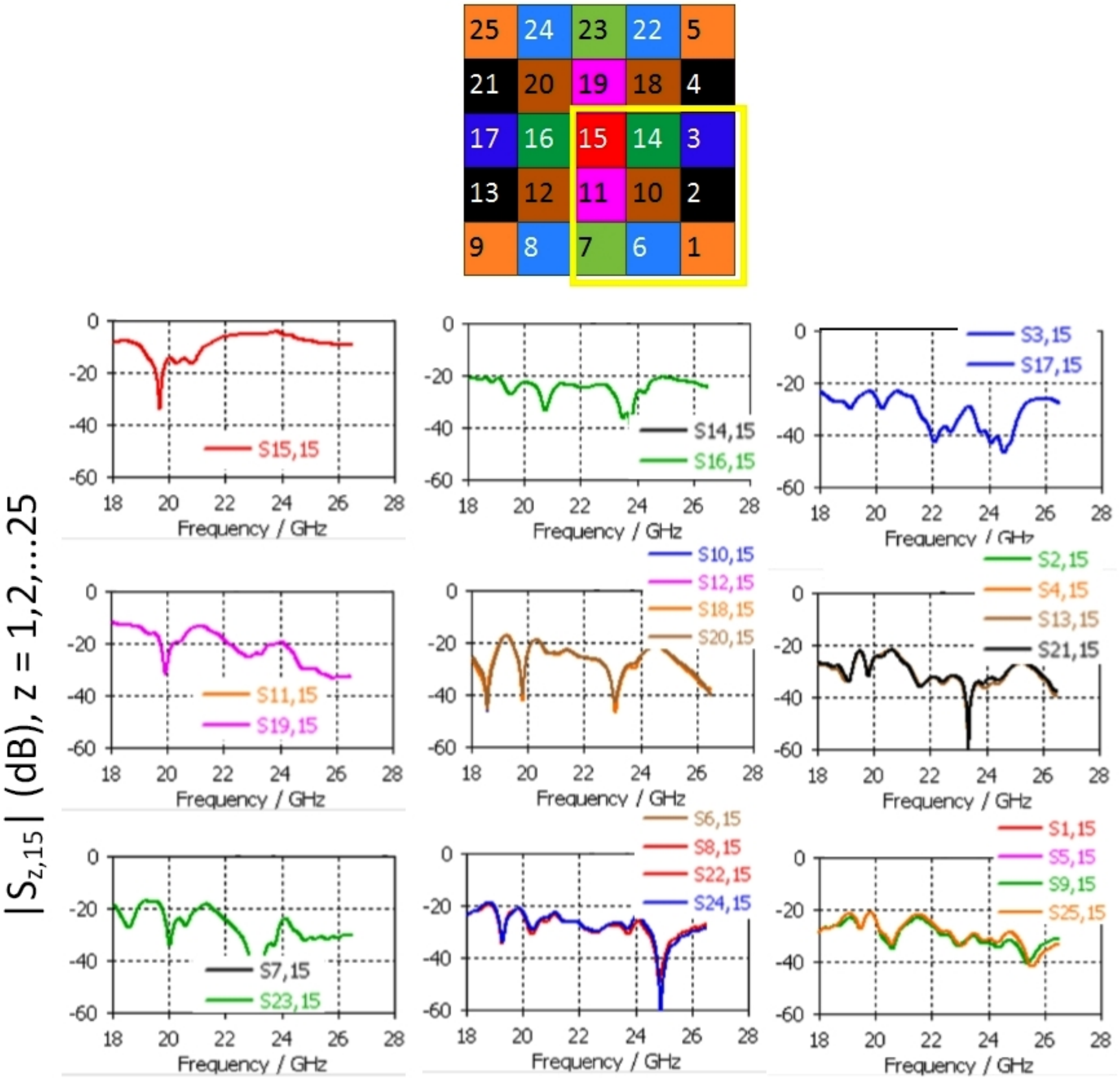

25	24	23	22	5
21	20	19	18	4
17	16	15	14	3
13	12	11	10	2
9	8	7	6	1

Figure 4.17: KPAF 5 x 5 array S-parameters, mutual coupling coefficients referenced to centre pixel, $|S_{z,15}||_{z=1,2,...25}$. Top: element numbering pattern for 5 x 5 array, also used for Figure 4.18. Similar coloured squares yield nearly identical results, demonstrating the two planes of symmetry. Yellow square outlines the nine unique patterns, shown in the graphs. Worst case mutual coupling from neighbour elements 11 and 19, peaking at -12.2 dB.

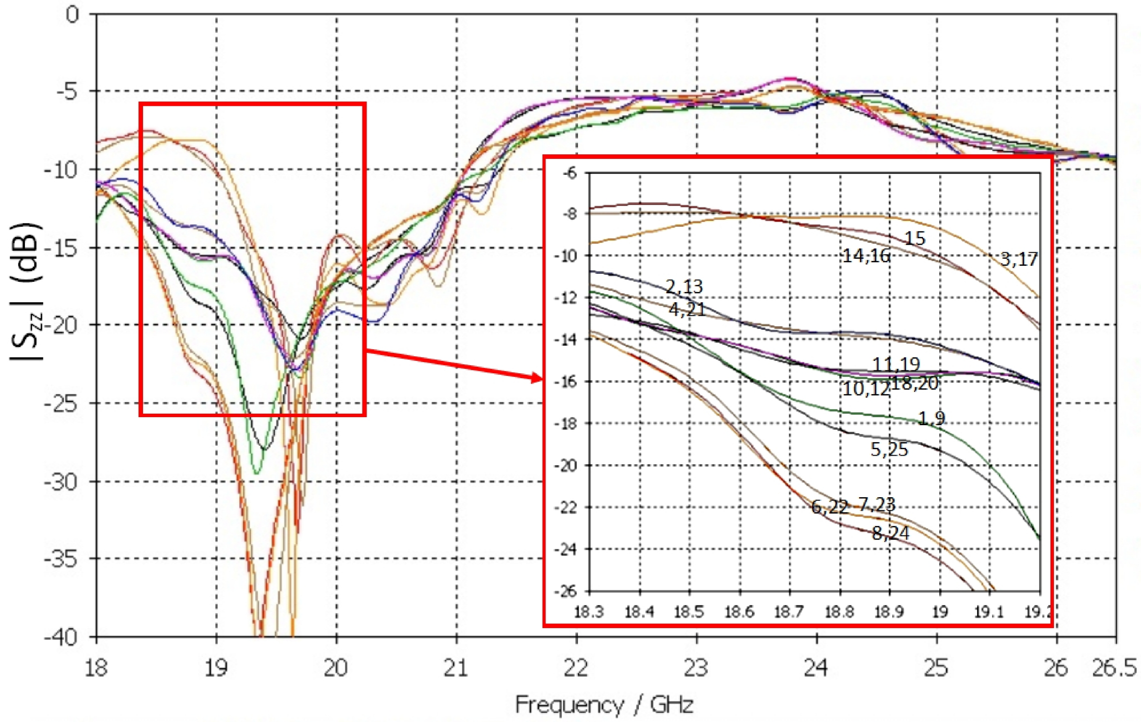

Figure 4.18: KPAF 5 x 5 array input reflection coefficients, $|S_{z,z}||_{z=1,2,...25}$. Element numbering as shown in Figure 4.17.

Chapter 5

Receiver and Beamformer

> *My God, it's full of stars.*
> - Arthur C. Clarke, 2001 : *A Space Odyssey*

To evaluate the antenna feed element and array, we need to use a receiver to amplifiy, downconvert and detect the K-band signal. This will involve mixing a portion of the band down to a lower frequency, possible filtering and further processing before detection.

5.1 Low Noise Amplifier

A cryogenic low-noise amplifier module composed of five monolithic microwave integrated circuit (MMIC) cells, each housing a single commercial GaAs MMIC amplifier chip CMD160 from Custom MMIC, was assembled and tested in-house at NRC Herzberg. The custom MMIC chip is low-noise, low-power and has 50 Ω matched ports, eliminating the need for external DC blocks and RF port matching. The housing is gold-plated tellurium copper with ten RF connectors, two per channel of Southwest Microwave 2.92 mm panel mount type. There are three DC bias terminals for ground, drain voltage, V_d, and gate voltage, V_g that are daisy-chained to each of the five amplifier sections. The chassis body is common with the chip ground and 10,000 pF and 100 pF bypass and coupling chip capacitors are needed for the drain and gate bias supplies. The transmission lines are 0.127 mm thick and 50 Ω and are wire bonded to the 2.92 mm coaxial connectors and to the MMIC input and output terminals. To prepare for cryogenic use, the K-type coaxial connectors have glass beads and a copper bracket is provided for test dewar mounting.

5.1.1 Manufacturing

Figure 5.1 shows the in-house CNC milling and assembly for the LNA. The unit was gold plated after machining and one of the five channel was populated with the MMIC, transmission lines, bypass capacitors, feed throughs for V_d, V_g, ground and RF connectors.

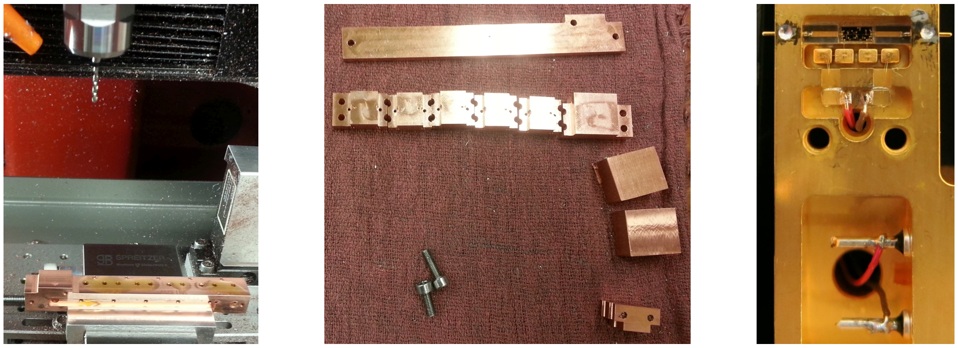

(a) (b) (c)

Figure 5.1: LNA manufacturing and assembly. (a) Milling copper body piece on CNC, (b) copper body pieces before gold plating, and (c) assembed single cavity.

The simulated model and assembled unit are shown in Figures 5.2, 5.3. The five channel model has the top lid removed to show details of the single stage MMIC amplifier.

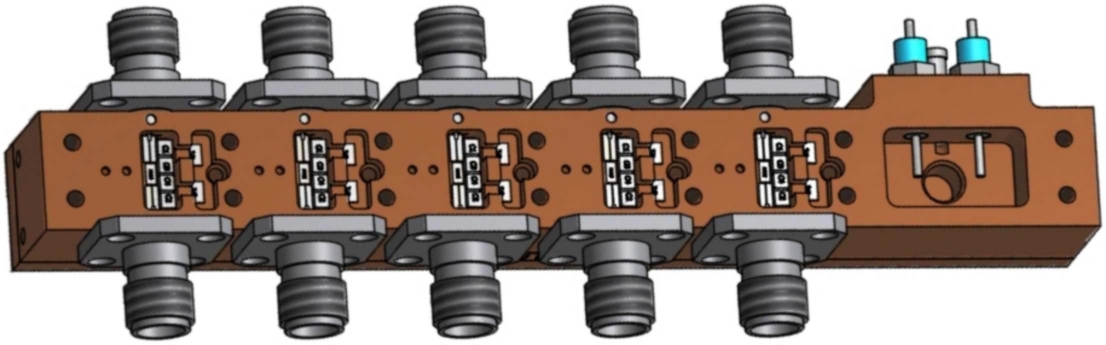

Figure 5.2: Amplifier model with populated MMIC cavities, RF and DC connectors, cover removed.

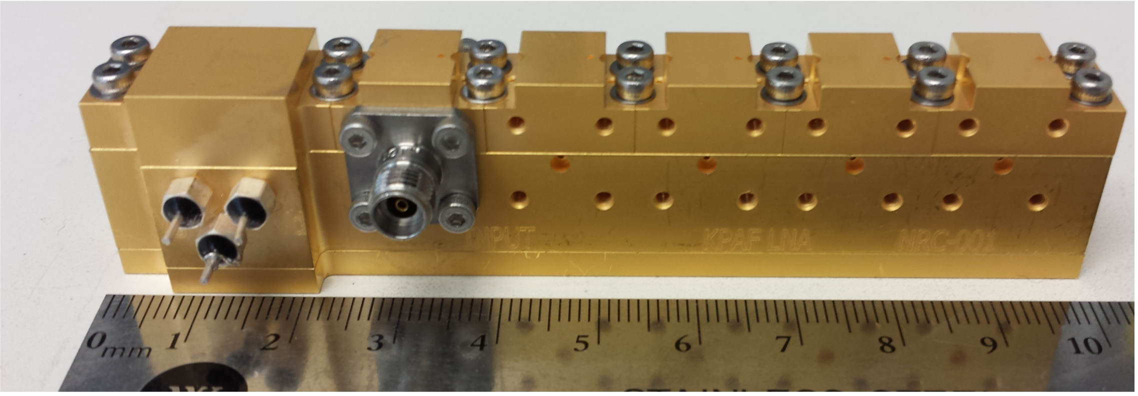

Figure 5.3: Assembled amplifier with one MMIC channel populated.

5.1.2 Vector Network Analyzer Setup

The room temperature measurements of the LNA involved both S-parameters and noise figure testing. S-parameters include S_{11}: input reflection, S_{21}: forward gain, S_{12}: reverse isolation and S_{22}: output reflection. The setup in Figure 5.4 shows the Anritsu MS4647A vector network analyzer (VNA)'s two ports connected to the input and output of the LNA. A full 2-port calibration at the end of the coaxial cables' K-type (2.92 mm) connectors moved the calibration right up to the LNA so that the device under test was solely the LNA block. The DC bias levels were provided by a dual linear power supply. The resulting data was captured on the laptop shown above the VNA.

5.1.3 Noise Figure Analyzer Setup

A noise figure analyzer (NFA), Agilent model N8975A operating from 10 MHz to 26.5 GHz using a"smart" noise source N4002A, 10 MHz - 26.5 GHz with 14 dB nominal excess noise ratio (ENR). The noise source has a built-in thermometer to monitor the ambient temperature, and transfers the value to the NFA to control the calculation of the ENR and thus the T$_{cold}$ value. This temperature compensation increases the accuracy of the overall noise figure measurement.

The NFA is calibrated to remove the contribution of the noise source as in Figure 5.5a, and the test setup is shown in Figure 5.5b.

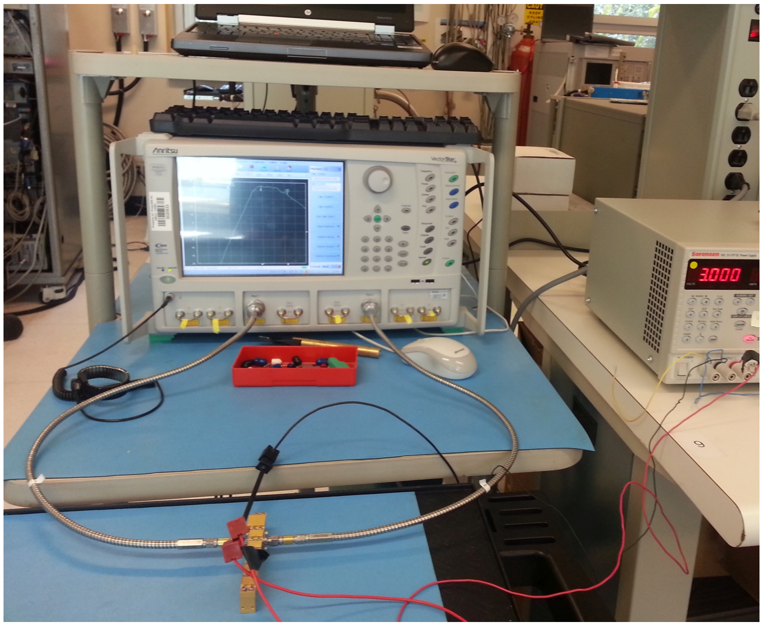

Figure 5.4: Room temperature LNA testing - S-parameters.

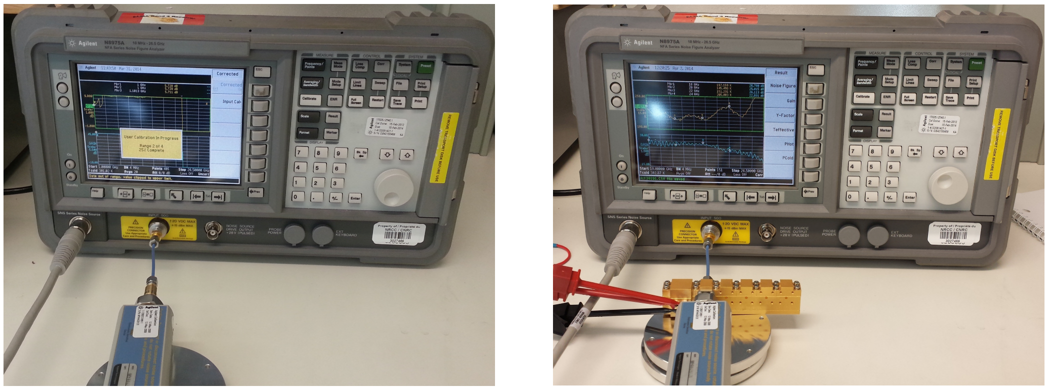

(a)

(b)

Figure 5.5: Room temperature LNA noise figure testing. (a) Calibration, and (b) testing.

5.1.4 Cryogenic Setup

In order to evaluate the cryogenic performance, the LNA was placed into a vacuum chamber, or test Dewar, evacuated to a very high vacuum, $\sim 10^{-8}$ torr, and a closed-cycle 2-stage Gifford-McMahon refrigerator is used to remove the heat. The high vacuum ensures that very little heat is transferred due to convection. The test Dewar in the lab at NRC Herzberg is routinely used for characterizing passive and active components at cryogenic temperatures and can cool the chamber from 300 K to 16 K

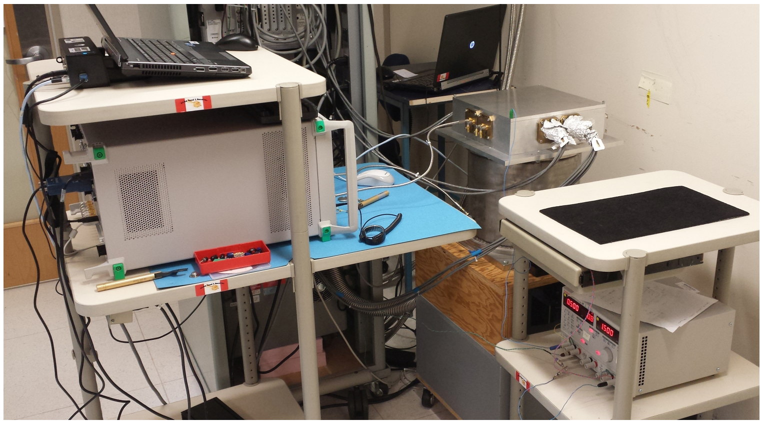

Figure 5.6: Cryogenic setup with test Dewar and VNA. NFA in rack behind VNA.

in a matter of hours. The test setup is seen in Figure 5.6

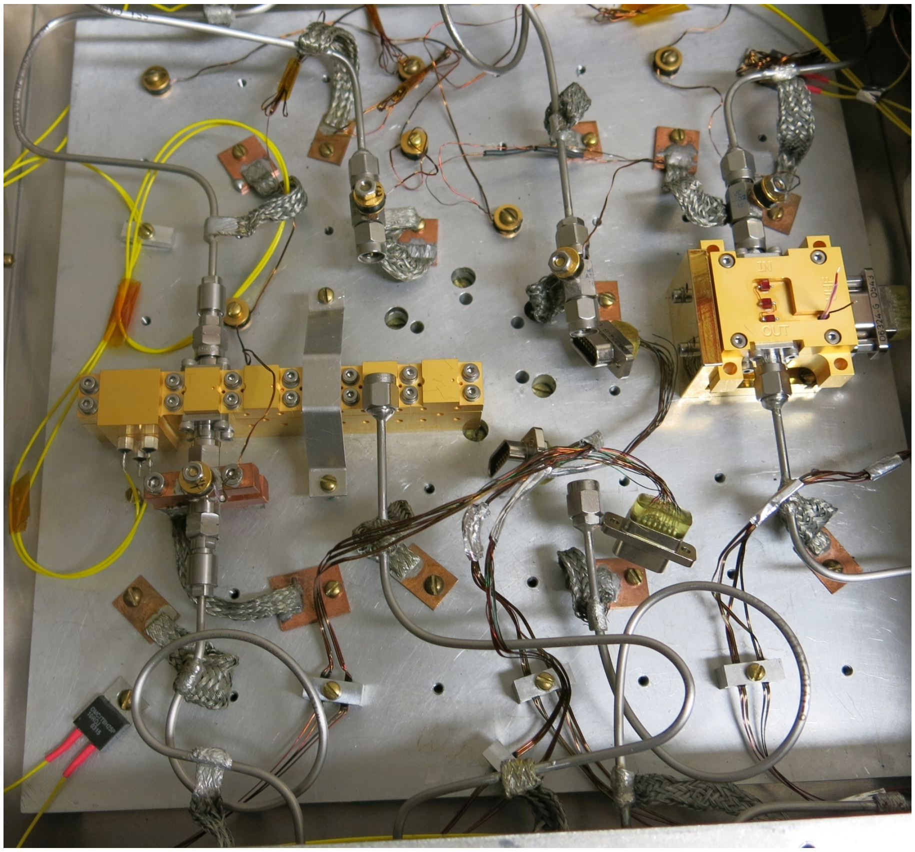

Figure 5.7: LNA cryogenic testing; bottom side is thermally mounted to Dewar plate, Lakeshore temperature sensor on LNA input calibrated resistor. LNA is gold-coloured rectangular feature on left.

Figure 5.7 shows the inside of the test Dewar. The 0.085” stainless steel coaxial cables provide electrical connection from the hermetically sealed bulkhead K-connector to the amplifier, the device under test. A calibrated attenuator is included in the device under test to reduce unwanted reflections from the amplifier input, as input return loss values of -5 dB are not uncommon. The effect of the attenuator is removed in the calculations of the VNA and the noise figure meter. Stainless steel cables connect the amplifier output to the output of the test Dewar. The DC bias cables run through a hermetically sealed connector also.

5.1.5 LNA Bias Levels

The MMIC datasheet for the CMD160 chip states the room temperature performance for 17 - 25 GHz is 26.5 dB peak gain, 1.4 dB minimum noise figure. The nominal bias levels are V_d = 3.0 V, V_g = 1.5 V, I_d = 26 mA. For room temperature testing, these bias levels were adhered to, but for cryogenic temperatures they were varied, while staying below the reported maximums, in order to observe any variation in measured S-parameters and noise figure testing.

5.1.6 Noise Figure and Noise Temperature Definitions

Both terms, noise figure and noise temperature are often used when discussing cryogenic and room temperature performances of microwave components. It is important to realize the difference:

$$T = (F - 1)T_0 \tag{5.1}$$

where T = component noise temperature [K], T_0 = physical temperature of component [K] and F = noise figure [dimensionless]. If the two-port contributes zero noise, T = 0 and F = 1. For low-noise components, F is slightly greater than 1, and it is common practice to specify the noise temperature instead of the noise figure. Noise figure is often excessed in decibels:

$$F_{dB} = 10\ \log_{10} F \tag{5.2}$$

Although the noise parameter on the CMD160 datasheet is given in dB, the convention here will be to present noise as noise temperature in Kelvins.

5.1.7 S-parameters and Noise Temperature

Room temperature and cryogenic S-parameters and noise temperature tests for various bias settings are performed.

The full S-parameters, S_{11}, S_{12}, S_{21} and S_{22} are shown in Figures 5.8 and 5.9 as a function of frequency and V_d and V_g bias settings at 303 K and 13 K physical temperatures. S_{12} peaks at 40 dB, performing best at the low end of the band. The best overall S_{11} is attained with a high bias setting of $V_g = 3.5$ V, $V_d = 1.5$ V, with a very consistent performance with frequency but slightly better at high frequencies. Both room temperature and cryogenic S_{22} is best at 22 GHz, while staying better than 5 dB for room temperature and 9 dB for cryogenic temperatures. Room temperature S_{21} peaks at 28 dB, but cryogenic S_{21} peaks at 34 dB when the $V_d = 1.5$ V and $V_g = 2.0$ V.

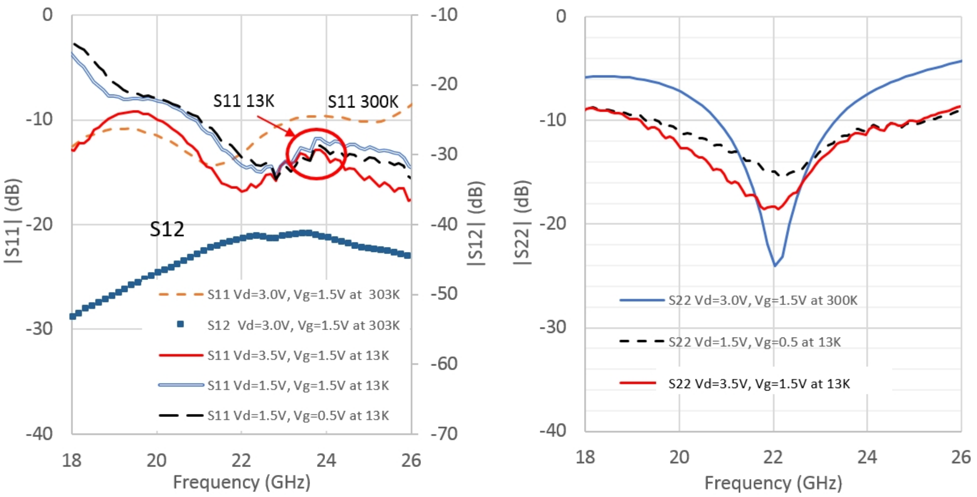

Figure 5.8: LNA S_{11}, S_{12}, S_{22}, at 13K and 300K physical temperatures for various V_d and V_g bias settings.

The noise temperature in Figure 5.10 is measured at room temperature, 303 K and cryogenic temperature, 13 K at various bias settings, V_d and V_g shows optimum performance around 20 GHz for both cryogenic, 13 K and room temperatures, 303 K. At 303 K the noise temperature is 150 K and the gain is 26 dB at 22 GHz. At 13 K physical temperature, the lowest noise temperature is 20 K at 20 GHz with $V_d = 1.5$ V, $V_g = 0.5$ V bias settings, and 12.9 mW dissipated power; but this is also the least gain at cryogenic temperatures, 29 dB. A good compromise is achieved with $V_d = 1.5$ V, $V_g = 2.0$ V, 32.5 mW dissipated power with 33 dB gain and 21 K noise temperature at 20 GHz.

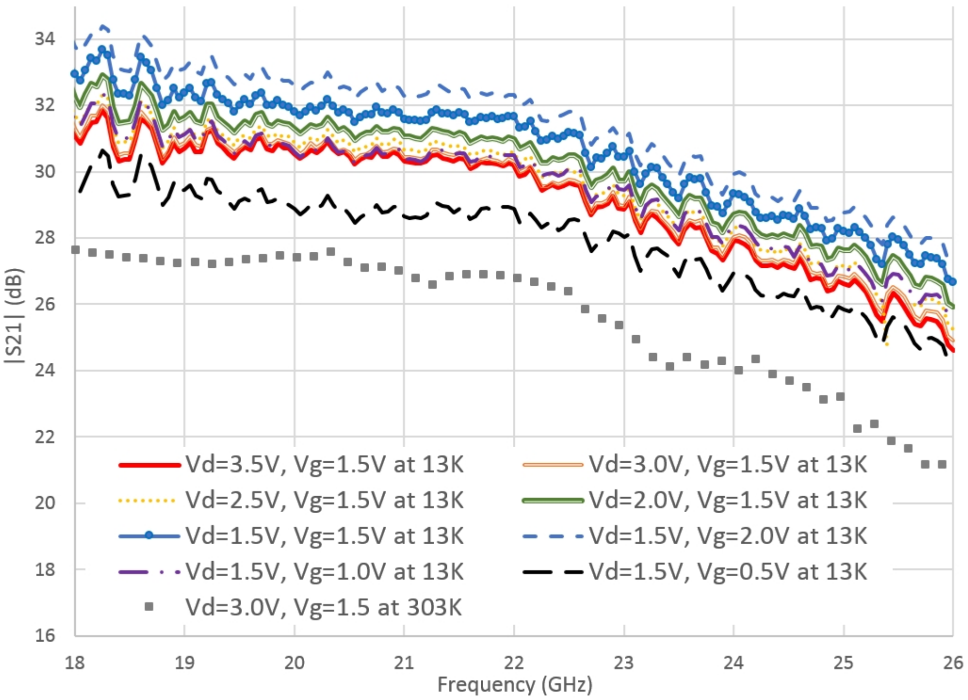

Figure 5.9: LNA S_{21} as a function of bias settings, all at 13 K except grey square dataset at 300 K physical temperature.

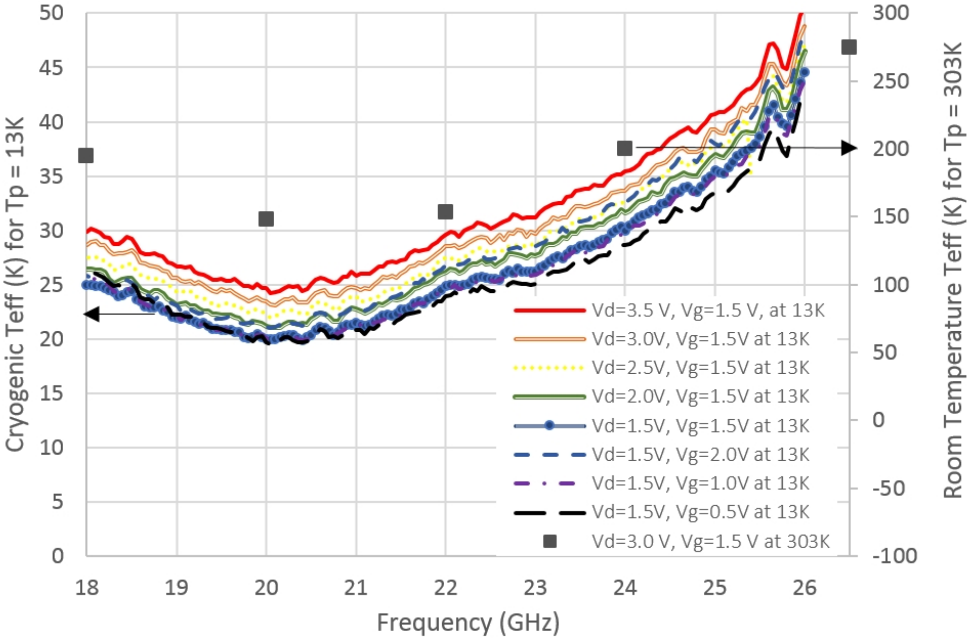

Figure 5.10: LNA noise temperature as a function of bias settings, all at 13K except square dataset at 300 K physical temperatures.

5.2 Downconverting Mixer

A frequency down converter for an RF of 18 - 26 GHz, specifically 23.6 - 24.2 GHz to cover the first four ammonia lines, to an IF of 0.8 - 1.5 GHz, Figure 5.11, is needed to interface with existing instrumentation at NRC Herzberg in Penticton which consists of a baseband mixer and analog beamformer.

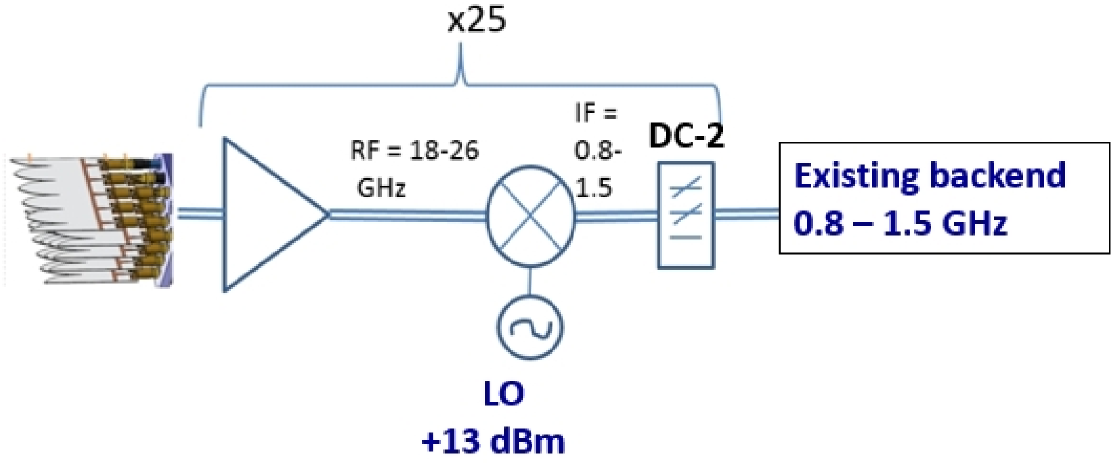

Figure 5.11: System block diagram including mixer frequencies.

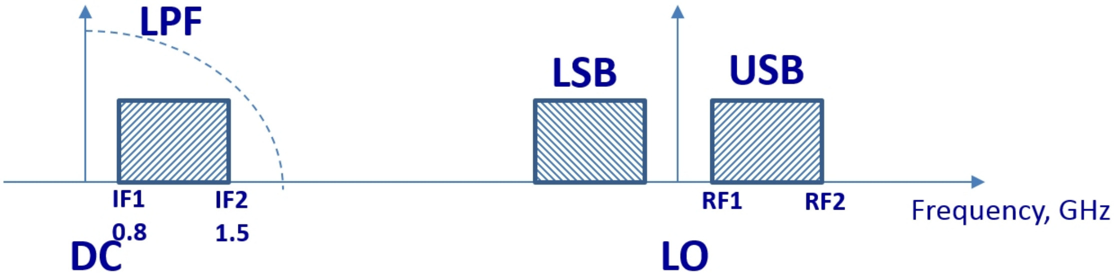

Figure 5.12: Mixer frequency chart showing upper side band (USB), lower side band (LSB), the downconverted IF block and the low pass filter (LPF).

Figure 5.11 shows the system block diagram with mixer frequency information. The intermediate frequency (IF) is set by the existing backend to be 0.8 - 1.5 GHz. When determining the local oscillator frequency, the diagram in Figure 5.12 can aid in calculating the upper and lower side bands. To observe the lowest end of the K band, 18.0 - 18.7 GHz, the LO required is:

RF centre frequency: 18.35 GHz
IF centre frequency: 1.15 GHz
LO = RF - IF = 16.20 GHz

To observe the ammonia molecules the RF frequency band is 23.6 - 24.2 GHz and the LO required is:

RF centre frequency: 23.90 GHz
IF centre frequency: 1.15 GHz
LO = RF - IF = 22.75 GHz

To observe the highest end of the K band, 25.3 - 26.0 GHz, the LO required is:

RF centre frequency: 25.65 GHz
IF centre frequency: 1.15 GHz
LO = RF - IF = 24.50 GHz

For full coverage of the 18 - 26 GHz band, in 0.7 GHz segments, the LO needs to be able to tune from 16.20 to 24.50 GHz.

The K-band mixer design is a packaged Hittite MMIC mixer chip model HMC260, a passive double balanced mixer with 50 Ω ports with an added 2-pole LC lumped element low pass filter on the IF port. The electrical layout is shown in Figure 5.13 with the RF, IF and LO ports labelled and the aluminum body design shown in Figure 5.14.

The transmission line is 50 Ω microstrip on Rogers RT/Duroid 5880 substrate with 0.127 mm thickness. The trace is 1.27 mm wide and has a nominal length of 4 mm which can be adjusted to fit. An aluminum chassis has been designed; as this component will not be cryogenically cooled, there is no need for more expensive copper with higher thermal conductivity.

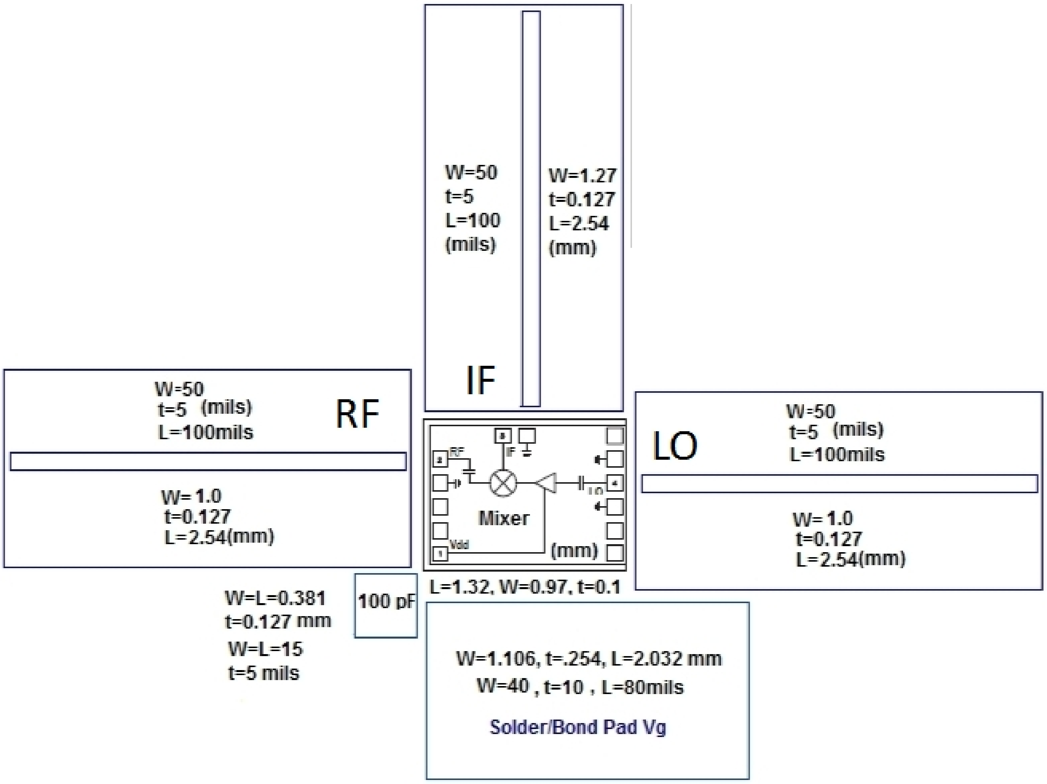

Figure 5.13: Mixer electrical layout.

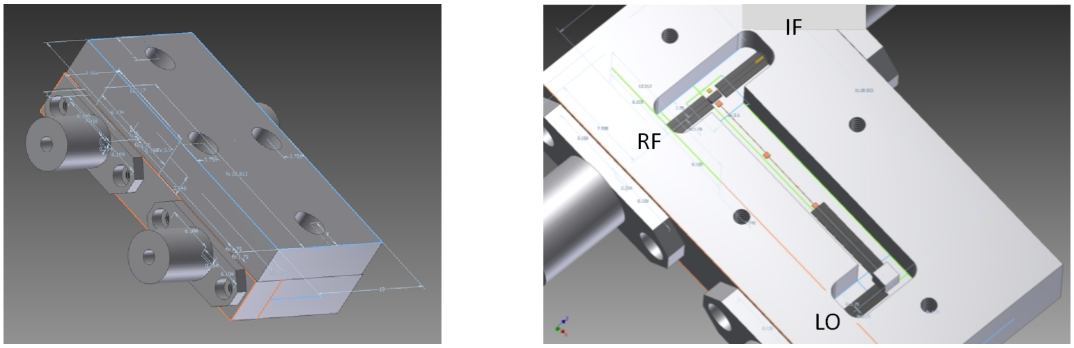

(a) (b)

Figure 5.14: Mixer body design, (a) lid on (b) lid off.

The LO requires +13 dBm power, and we expect 8 to 10 dB conversion loss as per the Hittite datasheet in Appendix E.

5.3 Beamfomer Architectures

Antenna elements, when densely packed spaced by 0.5λ, justifiably need to be small, by themselves will generally over-illuminate the telescope reflector. In order to optimize the illumination, the spillover and taper efficiencies can be optimized by adjusting the amplitude and phase weights and coherently combining the results as in Figure 5.15. Fisher and Bradley [65] mention that typically seven or more elements are needed to form each beam and that forming beams with a PAF is very much like a typical phased array. The complex weights are chosen sometimes in a ring pattern as long as most of the power for a given beam falls on the elements.

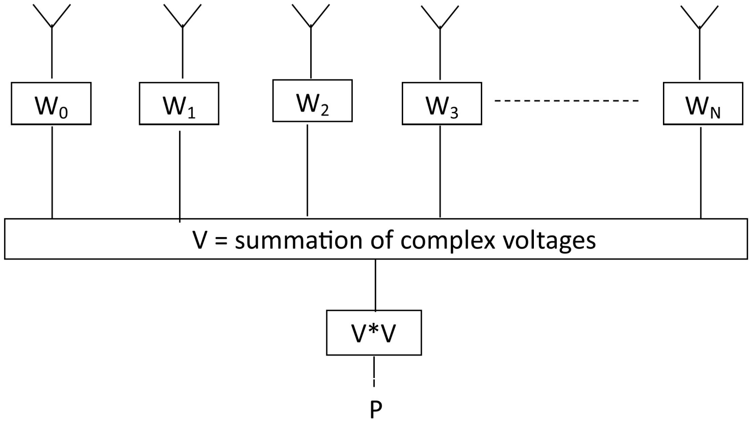

Figure 5.15: Direct signal combination beam forming network.

The type of beam forming network shown in Figure 5.15 is called direct signal combination and involves giving a subset of the array elements a complex weighting, $\mathbf{W}_n$ and summing them, V, to form one beam. The detected power P is the magnitude of the complex conjugate of V.

A second type of beam forming network is shown in Figure 5.16. This method involves the self-correlation of all elements used to form one beam to create a set of complex cross- and auto-correlation values. Complex weights, U_n and summed to produce P, the beam power output. Although much more complicated and expensive, this method allows for the beam formation to be done in software and reprocessed with various weighting schemes.

Whichever hardware configuration is used in the future, the final product, the synthesized beams, can be simulated using CST as shown in the next section.

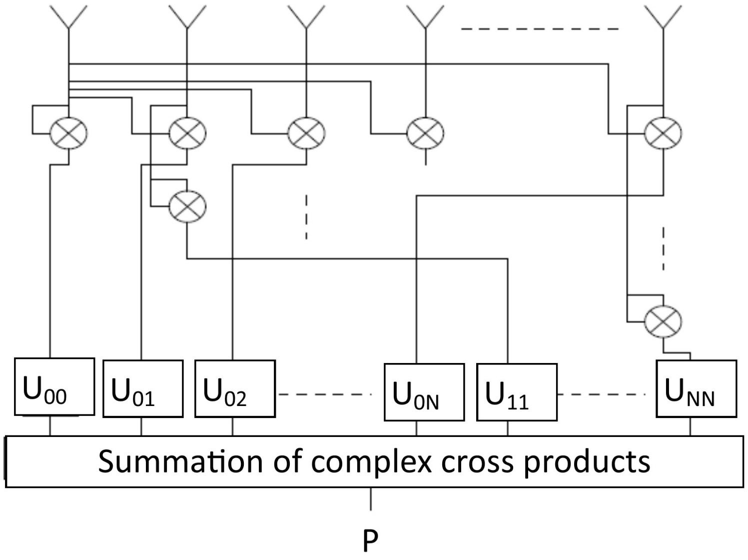

Figure 5.16: Correlation beam forming network.

5.4 Parabolic Reflectors and Efficiencies

Balanis defines aperture efficiency ϵ_{ap} as a function of many other efficiencies [69]:

$$\epsilon_{ap} = \epsilon_s \epsilon_t \epsilon_p \epsilon_x \epsilon_b \epsilon_r \tag{5.3}$$

spillover efficiency: ϵ_s is the fraction of the total power that is radiated by the feed, intercepted and collimated by the reflecting surface.

taper efficiency: ϵ_t is the uniformity of the amplitude distribution of the feed pattern over the surface of the reflector.

phase efficiency: ϵ_p is the phase uniformity of the field over the aperture plane.

polarization efficiency: ϵ_x is the polarization uniformity of the field over the aperture plane.

blockage efficiency: ϵ_b is the efficiency due to any blockage in front of the reflector.

random error efficiency: ϵ_r is the efficiency due to random errors over the reflector surface.

The directivity and aperture efficiency can be calculated depending on the primary radiation characteristic, that is the primary feed pattern. For a given feed pattern all paraboloids with the same F/D ratio have identical aperture efficiencies.

The classic graphs in [69] display the maximum aperture efficiency as a function of F/D, and the associated taper and spillover efficiency values. For a F/D of 0.45, the ideal feed pattern, maximizing aperture efficiency, is midway between a $\cos^2$ and $\cos^4$ feed pattern.

By using numerical techniques it is possible to compute either the expected aperture efficiency for a given beam, or the ideal beam width to achieve maximum aperture efficiency. For subsequent calculations only the spillover and taper efficiency terms will be taken into account as the remaining efficiencies can be approximated to 1.

5.5 Synthesized Beams

Using CST and simulating the 5 x 5 array with various weights for the elements, it can be seen that at least in gain and beam shape, there is an optimum set of complex weights. The middle ring and outer rings are defined in each of Figures 5.17, 5.18 and 5.19. The following complex weight configurations are simulated and discussed:

1. Centre element only: $1\angle 0°$, all others: $0\angle 0° =$ terminated.
2. Ring structure, centre element: $1\angle 0°$, middle ring: $0.1\angle 0°$ and outer ring: $0.01\angle 0°$.
3. Optimized ring structure, centre element: $1\angle 0°$, middle ring: $0.403\angle 0°$, outer ring: $0\angle 0° =$ terminated.

5.5.1 Synthesized Beam with Centre Element Only

To form a baseline for further weighting patterns, a simulation of the synthesized beam with only the centre element excited and all other elements terminated is shown in Figure 5.17. This results in the least gain of all three configurations, 4.06 dB maximum at bore sight direction. A reasonably good beam shape is attained although slightly asymmetrical. The principle polar cuts show HPBW of 131.4° in the E-plane and 94.4° in the H-plane and also significant side lobes in the H-plane. By changing the amplitude weights the beamshape can be optimized to reduce the side lobes and attain a beam width optimized for the reflector.

5.5.2 Synthesized Beam with Ring Structure

Figure 5.18 represents a simulation of the synthesized beam with ring structured element weightings 0 dB, -10 dB, -20 dB (0, 0.1, 0.01) for the centre element, first ring and second ring, respectively, with zero phase weightings. By lightly weighting the outer rings, the maximum gain is 9.3 dB. The principle polar cuts show HPBW of 45.0° in the E-plane and 46.4° in the H-plane and smaller side lobes in the H-plane than for the centre element only case. The beam symmetry has also dramatically improved over the single element excitation.

5.5.3 Synthesized Beam with Optimized Ring Structure

After some calculations to optimize the product of illumination and spillover efficiencies [13], the following set of beam weights was chosen, centre element: $1.0\angle 0°$, inner ring: $0.403\angle 0° = -4$ dB$\angle 0°$), outer ring: $0\angle 0°$. With these amplitude weights the highest gain, 12.3 dB, the most symmetric beam and the lowest side lobes of all three configurations are obtained in Figure 5.19. The principle polar cuts show HPBW of 43.1° in the E-plane and 42.2° in the H-plane. Again, the lightly weighted inner and outer rings act as a buffer required to provide the centre element with an appropriate boundary to enhance the radiation pattern.

Optimization of the element weightings is ongoing. This is a first step, and future designs will incorporate the modularity of the 5 x 5 KPAF to create 10 x 10 or 15 x 15 element systems providing many more beams.

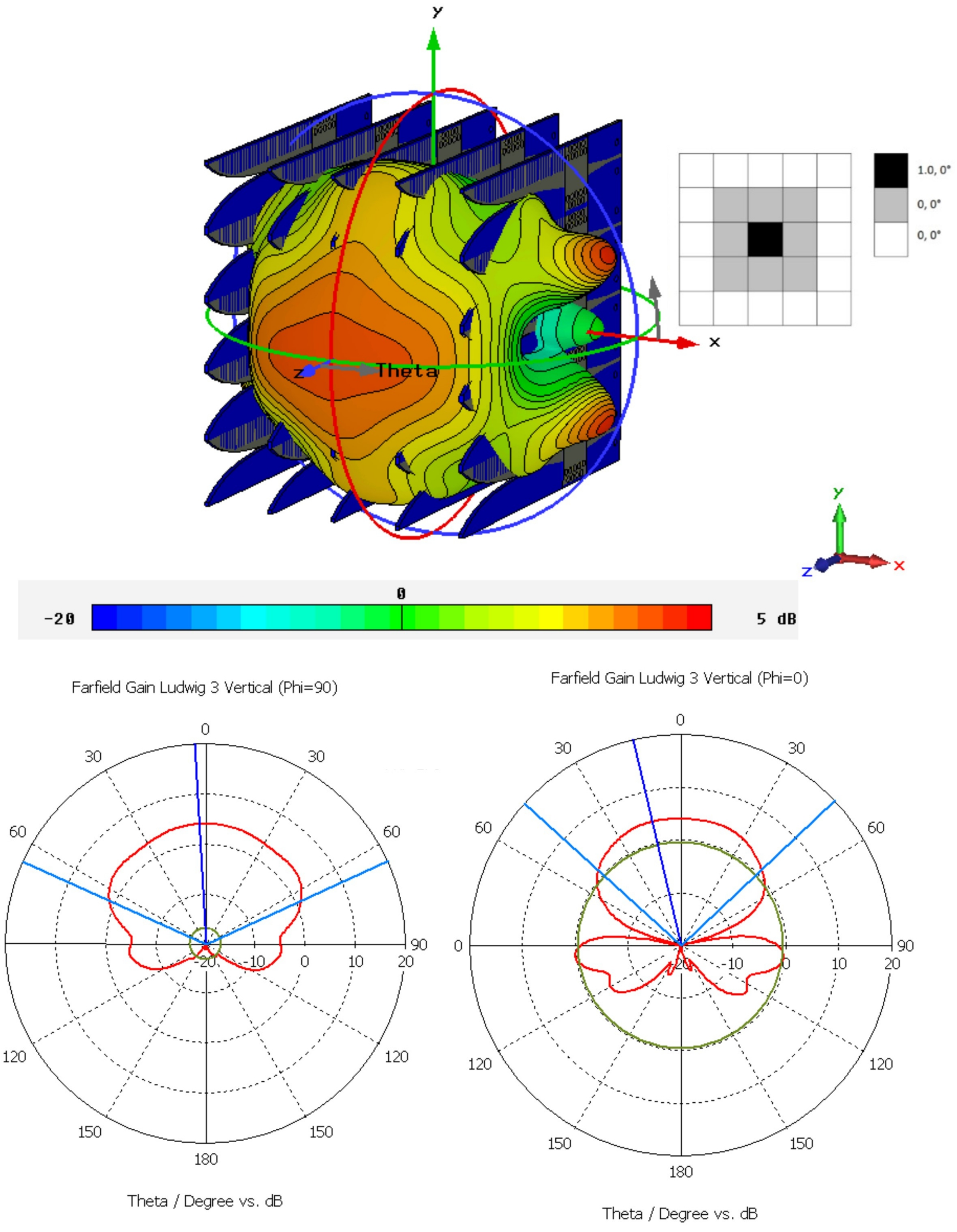

Farfield Gain Ludwig 3 Vertical (Phi=90)

Farfield Gain Ludwig 3 Vertical (Phi=0)

```
Frequency = 22
Main lobe magnitude =     3.98 dB
Main lobe direction =    3.0 deg.
Angular width (3 dB) =  131.4 deg.
Side lobe level =  -20.6 dB
```

```
Frequency = 22
Main lobe magnitude =     4.06 dB
Main lobe direction =   13.0 deg.
Angular width (3 dB) =   94.4 deg.
Side lobe level =   -4.5 dB
```

Figure 5.17: Gain of synthesized beam (dB) of 5 x 5 array with element amplitude and phase weightings: centre element: $1.0\angle 0°$, inner ring: $0\angle 0°$, outer ring: $0\angle 0°$. Contours represent 1 dB steps. The physical array structure demonstrates orientation. E-plane ($\phi = 90°$) and H-plane ($\phi = 0°$) polar cuts including HPBW and maximum side lobe levels. 22 GHz.

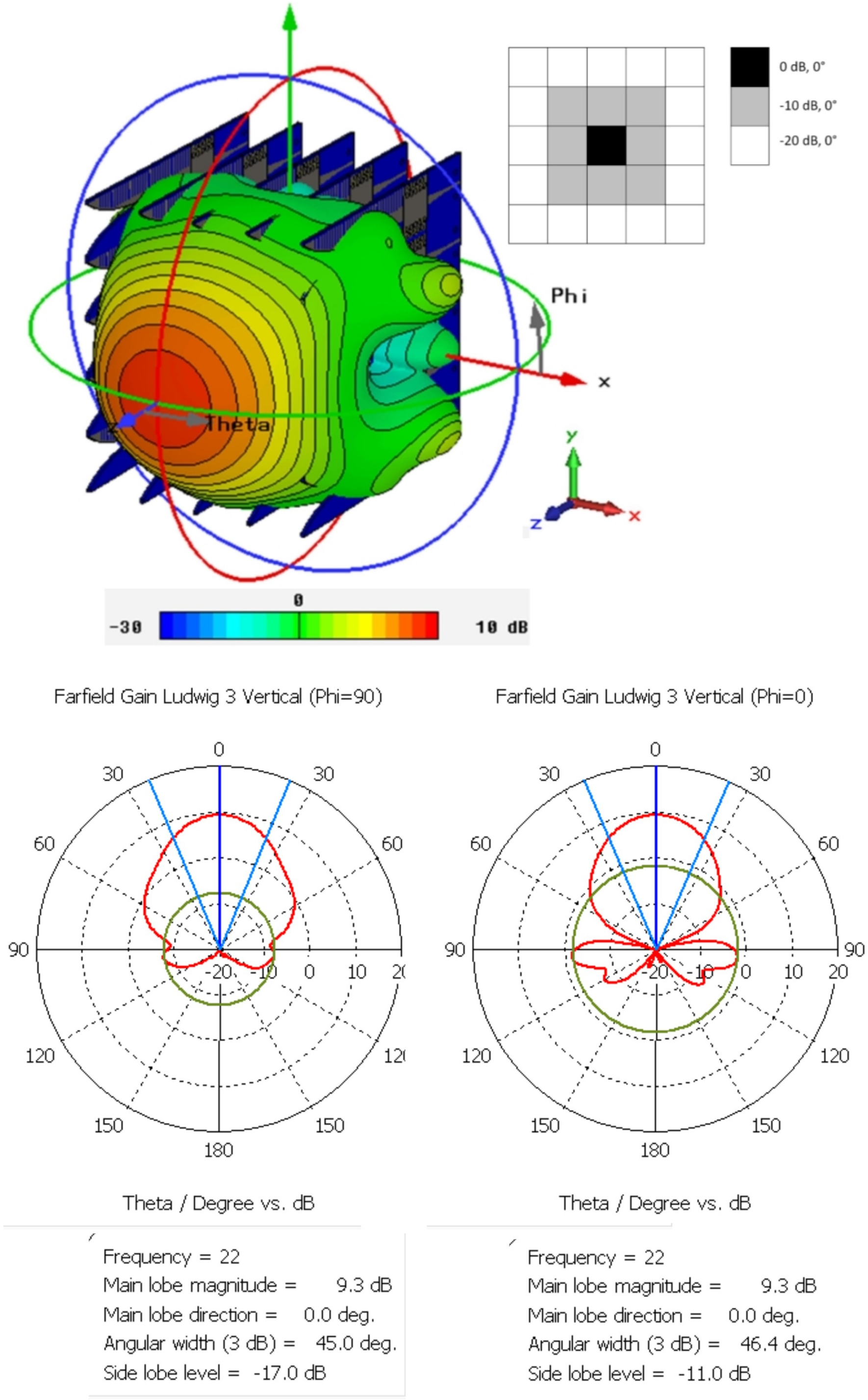

Farfield Gain Ludwig 3 Vertical (Phi=90)

Theta / Degree vs. dB

```
Frequency = 22
Main lobe magnitude =      9.3 dB
Main lobe direction =    0.0 deg.
Angular width (3 dB) =   45.0 deg.
Side lobe level =  -17.0 dB
```

Farfield Gain Ludwig 3 Vertical (Phi=0)

Theta / Degree vs. dB

```
Frequency = 22
Main lobe magnitude =      9.3 dB
Main lobe direction =    0.0 deg.
Angular width (3 dB) =   46.4 deg.
Side lobe level =  -11.0 dB
```

Figure 5.18: Gain of synthesized beam (dB) of 5 x 5 array with element amplitude and phase weightings: centre element: $1.0\angle 0°$, inner ring: $0.1\angle 0°$, outer ring: $0.01\angle 0°$. Contours represent 1 dB steps. The physical array structure demonstrates orientation. E-plane ($\phi = 90°$) and H-plane ($\phi = 0°$) polar cuts including HPBW and maximum side lobe levels. 22 GHz.

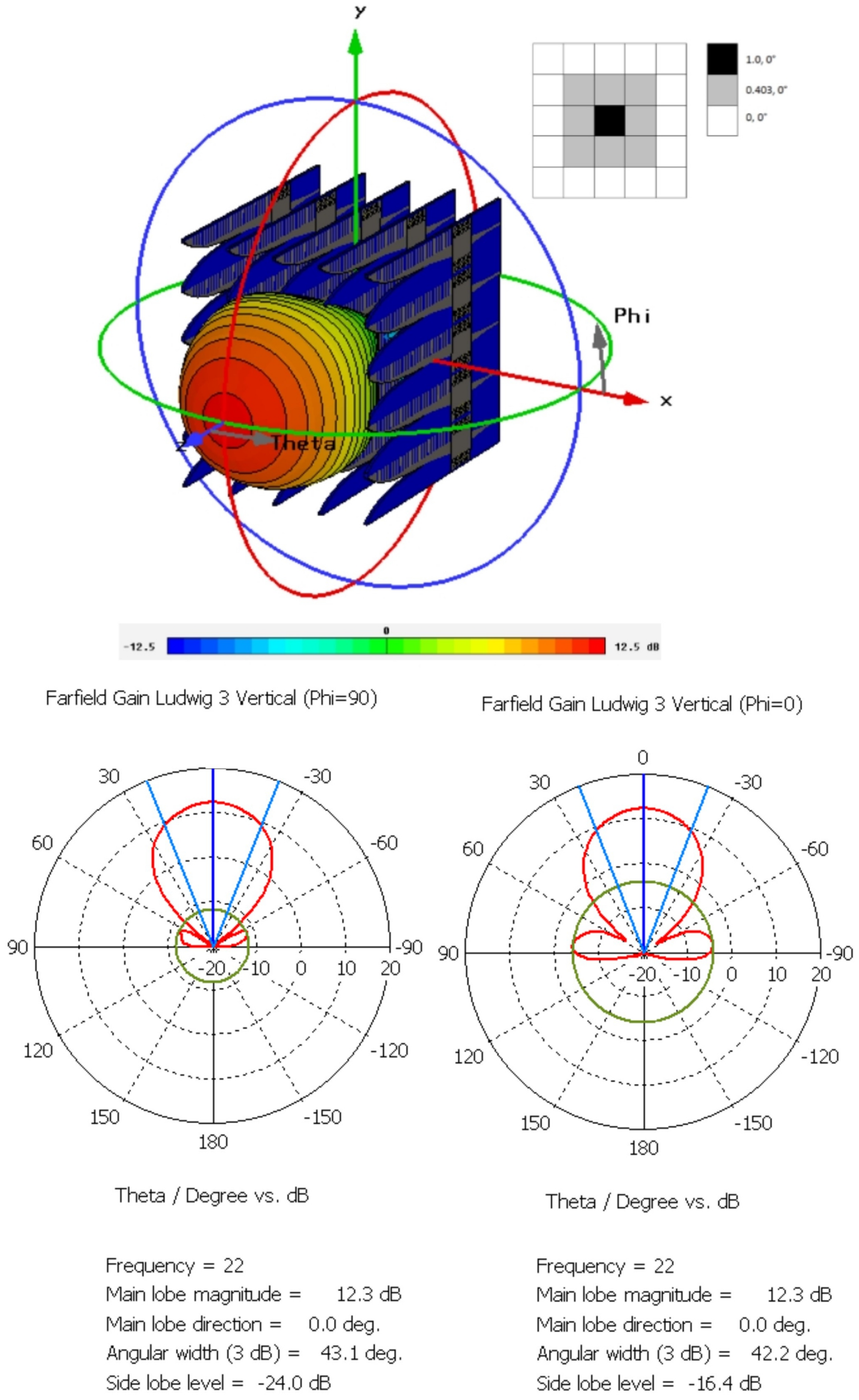

```
Frequency = 22
Main lobe magnitude =     12.3 dB
Main lobe direction =    0.0 deg.
Angular width (3 dB) =   43.1 deg.
Side lobe level =  -24.0 dB
```

```
Frequency = 22
Main lobe magnitude =     12.3 dB
Main lobe direction =    0.0 deg.
Angular width (3 dB) =   42.2 deg.
Side lobe level =  -16.4 dB
```

Figure 5.19: Gain of synthesized beam (dB) of 5 x 5 array with optimized element amplitude and phase weightings: centre element: $1.0\angle 0^\circ$, inner ring: $0.403\angle 0^\circ$, outer ring: $0\angle 0^\circ$. Contours represent 1 dB steps. E-plane ($\phi = 90^\circ$) and H-plane ($\phi = 0^\circ$) polar cuts including HPBW and maximum side lobe levels. The physical array structure demonstrates orientation. 22 GHz.

Chapter 6

Conclusions

Small moves Ellie, small moves.
- Contact

Astronomical surveys are demanding more throughput from telescope receivers. Currently, microwave telescopes with mature cryogenic single pixel receivers are upgrading to multi-pixel receivers by replacing conventional feed horns with PAFs to increase the field of view and, thus, imaging speeds. This step in astronomy instrumentation has been taken by only a few research laboratories world-wide and primarily in L-band (0.7 - 1.5 GHz). A K-band (18 - 26 GHz) 5 x 5 modular PAF imaging system including planar TSA elements with SIW feed, cryogenic low-noise amplifier block and mixer assembly for use with a 10 m reflector paraboloid has been designed, and a single blade 1 x 5 PAF system has been built and tested, demonstrating the feasibility of higher frequency antenna and receiving systems. The performance is evaluated using system noise temperature and optical throughput via survey speed rates and imaged area. The primary KPAF 5 x 5 module is proven and future designs will incorporate the modularity to create a 10 x 10 or 15 x 15 element system. A 40 beam single polarization cryogenic PAF can exceed the performance of a cryogenic SPF by a factor of 18.

Positive attributes of the KPAF system are that it is a successful technology demonstrator for K-band PAFs demonstrating a significant increase in field of view, and the planar tapered slot antenna design is economical and quick to manufacture. Some criticisms are the inconsistent SSST calibration circuit performance due to the delicate antenna substrate flexing and the non-zero insertion force mini-SMP coaxial connectors.

Recommendations for future KPAF improvements are the following:

- Increase the number of antenna-receiver elements to achieve a satisfactory survey speed increase for systems with non-cryogenic components.
- If scaling the system to higher frequencies, remove or modify corrugations and other small features on antenna element for manufacturing reliability.
- Replace Rogers 6010LM substrate with a more robust material as mentioned above.
- Use a feed configuration that can incorporate curved focal plane arrays to reduce focusing errors [70].
- Cryogenically cool the antenna and amplifier. This would involve a dewar design and a microwave-permeable membrane that can withstand the high pressure differential between the air and the near-perfect vacuum inside.
- Find a zero insertion force microwave connector for the antenna-amplifier connection to increase mechanical stability and SSST calibration repeatability and accuracy.
- Integrate the antenna, amplifier and possibly the mixer to reduce system noise temperature thus increasing the survey speed.

Bibliography

[1] M. Morgan and J.R.Fisher, "Next generation radio astronomy receiver systems," 2010. arxiv.org, last accessed Mar 31, 2014.

[2] K. F. Warnick, D. Carter, T. Webb, J. Landon, M. Elmer, and B. D. Jeffs, "Design and characterization of an active impedance matched low-noise phased array feed," *IEEE Trans. Antennas Propagat.*, vol. 59, pp. 1876–1885, June 2011.

[3] R. Maaskant, M. Ivashina, O. Iupikov, E. A. Redkina, S. Kasturi, and D. H. Schaubert, "Analysis of large microstrip-fed tapered slot antenna arrays by combining electrodynamic and quasi-static field models," *IEEE Trans. Antennas Propagat.*, vol. 59, pp. 1798–1807, June 2011.

[4] B. Veidt, G. J. Hovey, T. Burgess, R. J. Smegal, R. Messing, A. G. Willis, A. D. Gray, and P. E. Dewdney, "Demonstration of a dual-polarized phased-array feed," *IEEE Trans. Antennas Propagat.*, vol. 59, pp. 2047–2057, June 2011.

[5] R. Sarkis, C. Craeye, and B. Veidt, "Thick Vivaldi antenna for focal plane applications," in *IEEE AP-S Int. Symp. Dig.*, (Spokane, WA), pp. 1988–1991, July 2011.

[6] D. R. DeBoer, R. G. Gough, J. D. Bunton, T. J. Cornwell, R. J. Beresford, S. Johnston, I. J. Feain, A. E. Schinckel, C. A. Jackson, M. J. Kesteven, A. Chippendale, G. A. Hampson, J. D. OSullivan, S. G. Hay, C. E. Jacka, T. W. Sweetnam, M. C. Storey, L. Ball, and B. J. Boyle, "Australian SKA pathfinder: a high-dynamic range wide-field of view survey telescope," *Proceedings of the IEEE*, vol. 97, pp. 1507–1521, August 2009.

[7] G. Cortes-Medellin, A. Vishwas, S. C. Parshley, and D. B. Campbell, "Fully cryogenic phased array prototype camera for the Arecibo radio telescope," in

Proc. SPIE 9147, Ground-based and Airborne Instrumentation for Astronomy V, (Montreal, Quebec, Canada), pp. 91479Q–91479Q–7, June 22-26, 2014.

[8] S. Kim and G. Rebeiz, "A low power silicon BiCMOS phased array receiver for 76-84 GHz radar and communication systems," *IEEE J. Solid-State Circuits*, vol. 47, pp. 359–367, February 2012.

[9] K. Koh and G. Rebeiz, "An X- and Ku-band 8-element phased array receiver in 0.18 μm SiGe BiCMOS technology," *IEEE J. Solid-State Circuits*, vol. 43, pp. 1360–1371, June 2008.

[10] I. Wood, D. Dousset, J. Bornemann, and S. Claude, "Linear tapered slot antenna with substrate integrated waveguide feed," in *IEEE AP-S Int. Symp. Dig.*, (Honolulu, USA), pp. 4761–4764, June 2007.

[11] F. Taringou, D. Dousset, J. Bornemann, and K. Wu, "Broadband CPW feed for millimeter-wave SIW-based antipodal linearly tapered slot antennas," *IEEE Trans. Antennas Propagat.*, vol. 61, pp. 1756–1761, April 2013.

[12] D. Deslandes, "Design equations for tapered microstrip-to-substrate integrated waveguide transitions," in *IEEE MTT-S Int. Microwave Symp. Dig.*, (Anaheim, CA), pp. 704–707, May 2010.

[13] D. Henke, 2014. private communication.

[14] S. Claude, 2014. private communication.

[15] J. D. Kraus, *Radio Astronomy.* Cygnus Quasar Books, 1986.

[16] P. Ho and C. Townes, "Interstellar ammonia," *Annual Review of Astronomy and Astrophysics*, vol. 21, pp. 239–270, 1983.

[17] D. Shepherd, C. Chandler, B. Cotton, R. Perley, S. Randall, and A. Remijana, "New insights into astrophysical jets with the Atacama large millimeter array and the Karl G. Jansky very large array," *High Energy Density Physics*, vol. 9, no. 1, pp. 26–31, 2013.

[18] J. D. Francesco, 2013. private communication.

[19] K. Jansky, "Directional studies of atmospherics at high frequencies," *Proc. IRE*, vol. 20, pp. 1920–1932, 1932.

[20] K. Jansky, "Electrical disturbances apparently of extraterrestrial origin," *Proc. IRE*, vol. 21, pp. 1387–1398, 1933.

[21] J. D. Kraus, *Antennas.* McGraw-Hill, 2011.

[22] D. Hayman, T. Bird, K. Esselle, and P. Hall, "Encircled power study of focal plane field for estimating focal plane array size," in *IEEE AP-S Int. Symp. Dig.*, vol. 3A, (Washington, USA), pp. 371–374, July 2005.

[23] P. Goldsmith, C.-T. Hsieh, G. Huguenin, J. Kapitzky, and E. Moore, "Focal plane imaging systems for millimeter wavelengths," *IEEE Trans. Microwave Theory Tech.*, vol. 41, pp. 1664–1675, October 1993.

[24] J. Murphy and R. Padman, "Focal-plane and aperture-plane heterodyne array receivers for millimeter-wave radioastronomy – a comparison," *International Journal of Infrared and Millimeter Waves*, vol. 9, no. 8, pp. 667–704, 1988.

[25] Z.-L. Zhou, L. Li, J.-S. Hong, and B.-Z. Wang, "A novel harmonic suppression antenna with both compact size and wide bandwidth," *ACES Journal*, vol. 27, pp. 435–440, May 2012.

[26] B. Veidt, "Memo 71: Focal-plane array architectures: Horn clusters vs. phased-array techniques," 2006. SKA Memo Series.

[27] A. W. Rudge and D. Davies, "Electronically controlled primary feed for profile-error compensation of large parabolic reflectors," *Proceedings of the IEE*, vol. 117, pp. 351–358, February 1970.

[28] W. T. Smith and W. L. Stutzman, "A pattern synthesis technique for array feeds to improve radiation performance of large distorted reflector antennas," *IEEE Trans. Antennas Propagat.*, vol. 40, pp. 57–62, January 1992.

[29] P. Clarricoats, S. Tun, and R. Brown, "Performance of offset reflector antennas with array feeds," *IEE Proceedings H, Microwaves, Optics and Antennas*, vol. 131, pp. 172–178, June 1984.

[30] L. Belostotski and J. W. Haslett, "Sub-0.2 dB noise figure wideband room-temperature CMOS LNA with non-50 ohm signal-source impedance," *IEEE J. Solid-State Circuits*, vol. 42, pp. 2492–2502, November 2007.

[31] R. Maaskant, R. Mittra, and A. Tijhuis, “Fast analysis of large antenna arrays using the characteristic basis function method and the adaptive cross approximation algorithm,” *IEEE Trans. Antennas Propagat.*, vol. 56, pp. 3440–3451, Nov. 2008.

[32] W. Yu, X. Yang, Y. Lin, L. Ma, T. Su, N. Huang, R. Mittra, R. Maaskant, y. Lu, Q. Che, R. Lu, and Z. Su, “A new direction in computational electromagnetics: Solving large problems using the parallel FDTD on the BluGene/L supercomputer providing teraflop-level performance,” *IEEE Antennas and Propagat. Mag.*, vol. 50, pp. 26–44, April 2008.

[33] W. van Cappellen and L. Bakker, “APERTIF: phased array feeds for the Westerbork Synthesis Radio Telescope,” in *IEEE Int. Symp. Phased Array Systems Tech.*, (Waltham, MA), pp. 640–647, October 2010.

[34] D. B. Hayman, T. S. Bird, K. P. Esselle, and P. J. Hall, “Experimental demonstration of focal plane array beamforming in a prototype radiotelescope,” *IEEE Trans. Antennas Propagat.*, vol. 58, pp. 1922–1934, June 2010.

[35] P. E. Dewdney, P. J. Hall, R. T. Schilizzi, and T. Lazio, “The square kilometer array,” *Proceedings of the IEEE*, vol. 97, pp. 1482–1496, August 2009.

[36] B.-K. Tan, G. Yassin, S. Withington, and D. Goldie, “Microstrip Yagi antenna for ALMA band 11 receiver,” *International Journal of Terahertz Science and Technology*, p. accepted for publication, 2013.

[37] B. Veidt, T. Burgess, K. Yeung, S. Claude, I. Wevers, M. Halman, P. Niranjanan, C. Yao, A. Jew, D. Henke, and A. Willis, “Noise performance of thick Vivaldi elements with embedded low-noise amplifiers,” in *to be presented at General Assembly and Scientific Symposium, URSI*, (Beijing, China), August 2014.

[38] E. Woestenburg, L. Bakker, and M. Ivashina, “Experimental results for the sensitivity of a low noise aperture array tile for the SKA,” *IEEE Trans. Antennas Propagat.*, vol. 60, pp. 915–921, February 2012.

[39] J. Cordes, “Memo 109: Survey metrics,” 2007. SKA Memo Series.

[40] D. Jones, “Memo 66: Relative sensitivities of the ska and other current or near-future instruments,” 2005. SKA Memo Series.

[41] S. Johnston and A. Gray, “Memo 72: Surveys with the xNTD and CLAR,” 2006. SKA Memo Series.

[42] “AN 154 S-parameter design,” 2006. Agilent Technologies Application Note.

[43] R. Janaswamy and D. H. Schaubert, “Analysis of the tapered slot antenna,” *IEEE Trans. Antennas Propagat.*, vol. 35, pp. 1058–1065, September 1987.

[44] K. Yngvesson, D. Schaubert, T. Korzeniowski, E. Kollberg, T. Thungren, and J. Johansson, “Endfire tapered slot antennas on dielectric substrates,” *IEEE Trans. Antennas Propagat.*, vol. 33, pp. 1392–1400, December 1985.

[45] R. Janaswamy, *Radiation pattern analysis of the tapered slot antenna.* PhD thesis, University of Massachusetts, MA, 1986.

[46] K. Yngvesson, T. Korzeniowski, Y.-S. Kim, E. Kollberg, and J. Johansson, “The tapered slot antenna - a new integrated element for millimeter wave applications,” *IEEE Trans. Microwave Theory Tech.*, vol. 37, pp. 365–374, February 1989.

[47] T. L. Korzeniowski, *A 94 GHz imaging array antenna using slot-line radiators.* PhD thesis, University of Massachusetts, MA, 1985.

[48] M. Elsallal and J. Mather, “An ultra-thin, decade (10:10) bandwidth, modular ”BAVA” array with low cross-polarization,” in *IEEE AP-S Int. Symp. Dig.*, (Spokane, WA), pp. 1980–1983, July 2011.

[49] S. Sugawara, Y. Maita, K. Adachi, K. Mori, and K. Mizuno, “A mm-wave tapered slot antenna with improved radiation pattern,” in *IEEE MTT-S Int. Microwave Symp. Dig.*, (Denver, CO), pp. 959–962, June 1997.

[50] D. M. Pozar, *Microwave Engineering.* 3rd ed., John Wiley and Sons, 2005.

[51] J. Rizk and G. Rebeiz, “Millimeter-wave fermi tapered slot antennas on micromachines silicon substrates,” *IEEE Trans. Antennas Propagat.*, vol. 50, pp. 379–383, March 2002.

[52] S. Sugawara, Y. Maita, K. Adachi, K. Mori, and K. Mizuno, “Characteristics of a mm-wave tapered slot antenna with corrugated edges,” in *IEEE MTT-S Int. Microwave Symp. Dig.*, (Baltimore, MD), pp. 533–536, June 1998.

[53] I. R. T.G. Lim, H.N. Ang and B. Weiss, "Tapered slot antenna using photonic bandgap structure to reduce substrate effects," *Electronics Letters*, vol. 41, pp. 393–394, March 2005.

[54] K. Sawaya, H. Sato, Y. Wagatsuma, and K. Mizuno, "Broadband Fermi antenna and its application to mm-wave imaging," in *Proc. 2nd Eur. Conf. Antennas Propag. (EuCAP)*, (Edinburgh, U.K.), pp. 1–6, November 2007.

[55] J. Mandeep and M. Nicholas, "Design an X-band Vivaldi antenna." Microwaves and RF, July 2008, mwrf.com.

[56] N. Fourikis, N. Lioutas, and N. Shuley, "Parametric study of the co- and crosspolarisation characteristics of tapered planar and anitpodal slotline antennas," *IEE Proceedings-H*, vol. 140, pp. 17–22, February 1993.

[57] D. Deslandes and K. Wu, "Integrated microstrip and rectangular waveguide in planar form," *IEEE Microwave Wireless Comp. Lett.*, vol. 11, pp. 68–70, February 2001.

[58] F. Taringou and J. Bornemann, "New substrate-integrated to coplanar waveguide transition," in *Proc. 41st European Microwave Conf.*, (Manchester, UK), pp. 428–431, October 2011.

[59] M. Sun, X. Qing, and Z. N. Chen, "60-GHz antipodal Fermi antenna on PCB," in *Proc. 5th Eur. Conf. Antennas Propag. (EuCAP)*, (Rome), pp. 3109–3112, April 2011.

[60] J. Bai, S. Shi, and D. Prather, "Modified compact antipodal Vivaldi antenna for 4-50 GHz UWB application," *IEEE Trans. Microwave Theory Tech.*, vol. 59, pp. 1051–1057, April 2011.

[61] H. Sato, K. Sawaya, N. Arai, Y. Wagatsuma, and K. Mizuno, "Broadband FDTD analysis of Fermi antenna with narrow width substrate," in *IEEE AP-S Int. Symp. Dig.*, (Columbus, OH), pp. 261–264, June 2003.

[62] "AN 1287-3 Applying error correction to network analyzer measurements," 2006. Agilent Technologies Application Note.

[63] A. Company, "VectorStar MS4640A series microwave vector network analyzers calibration and measurement guide," 2012.

[64] “IEEE recommended practice for near-field antenna measurements,” 2012. IEEE Antennas and Propagations Society, IEEE Std 1720-2012.

[65] J. Fisher and R. Bradley, “Full-sampling focal plane arrays,” in *Imaging at Radio through Submillimeter Wavelengths, Astron. Soc. Pac. Conf. J.* (G. Mangum and S. Radford, eds.), vol. 217, pp. 11–18, 2000.

[66] H. Minnett and B. Thomas, “Fields in the image space of symmetrical focusing reflectors,” *Proc. IEE*, vol. 115, pp. 1419–1430, October 1968.

[67] A. Ludwig, “The definition of cross-polarisation,” *IEEE Trans. Antennas Propagat.*, vol. 21, pp. 116–119, January 1973.

[68] “GRASP user’s manual,” 2012. GRASP version 10.0.1.

[69] C. A. Balanis, *Antenna Theory: Analysis and Design.* 3rd ed., John Wiley and Sons, 2005.

[70] D. Dumas, M. Fendler, N. Baier, J. Primot, and E. le Coarer, “Curved focal plane detector array for wide field cameras,” *Applied optics*, vol. 51, pp. 5419–5424, August 2013.

Appendix A

Molecular Ammonia (NH_3) Transitions

The ammonia molecule and transitions between 23.6 and 25.8 GHz [16, 18] are shown in Table A.1. The second column is the rest frequency in GHz to 10 kHz resolution and the error in the frequency measurement. The third column is the inversion number. The fourth column is the resolved quantum numbers which gives information about the energy level changes and the hyperfine interactions within the ammonia molecule.

No.	**Freq. (error) [GHz]**	**Inversions**	**Hyperfine Transitions**
1	23.69293 (2.0E-7)	1(1)	F1=1-0, F=1/2-1/2
2	23.69297 (1.0E-7)	1(1)	F1=1-0, F=3/2-1/2
3	23.69387 (1.0E-7)	1(1)	F1=1-2, F=1/2-3/2
4	23.69391 (1.0E-7)	1(1)	F1=2-2, F=3/2-5/2
5	23.69391 (1.0E-7)	1(1)	F1=1-2, F=3/2-3/2
6	23.69446 (1.0E-7)	1(1)	F1=1-1, F=1/2-1/2
7	23.69447 (1.0E-5)	1(1)	F1=1-1, F=1/2-3/2
8	23.69447 (1.0E-7)	1(1)	F1=2-2, F=3/2-5/2
9	23.69448 (1.0E-7)	1(1)	F1=2-2, F=3/2-3/2
10	23.69450 (1.0E-7)	1(1)	F1=1-1, F=3/2-1/2
11	23.69451 (1.0E-6)	1(1)	F1=2-2, F=5/2-5/2
12	23.69451 (1.0E-7)	1(1)	F1=1-1, F=3/2-3/2
13	23.69452 (1.0E-7)	1(1)	F1=2-2, F=5/2-3/2
14	23.69507 (1.0E-7)	1(1)	F1=2-1, F=3/2-1/2
15	23.69508 (1.0E-7)	1(1)	F1=2-1, F=3/2-3/2
16	23.69511 (1.0E-7)	1(1)	F1=2-1, F=5/2-3/2
17	23.69603 (2.0E-7)	1(1)	F1=0-1, F=1/2-1/2
18	23.69604 (2.0E-7)	1(1)	F1=0-1, F=1/2-3/2
19	23.72058 (5.0E-6)	2(2)	F1=1-2
20	23.72134 (5.0E-6)	2(2)	F1=3-2
21	23.72263 (5.0E-7)	2(2)	F1=2-2
22	23.72263 (1.0E-7)	2(2)	F1=3-3
23	23.72263 (5.0E-7)	2(2)	F1=1-1
24	23.72393 (5.0E-6)	2(2)	F1=2-3
25	23.72469 (5.0E-6)	2(2)	F1=2-1
26	23.86781 (5.0E-6)	3(3)	F1=2-3
27	23.86845 (5.0E-5)	3(3)	F1=4-3
28	23.87013 (5.0E-7)	3(3)	F1=3-3
29	23.87013 (1.0E-7)	3(3)	F1=4-4
30	23.87013 (5.0E-7)	3(3)	F1=2-2
31	23.87181 (5.0E-6)	3(3)	F1=3-4
32	23.87245 (5.0E-6)	3(3)	F1=3-2
33	24.13942 (1.0E-7)	4(4)	
34	24.20529 (5.0E-6)	10(9)	
35	24.53299 (1.0E-7)	5(5)	
36	25.05603 (5.0E-6)	6(6)	
37	25.71518 (5.0E-6)	7(7)	

Table A.1: Molecular Ammonia Transitions from 23.6 - 25.8 GHz.

Appendix B

Rogers RT/Duroid 6010 Datasheet

ROGERS
CORPORATION
Advanced Circuit Materials

Advanced Circuit Materials Division
100 S. Roosevelt Avenue
Chandler, AZ 85226
Tel: 480-961-1382, Fax: 480-961-4533
www.rogerscorp.com

Data Sheet
1.6000

RT/duroid® 6006/6010LM High Frequency Laminates

Features
- High dielectric constant for circuit size reduction.
- Low loss. Ideal for operating at X-band or below.
- Low Z-axis expansion for RT/duroid 6010LM. Provides reliable plated through holes in multilayer boards.
- Low moisture absorption for RT/duroid 6010LM. Reduces effects of moisture on electrical loss.
- Tight ε_r and thickness control for repeatable circuit performance.
Some Typical Applications
- Space Saving Circuitry
- Patch Antennas
- Satellite Communications Systems
- Power Amplifiers
- Aircraft Collision Avoidance Systems
- Ground Radar Warning Systems

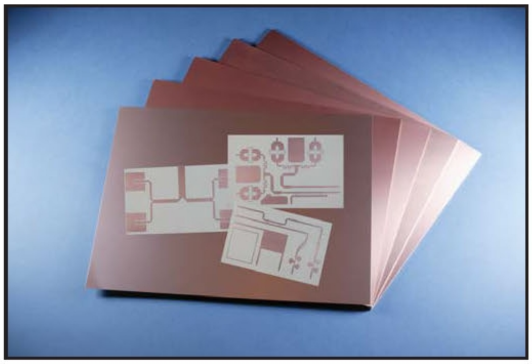

RT/duroid® 6006/6010LM microwave laminates are ceramic-PTFE composites designed for electronic and microwave circuit applications requiring a high dielectric constant. RT/duroid 6006 laminate is available with a dielectric constant value of 6.15 and RT/duroid 6010LM laminate has a dielectric constant of 10.2.

RT/duroid 6006/6010LM microwave laminates feature ease of fabrication and stability in use. They have tight dielectric constant and thickness control, low moisture absorption, and good thermal mechanical stability.

RT/duroid 6006/6010LM laminates are supplied clad both sides with ¼ oz. to 2 oz./ft² (8.5 to 70 µm) electrodeposited copper foil. Cladding with rolled copper foil is also available. Thick aluminum, brass, or copper plate on one side may be specified.

Standard tolerance dielectric thicknesses of 0.010", 0.025", 0.050", 0.075", and 0.100" (0.254, 0.635, 1.270, 1.905, 2.54 mm) are available. When ordering RT/duroid 6006 and RT/duroid 6010LM laminates, it is important to specify dielectric thickness, electrodeposited or rolled, and weight of copper foil required.

Typical Values **RT/duroid 6006, RT/duroid 6010LM Laminates**

Property	Typical Value [2]		Direction	Units [1]	Condition	Test Method
	RT/duroid 6006	RT/duroid 6010.2LM				
[3]Dielectric Constant ε_r *Process*	6.15± 0.15	10.2 ± 0.25	Z		10 GHz 23°C	IPC-TM-650 2.5.5.5 Clamped stripline
[4]Dielectric Constant ε_r *Design*	6.45	10.9	Z		8 GHz - 40 GHz	Differential Phase Length Method
Dissipation Factor, tan δ	0.0027	0.0023	Z		10 GHz/A	IPC-TM-650 2.5.5.5
Thermal Coefficient of ε_r	-410	-425	Z	ppm/°C	-50 to 170°C	IPC-TM-650 2.5.5.5
Surface Resistivity	7X10^{7}	5X10^{6}		Mohm	A	IPC 2.5.17.1
Volume Resistivity	2X10^{7}	5X10^{5}		Mohm•cm	A	IPC 2.5.17.1
Youngs' Modulus						ASTM D638 (0.1/min. strain rate)
under tension	627 (91) 517 (75)	931 (135) 559 (81)	X Y	MPa (kpsi)	A	
ultimate stress	20 (2.8) 17 (2.5)	17 (2.4) 13 (1.9)	X Y	MPa (kpsi)	A	
ultimate strain	12 to 13 4 to 6	9 to 15 7 to 14	X Y	%	A	
Youngs' Modulus						ASTM D695 (0.05/min. strain rate)
under compression	1069 (155)	2144 (311)	Z	MPa (kpsi)	A	
ultimate stress	54 (7.9)	47 (6.9)	Z	MPa (kpsi)	A	
ultimate strain	33	25	Z	%		
Flexural Modulus	2634 (382) 1951 (283)	4364 (633) 3751 (544)	X	MPa (kpsi)	A	ASTM D790
ultimate stress	38 (5.5)	36 (5.2) 32 (4.4)	X Y	MPa (kpsi)	A	
Deformation under load	0.33 2.10	0.26 1.37	Z Z	%	24 hr/ 50°C/7MPa 24 hr/150°C/7MPa	ASTM D621
Moisture Absorption	0.05	0.01		%	D48/50°C, 0.050" (1.27mm) thick	IPC-TM-650, 2.6.2.1
Density	2.7	3.1				ASTM D792
Thermal Conductivity	0.49	0.86		W/m/°K	80°C	ASTM C518
Thermal Expansion	47 34, 117	24 24,47	X Y,Z	ppm/°C	0 to 100°C	ASTM 3386 (5K/min)
Td	500	500		°C TGA		ASTM D3850
Specific Heat	0.97 (0.231)	1.00 (0.239)		J/g/K (BTU/lb/°F)		Calculated
Copper Peel	14.3 (2.5)	12.3 (2.1)		pli (N/mm)	after solder float	IPC-TM-650 2.4.8
Flammability Rating	V-0	V-0				UL94
Lead-Free Process Compatible	Yes	Yes				

[1] SI unit given first with other frequently used units in parentheses.
[2] References: APR4022.33 DJS 4019.27-32, Internal TR 2610. Tests were at 23°C unless otherwise noted.
[3] Dielectric constant is based on .025 dielectric thickness, one ounce electrodeposited copper on two sides.
[4] The design Dk is an average number from several different tested lots of material and on the most common thickness/s. If more detailed information is required, please contact Rogers Corporation. Refer to Rogers' technical paper "Dielectric Properties of High Frequency Materials" available at http://www.rogerscorp.com/acm.

Typical values are a representation of an average value for the population of the property. For specification values contact Rogers Corporation.

STANDARD THICKNESS:	STANDARD PANEL SIZE:	STANDARD COPPER CLADDING:
0.005" (0.127mm) 0.010" (0.254mm) 0.025" (0.635mm) 0.050" (1.27mm) 0.075" (1.90mm) 0.100" (2.50mm)	10" X 10" (254 X 254mm) 10" X 20" (254 X 508mm) 20" X 20" (508 X 508mm) *18" X 12" (457 X 305 mm) *18" X 24" (457 X 610 mm) (*note: the above 2 panel sizes are not available in the 0.005" (0.127mm) and 0.010" (0.254mm) thicknesses)	¼ oz. (8.5 µm) electrodeposited copper foil. ½ oz. (18 µm), 1 oz. (35µm), 2 oz. (70µm) electrodeposited and rolled copper foil. Heavy metal claddings are available. Contact Rogers' Customer Service.

Revised 03/2011 0938-0111-.5CC **Publication: #92-105**

Appendix C

Connectors and Cables

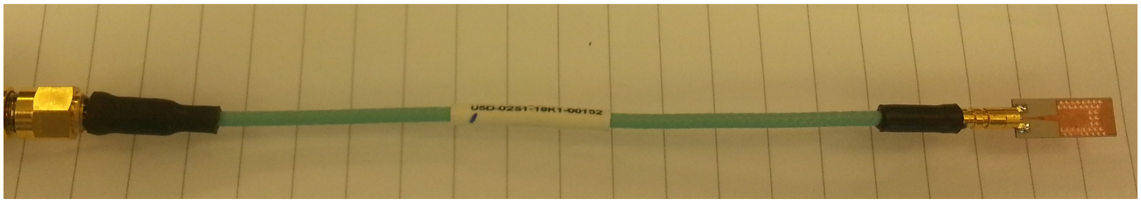

Figure C.1: Rosenberger cable and right angle plug soldered onto calibration circuit.

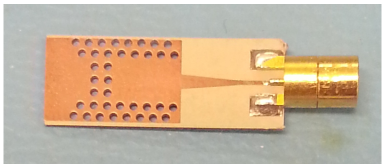

Figure C.2: miniSMP right angle plug soldered onto calibration circuit.

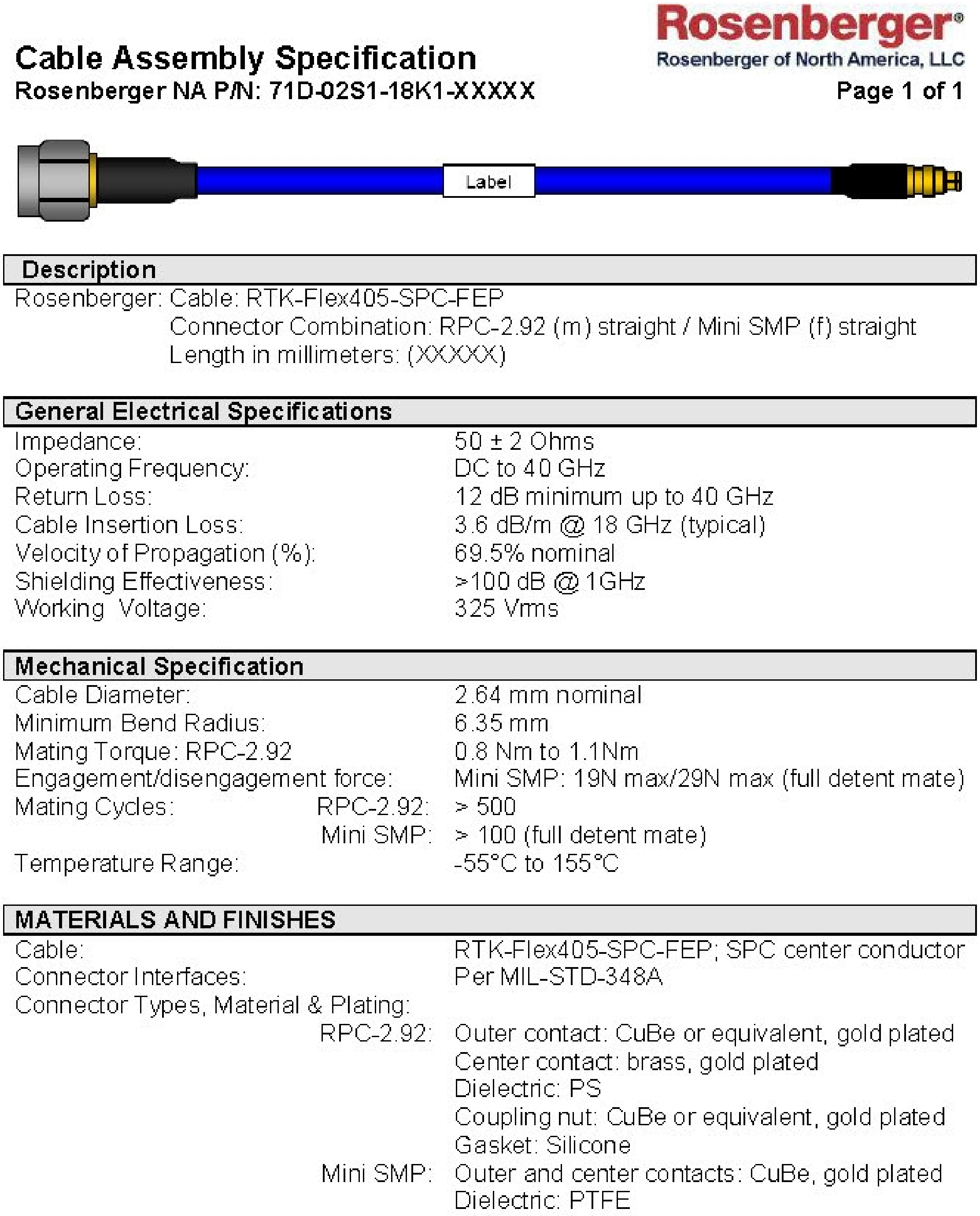

Rosenberger®
Rosenberger of North America, LLC
Page 1 of 1

Cable Assembly Specification
Rosenberger NA P/N: 71D-02S1-18K1-XXXXX

Description

Rosenberger: Cable: RTK-Flex405-SPC-FEP
Connector Combination: RPC-2.92 (m) straight / Mini SMP (f) straight
Length in millimeters: (XXXXX)

General Electrical Specifications

Impedance:	50 ± 2 Ohms
Operating Frequency:	DC to 40 GHz
Return Loss:	12 dB minimum up to 40 GHz
Cable Insertion Loss:	3.6 dB/m @ 18 GHz (typical)
Velocity of Propagation (%):	69.5% nominal
Shielding Effectiveness:	>100 dB @ 1GHz
Working Voltage:	325 Vrms

Mechanical Specification

Cable Diameter:		2.64 mm nominal
Minimum Bend Radius:		6.35 mm
Mating Torque: RPC-2.92		0.8 Nm to 1.1Nm
Engagement/disengagement force:		Mini SMP: 19N max/29N max (full detent mate)
Mating Cycles:	RPC-2.92:	> 500
	Mini SMP:	> 100 (full detent mate)
Temperature Range:		-55°C to 155°C

MATERIALS AND FINISHES

Cable:		RTK-Flex405-SPC-FEP; SPC center conductor
Connector Interfaces:		Per MIL-STD-348A
Connector Types, Material & Plating:		
	RPC-2.92:	Outer contact: CuBe or equivalent, gold plated Center contact: brass, gold plated Dielectric: PS Coupling nut: CuBe or equivalent, gold plated Gasket: Silicone
	Mini SMP:	Outer and center contacts: CuBe, gold plated Dielectric: PTFE

Figure C.3: Rosenberger P/N 71D-02S1-18K1 cable assembly datasheet

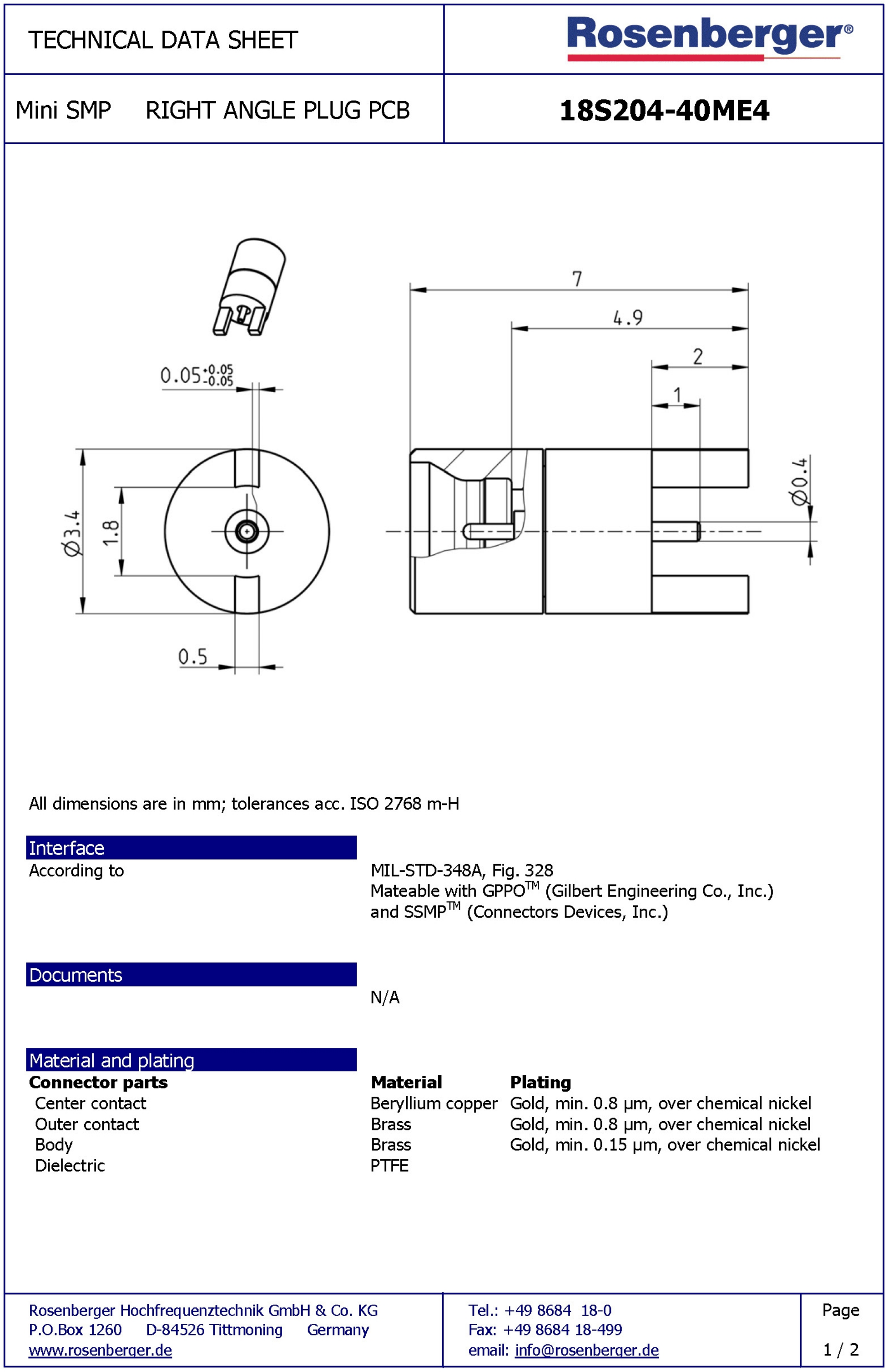

TECHNICAL DATA SHEET

Rosenberger®

Mini SMP RIGHT ANGLE PLUG PCB

18S204-40ME4

All dimensions are in mm; tolerances acc. ISO 2768 m-H

Interface

According to	MIL-STD-348A, Fig. 328 Mateable with GPPO^{TM} (Gilbert Engineering Co., Inc.) and SSMP^{TM} (Connectors Devices, Inc.)

Documents

N/A

Material and plating

Connector parts	**Material**	**Plating**
Center contact	Beryllium copper	Gold, min. 0.8 µm, over chemical nickel
Outer contact	Brass	Gold, min. 0.8 µm, over chemical nickel
Body	Brass	Gold, min. 0.15 µm, over chemical nickel
Dielectric	PTFE	

Rosenberger Hochfrequenztechnik GmbH & Co. KG
P.O.Box 1260 D-84526 Tittmoning Germany
www.rosenberger.de

Tel.: +49 8684 18-0
Fax: +49 8684 18-499
email: info@rosenberger.de

Page
1 / 2

Figure C.4: Rosenberger P/N 18S204-40ME4: Right angle plug

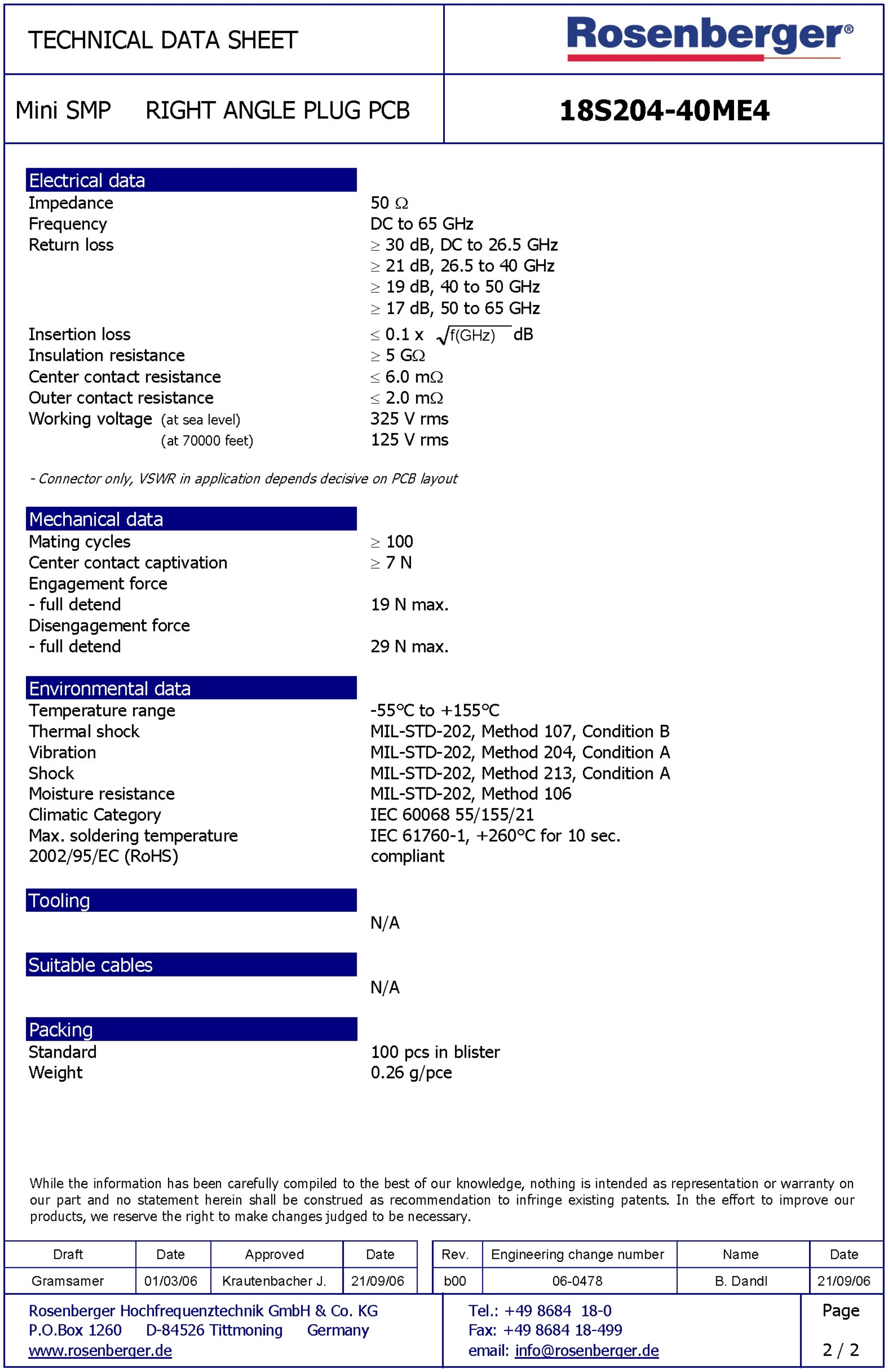

TECHNICAL DATA SHEET

Rosenberger®

Mini SMP RIGHT ANGLE PLUG PCB

18S204-40ME4

Electrical data

Impedance	50 Ω
Frequency	DC to 65 GHz
Return loss	≥ 30 dB, DC to 26.5 GHz ≥ 21 dB, 26.5 to 40 GHz ≥ 19 dB, 40 to 50 GHz ≥ 17 dB, 50 to 65 GHz
Insertion loss	≤ 0.1 x $\sqrt{f(GHz)}$ dB
Insulation resistance	≥ 5 GΩ
Center contact resistance	≤ 6.0 mΩ
Outer contact resistance	≤ 2.0 mΩ
Working voltage (at sea level)	325 V rms
(at 70000 feet)	125 V rms

- Connector only, VSWR in application depends decisive on PCB layout

Mechanical data

Mating cycles	≥ 100
Center contact captivation	≥ 7 N
Engagement force	
- full detend	19 N max.
Disengagement force	
- full detend	29 N max.

Environmental data

Temperature range	-55°C to +155°C
Thermal shock	MIL-STD-202, Method 107, Condition B
Vibration	MIL-STD-202, Method 204, Condition A
Shock	MIL-STD-202, Method 213, Condition A
Moisture resistance	MIL-STD-202, Method 106
Climatic Category	IEC 60068 55/155/21
Max. soldering temperature	IEC 61760-1, +260°C for 10 sec.
2002/95/EC (RoHS)	compliant

Tooling

N/A

Suitable cables

N/A

Packing

Standard	100 pcs in blister
Weight	0.26 g/pce

Draft	Date	Approved	Date	Rev.	Engineering change number	Name	Date
Gramsamer	01/03/06	Krautenbacher J.	21/09/06	b00	06-0478	B. Dandl	21/09/06

Rosenberger Hochfrequenztechnik GmbH & Co. KG
P.O.Box 1260 D-84526 Tittmoning Germany
www.rosenberger.de

Tel.: +49 8684 18-0
Fax: +49 8684 18-499
email: info@rosenberger.de

Page
2 / 2

Figure C.5: Rosenberger P/N 18S204-40ME4: Right angle plug

Appendix D

Low Noise Amplifier

PARTS LIST **PRELIMINARY**

ITEM	QTY	PART NUMBER	DESCRIPTION
1	40	M2 x 0.4 x 5 long SHCS 18-8 SS	Socket Head Cap Screw
2	14	M2 x0.4 x 6 long SHCS 18-8 SS	Socket Head Cap Screw
3	14	PIC-Design D6-20	Belleville Spring Washer
4	14	M2 Flat Washer, 18-8 SS	Plain washers
5	1	KP-000-01390-01	LNA Enclosure Top Lid DC End
6	4	KP-000-01391-01	LNA Enclosure Top Lid Centre
7	1	KP-000-01392-01	KPAF LNA Enclosure Top Lid Cryo End
8	10	Southwest Microwave 290-07G Glass Bead	Hermetic Electrical RF Feed Thru.
9	10	Southwest Microwave 212-500SF	SMA Electrical RF Connector
10	3	M2x 0.4 x 5 long FSHCS 18-8 SS	Flat socket head cap screws
11	1	Mouser 1563	Threaded Ground Pin
12	2	Mouser 534-11360	Feed Thru. Pin, Electrical
13	1	KP-000-01393-01	LNA Enclosure Bottom Lid
14	1	KP-000-01389-01	LNA Enclosure Body

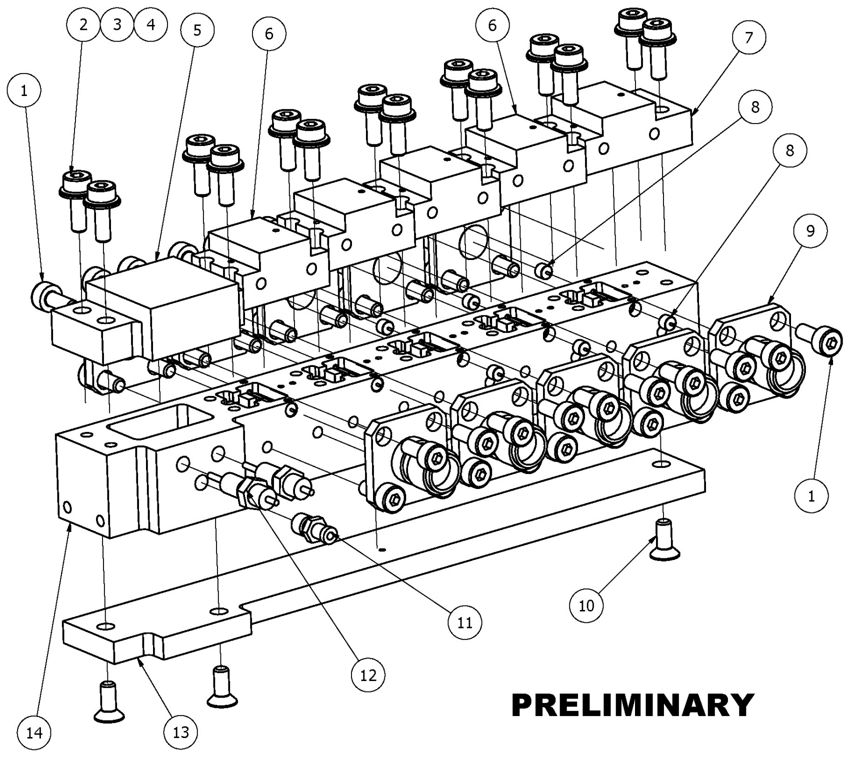

PRELIMINARY

PRELIMINARY

NOTES:

1. Material:
2. Finish: , colour:

P		Initial Release	XXX	MMM dd
REV REV	LOC EMPL	DESCRIPTION	BY PAR	DATE

UNLESS OTHERWISE STATED:
SAUF INDICATION CONTRAIRE:

ALL DIMENSIONS ARE IN
MILLIMETRES (MM)

TOLERANCES
X. ±0.5
X.X ±0.100
X.XX ±0.050
X.XXX ±0.010
ANGLE ±0°30'

MACHINING FINISH N7-1.6Um-63UIN
FINI OBTENU PAR USINAGE

EDGE BREAK 0.3 x 45°
FACONNAGE DES BORDS

THIRD ANGLE PROJECTION

NATIONAL RESEARCH COUNCIL CANADA
HERZBERG INSTITUTE OF ASTROPHYSICS
DOMINION ASTROPHYSICAL OBSERVATORY VICTORIA

CONSEIL NATIONAL DE RECHERCHES CANADA
INSTITUT HERZBERG D'ASTROPHYSIQUE
OBSERVATOIRE FEDERAL D'ASTROPHYSIQUE VICTORIA

DWG No. / DES. No. KP-000-01394-01
REV 0

TITLE / TITRE
LAN Body Assembly
Miniature 25 Blade Array

DESIGNED / CONCU PAR	DRAWN / DESSINE PAR	CHECKED / VERIFIE PAR	SCALE / ECHELLE	PROJECT / PROJET	SIZE / TAILLE
DATE 6/21/2013	DATE 9/25/2013	DATE	2:1	KPAF	B

Sheet 1 of 2

Figure D.1

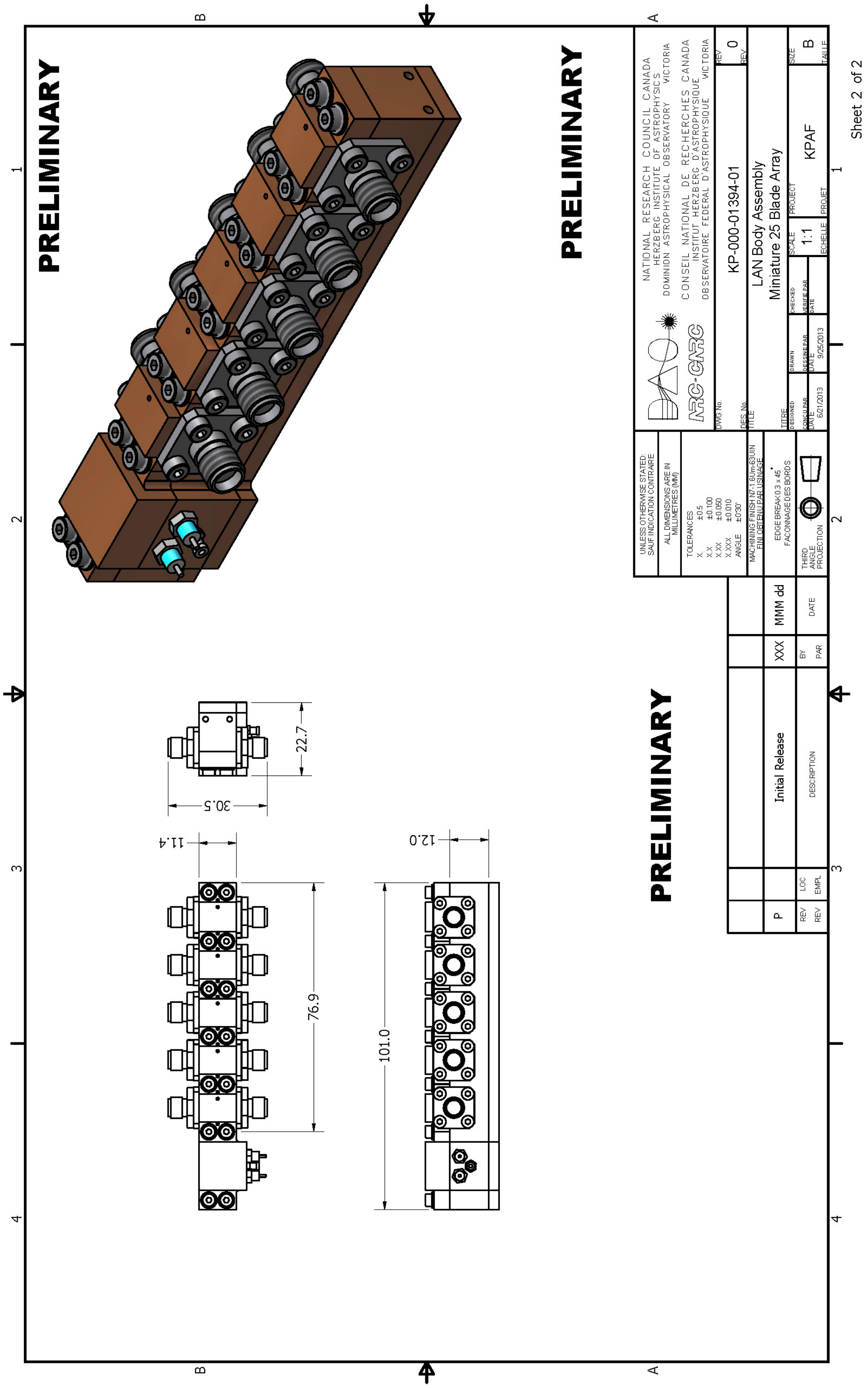
PRELIMINARY
PRELIMINARY
PRELIMINARY
22.7
30.5
11.4
12.0
76.9
101.0
P
Initial Release
XXX
MMM dd
REV
EMPL
LOC
DESCRIPTION
BY
PAR
DATE
UNLESS OTHERWISE STATED:
SAUF INDICATION CONTRAIRE:
ALL DIMENSIONS ARE IN
MILLIMETRES (MM)
TOLERANCES
X. ±0.5
X.X ±0.100
X.XX ±0.050
X.XXX ±0.010
ANGLE ±0°30'
MACHINING FINISH N7-1.6Um-63UIN
FINI OBTENU PAR USINAGE
EDGE BREAK 0.3 x 45°
FACONNAGE DES BORDS
THIRD
ANGLE
PROJECTION
NRC·CNRC
NATIONAL RESEARCH COUNCIL CANADA
HERZBERG INSTITUTE OF ASTROPHYSICS
DOMINION ASTROPHYSICAL OBSERVATORY VICTORIA
CONSEIL NATIONAL DE RECHERCHES CANADA
INSTITUT HERZBERG D'ASTROPHYSIQUE
OBSERVATOIRE FEDERAL D'ASTROPHYSIQUE VICTORIA
DWG No.
KP-000-01394-01
REV
0
DES. No.
TITLE
LAN Body Assembly
Miniature 25 Blade Array
TITRE
DESIGNED
CONCU PAR
DATE
6/21/2013
DRAWN
DESSINE PAR
DATE
9/25/2013
CHECKED
VERIFIE PAR
DATE
SCALE
1:1
ECHELLE
PROJECT
KPAF
PROJET
SIZE
B
TAILLE
Sheet 2 of 2
A
B
1
2
3
4

Figure D.2

Appendix E

Mixer

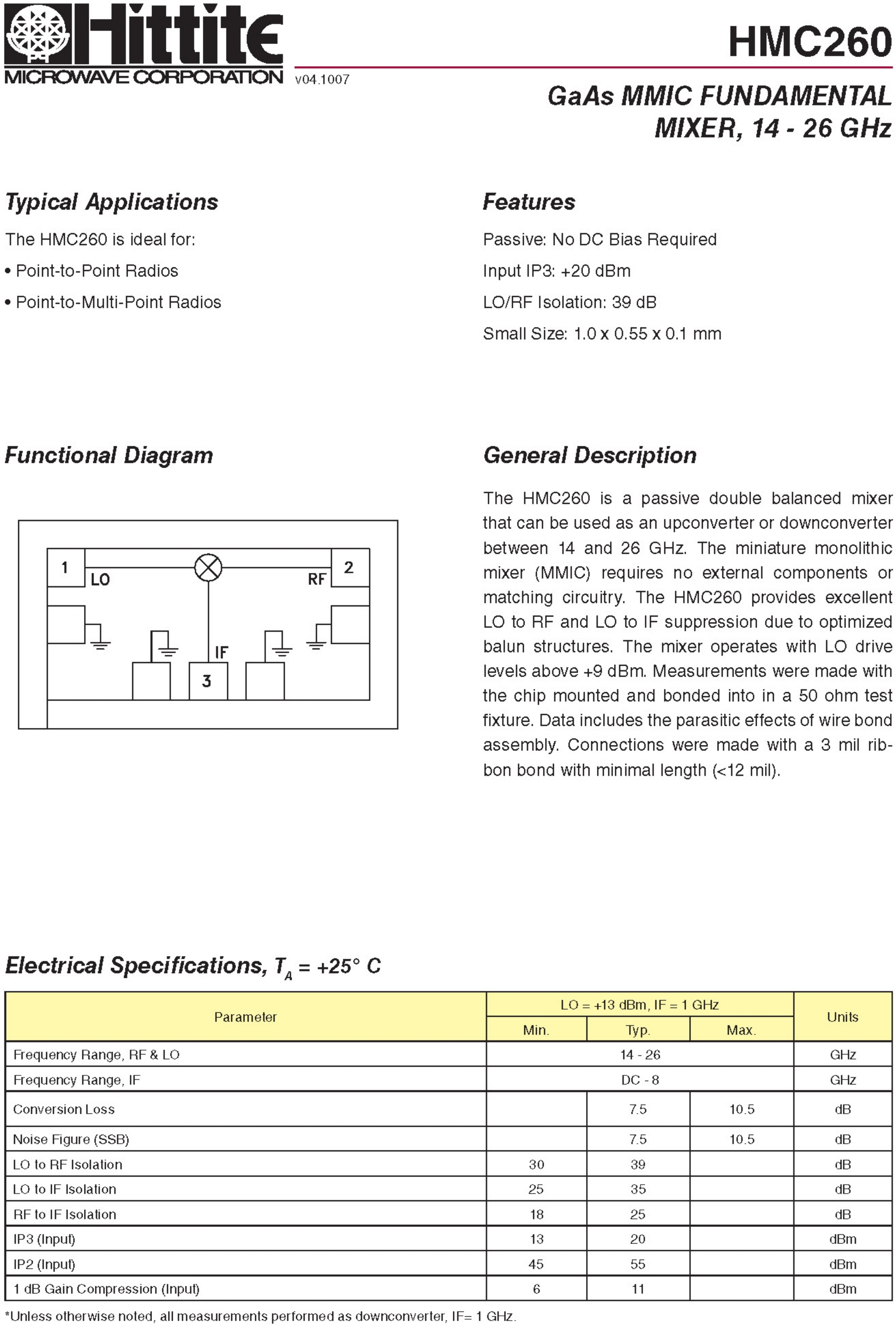

Hittite MICROWAVE CORPORATION v04.1007

HMC260

GaAs MMIC FUNDAMENTAL MIXER, 14 - 26 GHz

Typical Applications

The HMC260 is ideal for:

- Point-to-Point Radios
- Point-to-Multi-Point Radios

Features

Passive: No DC Bias Required

Input IP3: +20 dBm

LO/RF Isolation: 39 dB

Small Size: 1.0 x 0.55 x 0.1 mm

Functional Diagram

General Description

The HMC260 is a passive double balanced mixer that can be used as an upconverter or downconverter between 14 and 26 GHz. The miniature monolithic mixer (MMIC) requires no external components or matching circuitry. The HMC260 provides excellent LO to RF and LO to IF suppression due to optimized balun structures. The mixer operates with LO drive levels above +9 dBm. Measurements were made with the chip mounted and bonded into in a 50 ohm test fixture. Data includes the parasitic effects of wire bond assembly. Connections were made with a 3 mil ribbon bond with minimal length (<12 mil).

Electrical Specifications, T_A = +25° C

Parameter	LO = +13 dBm, IF = 1 GHz			Units
	Min.	Typ.	Max.	
Frequency Range, RF & LO		14 - 26		GHz
Frequency Range, IF		DC - 8		GHz
Conversion Loss		7.5	10.5	dB
Noise Figure (SSB)		7.5	10.5	dB
LO to RF Isolation	30	39		dB
LO to IF Isolation	25	35		dB
RF to IF Isolation	18	25		dB
IP3 (Input)	13	20		dBm
IP2 (Input)	45	55		dBm
1 dB Gain Compression (Input)	6	11		dBm

*Unless otherwise noted, all measurements performed as downconverter, IF= 1 GHz.

Figure E.1: Hittite Mixer Corporation - HMC260 - Downconverting mixer MMIC